NTNU

Norwegian University of Science and Technology

Department of Materials Science and Engineering

A Computational Study of Thermal Diffusion

Thermodynamic Modelling of the Soret Coefficient

Author
Vegard Gjeldvik Jervell

Supervisor
Professor
Øivind Wilhelmsen

December 22, 2021

Acknowledgements

I would like to thank Karl, Aamund, Andrea and everyone else that has pulled me out of my chair for breaks on all the long days, and Torbjørn for reminding me to go home on the even longer ones. I want to thank Olav for interesting late night discussions on the days I didn't get home. I also want to thank all the people that fill the coffee mug at the office, and all those that help me empty it, you truly, honestly, make every day so very much better. Most importantly, I would like to thank Øivind for guiding me thorough the jungle of irreversible thermodynamics with interesting, motivating discussions and an impressive patience for my at times far-fetched ideas.

Finally, I would like to thank Alexandra, for calling every night, always believing in me and always motivating me to be the best i can be and do the best i can do. This would never have been possible without your never-ending support and endless supply of pure joy.

Abstract

Thermal diffusion, or the Soret effect, is a phenomenon that has intrigued theorists and experimentalists alike for over a century. In essence, it is the phenomenon that in a mixture exposed to a thermal gradient, the components will separate. This effect can be quantified by a coupling coefficient known as the Soret coefficient. Despite being the subject of extensive studies, no model has yet been developed that is capable of consistently and reliably predicting the Soret coefficient. In this work, a model proposed by Kempers is systematically investigated. The model consists of a set of equations that are solved by the use of an equation of state (EoS) together with kinetic gas theory.

The primary focus is divided into two parts. In the first part, the building blocks of the model; the equation of state and the Enskog solutions, are investigated separately. The SAFT-VR-MIE EoS is shown to reliably reproduce the vapour-liquid equilibria (VLE) and the pressure-temperature-volume (PVT) behaviour of the Lennard-Jones fluid, as predicted in molecular dynamics (MD) simulations. The Enskog solutions up to order five are shown to give reasonable predictions for gas phase diffusion coefficients, when combined with the temperature dependent Barker-Henderson hard sphere diameter. Further, the numerical challenges of increasing the order of approximation of the Enskog solutions are investigated, and it is found that the equations should be scaled or preconditioned to avoid numerical instability.

In the second part, the ability of Kempers' model to predict the Soret coefficient in various mixtures is investigated. It is found that the ability of an EoS to predict the VLE and PVT behaviour of a fluid is an insufficient measure of its suitability for use in modelling the Soret effect. The Kempers-model is shown to be highly inconsistent in its ability to reproduce the Soret coefficient obtained from both MD simulations and experimental measurements.

Finally, in a critical assessment of the derivation proposed by Kempers, potential flaws in the model are revealed and the possibilities of improving the model are discussed.

Contents

1 Introduction

Thermal diffusion, also known as the Soret effect or Ludwig-Soret effect, is an intriguing phenomenon that has interested researchers for over a hundred years since it was first described by Carl Friedrich Wilhelm Ludwig in the mid 19th century. [1] The phenomenon is that a mixture with an imposed temperature gradient will develop a concentration gradient. This a consequence of the well known result from irreversible thermodynamics, that there are cross-coupling coefficients between fluxes and driving forces. [2] The inverse effect - a heat flux resulting from an imposed gradient in chemical potential is known as the Dufour effect.

Onsager showed that the coefficient matrix that describes coupling of fluxes and forces is symmetrical, introducing the famous Onsager reciprocal relations. [3] These relations imply that the coefficient coupling a thermal gradient to a mass flux is equal to the coefficient that couples a chemical potential gradient to a heat flux. This means that if one is capable of modelling the Soret coefficient, the same model can be used to predict the Dufour effect.

As modern science progresses, engineering applications also push further into extreme conditions. Nano-scale precision is commonly used in the production and development of modern technology, both in the texturing of surfaces and structuring of pores in nano-porous materials. [4] At this scale small variations in concentration and temperature lead to enormous gradients. In the design of battery electrodes and electrolytes, transport properties are of major importance, and during operation a temperature gradient arises in the battery due to the electrode reactions and internal resistance. [5] Further development in these fields therefore warrants precise descriptions of the coupling of heat and mass transfer.

Modern material applications on the macro scale require materials that can perform reliably when subjected to large temperature gradients over time. [2] This includes the materials used in reactors, both chemical and nuclear, as well as materials in pipes and containers containing fluids far from ambient temperature, and the coatings used on said materials. To further progress the development of materials subjected to these extreme conditions, increased precision in the modelling and prediction of diffusive behaviour is required.

In the field of Biochemical engineering, precise control of heat- and oxygen flow is required. [6] This is also a major hurdle in the up-scaling of bio-reactors. Specifically, the transfer of oxygen into the reactor solution at a rate high enough to keep a high concentration of microorganisms alive is challenging. More precise modelling of how the thermal gradients in the reactor and the mass transfer of oxygen interact may be of use in overcoming this challenge.

1.1 Thermal diffusion

In a binary mixture, with one independent diffusive mass flux and no pressure gradient, the mass flux of component 1 in the center-of-mass (CoM) frame of reference (FoR) may be written as, [7]

$$\mathbf{J}_1^{mm} = L_{\mu\mu}\nabla w_1 + L_{\mu q}\nabla T. \tag{1.1}$$

where w_1 denotes the mass fraction of component 1, J_1^{mm} denotes the mass flux of component 1 in the CoM FoR, $L_{\mu\mu}$ is the coefficient connecting the mass fraction gradient to the flux, closely related to the diffusion coefficient, and $L_{\mu q}$ is the coupling coefficient connecting a thermal gradient to a mass flux. It is assumed that $L_{\mu\mu}$ and $L_{\mu q}$ are independent of the fluxes and gradients in a system, such that in a state where the mass flux vanishes the gradients are related by

$$\frac{\nabla w_1}{\nabla T} = -\frac{L_{\mu\mu}}{L_{\mu q}}. \tag{1.2}$$

This expression will appear differently depending on the basis and FoR it is expressed in, as further discussed in Section 3.1. It is however immediately clear from equation (1.2) that one can define a coefficient relating the gradients in concentration and temperature. Here, the Soret coefficient S_T, and the thermal diffusion factor α_T refer to

$$S_{T,i} \equiv \frac{\nabla x_i}{x_i(1-x_i)\nabla T}, \qquad \alpha_{T,i} \equiv \frac{T\nabla x_i}{x_i(1-x_i)\nabla T} = TS_{T,i}, \tag{1.3}$$

where x_i denotes the mole fraction of component i and T denotes the temperature. Additionally, the thermal diffusion coefficient D_T, and thermal diffusion ratio k_T may be defined. Their definitions are slightly more involved and are discussed in more detail in Section 2.3.

Accurate prediction of the coefficients describing thermal diffusion has proven to be a challenging task. Several empirical and semi-empirical correlations have been proposed. Though these models give reasonably good fits to the data they are regressed against, their nature of containing fitting parameters makes their predictive power disputable. For example the power law correlations by Longree et al.[8] may be useful for mixtures in which both components are accurately described by a Lennard-Jones potential, but cannot be expected to give accurate predictions for more complex molecules. The model is also restricted to binary mixtures and does not incorporate any dependency on the composition, density or temperature of the system. A model proposed by Firoozbadi and Shukla,[9,10] is based on first principle considerations and extended to multicomponent systems, but one inherently physical parameter is treated as a fitting parameter. Though this fitting parameter is determined to have the same value for a variety of systems, one cannot in general expect the model to hold for solid state systems or mixtures that differ greatly from those tested.

Kinetic gas theory, in particular the standard Enskog theory (SET),[11] revised Enskog theory (RET),[12] and modified Enskog theory (MET),[13] have been shown to give reasonable predictions for low density gases in which relatively simple intermolecular potentials can be employed.[14–17] However, the precision must be expected to deteriorate quickly for systems with many body interactions or complex molecules. This includes polymers, strongly associating molecules and solid state systems, and no attempts to compare the theory to such systems were found at the time of writing.

A model proposed by Kempers,[18] based purely on thermodynamic considerations, provides a method of predicting the effect of thermal diffusion for multicomponent systems without employing any specific intermolecular potential or fitting parameters. The model is claimed to be applicable to any system for which a sufficiently accurate equation of state (EoS) is available. Eslamian and Saghir have proposed modifications to the model,[19] based on the activation energy of viscous flow, although they comment that their model is incomplete in the incorporation of complex intermolecular forces.

1.2 Scope

In this work the model proposed by Kempers is investigated in detail. In an attempt to isolate the predictive capabilities of the Kempers-model from that of the employed equation of state, the primary data used for comparison is taken from molecular dynamics (MD) simulations of Lennard-Jones fluid mixtures. The equation of state that is employed for this comparison is the SAFT-VR-MIE EoS, which may be supplied with the same interaction parameters as those used in the simulations.

Additionally, the predictions of the SAFT-VR-MIE EoS and of the Enskog solutions are investigated individually to better understand the behaviour of the building blocks upon which the Kempers-model is based. The primary goal is to assess under what conditions the Kempers model can provide reliable predictions of the Soret coefficient, if any, and to uncover how one may determine if the predictions of the model are reliable in cases where no data for validation is available.

2 Theory

As the Kempers-model requires both an equation of state, and the results of kinetic gas theory, some elaboration on both is fitting. This section will therefore begin with a thorough introduction of the Kempers-model, before introducing and summarising the established thermodynamic- and kinetic gas theory that is used throughout the report.

2.1 The Kempers model

The focus of this section is to elucidate the Kempers-model and its derivation. The arguments presented throughout the derivation differ somewhat in formulation from those presented by Kempers, this is to facilitate the further discussion of the derivation in Section 6.

Consider a system consisting of two bulbs, denoted α and β, of equal volume V connected by a tube of negligible volume. The bulbs are filled with some homogeneous phase of given composition $\mathbf{n}$. Impose now a temperature gradient in the connecting tube and allow the system to reach the steady state, where the mass flux of all components vanishes. The temperature of each bulb is uniform, such that each bulb is at equilibrium.

Regarding the two bulbs as independent subsystems, the partition function of the system can be written as $Z(\mathbf{n}_\alpha, \mathbf{n}_\beta, V, T_\alpha, T_\beta) = Z_\alpha(\mathbf{n}_\alpha, V, T_\alpha)Z_\beta(\mathbf{n}_\beta, V, T_\beta)$, where $\mathbf{n}_i$, T_i and Z_i are the composition, temperature and partition function of bulb i. Following the principle of maximum multiplicity, the equilibrium state will be the state that maximises the total partition function. This is the equivalent of minimising the Helmholtz energy (A) of the system. The optimisation is conducted under the constraint of conservation of species, and constant bulb volumes. The composition of each bulb at equilibrium is then given by the constrained optimisation

$$\begin{aligned} \max_{\mathbf{n}_\alpha, \mathbf{n}_\beta} \{Z(\mathbf{n}_\alpha, \mathbf{n}_\beta, V, T_\alpha, T_\beta)\} &= \max_{\mathbf{n}_\alpha, \mathbf{n}_\beta} \{Z_\alpha(\mathbf{n}_\alpha, V, T_\alpha)Z_\beta(\mathbf{n}_\beta, V, T_\beta)\} \\ &= \min_{\mathbf{n}_\alpha, \mathbf{n}_\beta} \left\{ \frac{A_\alpha(\mathbf{n}_\alpha, V, T_\alpha)}{RT_\alpha} + \frac{A_\beta(\mathbf{n}_\beta, V, T_\beta)}{RT_\beta} \right\} \\ n_i^\alpha + n_i^\beta &= n_i, \quad \forall \quad i \\ \sum_i n_i^\alpha v_i^\alpha &= \sum_i n_i^\beta v_i^\beta. \end{aligned} \tag{2.1}$$

Where the subscripts on the min and max statements denote the free variables of optimisation, v_i is the partial molar volume of species i and R is the gas constant. This system will be referred to as the "real" system. The notation adopted here is to be understood such that the result of the minimisation statements is the point at which the minimum is found, not the minimum value of the function subject to minimisation. That is, for a function $f(x, y)$,

$$\min_{x,y} \{f(x, y)\} = (x_{min}, y_{min}) \tag{2.2}$$

where (x_{min}, y_{min}) are the coordinates of the minimum.

Consider now the same bulbs, at the same temperatures, filled with an ideal gas mixture of total composition $\mathbf{n}$ equivalent to that of the real system. This system will be referred to as the "ideal gas system", and its variables will be denoted with a superscript ^{ig}. The bulb compositions at steady state are denoted $\mathbf{n}_\alpha^{ig}$ and $\mathbf{n}_\beta^{ig}$. These are independent of the compositions $\mathbf{n}_\alpha$ and $\mathbf{n}_\beta$, depending only on the total composition $\mathbf{n}$ and the temperatures. It then follows that the Helmholtz energy of the ideal gas system, $A^{ig}(\mathbf{n}_\alpha^{ig}, \mathbf{n}_\beta^{ig}, V, T_\alpha, T_\beta)$, is independent of the bulb compositions in the real system. Naturally, the composition of the bulbs in the ideal gas state is given by an optimisation analogous to the one in Equation (2.1). Because the two optimisations are independent problems, they may be solved simultaneously to give the same result as if they were solved

independently. Thereby, the minimisation statement in Equation (2.1) can be rewritten as

$$\begin{aligned}
\min_{\mathbf{n}_\alpha,\mathbf{n}_\beta}\left\{\frac{A_\alpha(\mathbf{n}_\alpha,V,T_\alpha)}{RT_\alpha}+\frac{A_\beta(\mathbf{n}_\beta,V,T_\beta)}{RT_\beta}\right\}&\\
=\min_{\mathbf{n}_\alpha,\mathbf{n}_\beta}\left\{\frac{A_\alpha(\mathbf{n}_\alpha,V,T_\alpha)}{RT_\alpha}+\frac{A_\beta(\mathbf{n}_\beta,V,T_\beta)}{RT_\beta}\right\}&\\
-\min_{\mathbf{n}_\alpha^{ig},\mathbf{n}_\beta^{ig}}\left\{\frac{A_\alpha^{ig}(\mathbf{n}_\alpha^{ig},V,T_\alpha)}{RT_\alpha}+\frac{A_\beta^{ig}(\mathbf{n}_\beta^{ig},V,T_\beta)}{RT_\beta}\right\}&\\
=\min_{\mathbf{n}_\alpha,\mathbf{n}_\beta,\mathbf{n}_\alpha^{ig},\mathbf{n}_\beta^{ig}}\left\{\frac{A_\alpha(\mathbf{n}_\alpha,V,T_\alpha)-A_\alpha^{ig}(\mathbf{n}_\alpha^{ig},V,T_\alpha)}{RT_\alpha}\right.&\\
\left.+\frac{A_\beta(\mathbf{n}_\beta,V,T_\beta)-A_\beta^{ig}(\mathbf{n}_\beta^{ig},V,T_\beta)}{RT_\beta}\right\}&
\end{aligned}\tag{2.3}$$

$$\begin{aligned}
n_i^\alpha+n_i^\beta&=n_i,\quad\forall\quad i\\
n_i^{\alpha,ig}+n_i^{\beta,ig}&=n_i^\alpha+n_i^\beta,\quad\forall\quad i\\
\sum_i n_i^\alpha v_i^\alpha&=\sum_i n_i^\beta v_i^\beta\\
\sum_i n_i^{\alpha,ig}v_i^{\alpha,ig}&=\sum_i n_i^{\beta,ig}v_i^{\beta,ig},\qquad\left(v_i^{\alpha,ig},v_i^{\beta,ig}\right)=\left(\frac{RT_\alpha}{p_\alpha^{ig}},\frac{RT_\beta}{p_\beta^{ig}}\right)
\end{aligned}$$

where p denotes the pressure. Applying the Lagrange multiplier method to this problem yields the set of equations

$$\begin{aligned}
\nabla_{\mathcal{L}}\left\{\frac{A_\alpha-A_\alpha^{ig}}{RT_\alpha}+\frac{A_\beta-A_\beta^{ig}}{RT_\beta}-\sum_{i=1}^{N}\left[\lambda_i\left(n_i^\alpha+n_i^\beta-n_i\right)+\gamma_i\left(n_i^\alpha+n_i^\beta-n_i^{\alpha,ig}-n_i^{\beta,ig}\right)\right]\right.&\\
\left.-\nu_1\left(\sum_i n_i^\alpha v_i^\alpha-n_i^\beta v_i^\beta\right)-\nu_2\left(\frac{T_\alpha}{p_\alpha^{ig}}\sum_i n_i^{\alpha,ig}-\frac{T_\beta}{p_\beta^{ig}}\sum_i n_i^{\beta,ig}\right)\right\}=0&
\end{aligned}\tag{2.4}$$

$$\nabla_{\mathcal{L}}=\left[\frac{\partial}{\partial\mathbf{n}_\alpha},\frac{\partial}{\partial\mathbf{n}_\beta},\ \frac{\partial}{\partial\mathbf{n}_\alpha^{ig}},\frac{\partial}{\partial\mathbf{n}_\beta^{ig}},\frac{\partial}{\partial\boldsymbol{\lambda}},\frac{\partial}{\partial\boldsymbol{\gamma}},\frac{\partial}{\partial\nu_1},\frac{\partial}{\partial\nu_2}\right]_{T_\alpha,T_\beta,V}$$

Taking the derivatives with respect to n_i^α and $n_i^{\alpha,ig}$ yields

$$\begin{aligned}
\frac{\mu_i^\alpha}{RT_\alpha}-\lambda_i-\gamma_i-\nu_1 v_i^\alpha=0&\\
\frac{\mu_i^{\alpha,ig}}{RT_\alpha}+\gamma_i-\nu_2\underbrace{\left(\frac{T_\alpha}{p_\alpha^{ig}}-\frac{T_\alpha}{\left(p_\alpha^{ig}\right)^2}\left(\frac{\partial p_\alpha^{ig}}{\partial n_i^{\alpha_i g}}\right)_{T_\alpha,V}\sum_j n_i^{\alpha_i g}\right)}_{=0}=0.&
\end{aligned}\tag{2.5}$$

Where μ denotes the chemical potential, and the term containing ν_2 vanishes by the ideal gas law. Multiplying by R and summing these equations, and doing the equivalent for n_i^β and $n_i^{\beta,ig}$, eliminates the γ_i. The resulting equations are

$$\begin{aligned}
\frac{\mu_i^\alpha-\mu_i^{\alpha,ig}}{T_\alpha}-\lambda_i-\nu_1 v_i^\alpha=0&\\
\frac{\mu_i^\beta-\mu_i^{\beta,ig}}{T_\beta}-\lambda_i+\nu_1 v_i^\beta=0&
\end{aligned}\tag{2.6}$$

subtracting the second equation in (2.6) from the first equation eliminates the λ_i, giving

$$\frac{\mu_i^\alpha - \mu_i^{\alpha,ig}}{T_\alpha} - \frac{\mu_i^\beta - \mu_i^{\beta,ig}}{T_\beta} - \nu_1 \left(v_i^\alpha + v_i^\beta\right) = 0 \tag{2.7}$$

Solving equation k for ν_1 and inserting the expression back into the remaining equations yields

$$\frac{v_k^\alpha + v_k^\beta}{v_i^\alpha + v_i^\beta}\left(\frac{\mu_i^\alpha - \mu_i^{\alpha,ig}}{T_\alpha} - \frac{\mu_i^\beta - \mu_i^{\beta,ig}}{RT_\beta}\right) = \frac{\mu_k^\alpha - \mu_k^{\alpha,ig}}{T_\alpha} - \frac{\mu_k^\beta - \mu_k^{\beta,ig}}{RT_\beta} \qquad i = \{1,2,...,N\} \cap \{k\} \tag{2.8}$$

It is simple to see that if Equation (2.8) holds for all $i \neq k$, the choice of k is arbitrary. Therefore $k = N$ is chosen for notational convenience. Now, $v_i^\alpha + v_i^\beta$ may be developed as a Taylor series about the average of the two bulbs. Ignoring third and higher order derivatives, then expressing the difference between bulb α and β as $\Delta\varphi = \varphi_\alpha - \varphi_\beta$, where φ is any variable, this equation may be rewritten as

$$\frac{1}{v_i}\left[\Delta\left(\frac{\mu_i}{T}\right) - \Delta\left(\frac{\mu_i^{ig}}{T}\right)\right] = \frac{1}{v_N}\left[\Delta\left(\frac{\mu_N}{T}\right) - \Delta\left(\frac{\mu_N^{ig}}{T}\right)\right] \tag{2.9}$$

Expanding $\Delta\left(\frac{\mu_i}{T}\right)$ as a Taylor series in the variables $T, p, n, x_i, ..., x_{N-1}$ and making use of the fact that $\sum_i v_i^\alpha n_i^\alpha = \sum_i v_i^\beta n_i^\beta \implies \Delta p = 0$, one obtains for the first two terms

$$\Delta\left(\frac{\mu_i}{T}\right) = \frac{\partial}{\partial T}\left(\frac{\mu_i}{T}\right)_{p,\mathbf{n}} \Delta T + \frac{1}{T}\sum_{j=1}^{N-1}\left(\frac{\partial \mu_i}{\partial x_j}\right)_{T,p,x_{k\neq j}} \Delta x \tag{2.10}$$

Using the relation

$$h_i = -T^2 \frac{\partial}{\partial T}\left(\frac{\mu_i}{T}\right)_{p,\mathbf{n}}, \tag{2.11}$$

where h_i denotes the partial molar enthalpy of component i, and for the ideal gas case,

$$\Delta\left(\frac{\mu_i^{ig}}{T}\right) = -h_i^{ig}\frac{\Delta T}{T} + \frac{R}{x_i}\Delta x_i, \tag{2.12}$$

and recognising the thermal diffusion factor in the ideal gas state as

$$\alpha_{T,i}^{ig} = -\frac{T\Delta x_i^{ig}}{x_i(1-x_i)}, \tag{2.13}$$

Equation (2.9) can be rewritten as

$$\sum_{j=1}^{N-1}\left(\frac{1}{v_i}\left(\frac{\partial \mu_i}{\partial x_j}\right)_{T,p} - \frac{1}{v_N}\left(\frac{\partial \mu_N}{\partial x_j}\right)_{T,p}\right) x_j(1-x_j)\alpha_{T,j} = \frac{h_N - h_N^{ig}}{v_N} - \frac{h_i - h_i^{ig}}{v_i} + RT\left(\frac{(1-x_i)\alpha_{T,i}^{ig}}{v_i} - \frac{(1-x_N)\alpha_{T,N}^{ig}}{v_N}\right) \tag{2.14}$$

$i = \{1,2,...,N-1\}$.

Together with the summational constraint $\sum_i \alpha_{T,i} x_i(1-x_i) = 0$, this set of equations can be solved for all the thermal diffusion factors, given a model for α_T^{ig} and a suitable equation of state. This set of equations

will be referred to as the Kempers Center-of-Volume (K-CoV) model. For a binary system Equation (2.14) simplifies to

$$\alpha_{T,1} = \frac{v_1}{V_m} \frac{h - h^{ig} - (h_1 - h_1^{ig}}{x_1 x_2 \left(\frac{\partial \mu_1}{\partial x_1}\right)_{T,p}} + \frac{RT}{x_1 \left(\frac{\partial \mu_1}{\partial x_1}\right)_{T,p}} \alpha_{T,1}^{ig}. \tag{2.15}$$

In the case presented thus far, the centre of mass of the contents of the bulbs will shift relative to the bulbs. If the exact same derivation is carried out, but imagining that no external forces are exerted on the two bulb system to hold it in place, the center-of-mass (CoM) of the system must remain stationary by conservation of momentum. It that case, the constraint $\sum_i v_i^\alpha n_i^\alpha = \sum_i v_i^\beta n_i^\beta$ may be replaced by $\sum_i m_i n_i^\alpha = \sum_i m_i n_i^\beta$, with m_i the molar mass of species i. The result will then be identical to Equation (2.14), but with the partial molar volumes replaced by molar masses. The resulting set of equations will be referred to as the Kempers center-of-mass (K-CoM) model. The two models will jointly be referred to as the Kempers-model.

2.2 Equations of state

An equation of state (EoS) is an equation that relates various thermodynamic state variables.[20] Often, these are expressed on the form $p = p(n, V, T; d_1, d_2, ...d_n)$ where p, V, n, T are the pressure, mole number, volume and temperature and the d_i are parameters determined either empirically, from first principles or some combination of the two. Alternative manners of expressing an EoS are by the use of the compressibility factor $Z \equiv \frac{pV}{nRT}$, or by expressing pressure as a polynomial in $\frac{1}{V_m}$, where V_m denotes the molar volume, known as a virial expansion. Before these are discussed however, it is convenient to introduce the principle of corresponding states (CSP). This principle states that at a reduced state $(p_r, V_r, T_r) = \left(\frac{p}{p_c}, \frac{V}{V_c}, \frac{T}{T_c}\right)$, where subscript c denotes the critical properties of the fluid, all fluids will behave identically.[21] This principle is known to hold well for systems in which quantum effects are negligible, and rotational and translational motion of molecules is independent.

The CSP gives rise to a formulation of the compressibility factor as a function of reduced temperature and volume, $Z = Z(T_r, V_r)$.[21] To account for molecules and conditions in which the CSP does not hold, additional corrections may be employed. A popular choice being the accentric factor (ω), which describes a molecular force fields deviation from spherical shape.[20] The compressibility factor then takes the functional form

$$Z = Z^{(0)}(T_r, p_r) + \omega Z^{(1)}(T_r, p_r), \tag{2.16}$$

where $Z^{(0)}$ describes a perfectly spherical molecule, and $Z^{(1)}$ describes a deviation from spherical geometry. $Z^{(0)}$ and $Z^{(1)}$ are assumed to be equal for all molecules, such that knowledge of the accentric factor and the critical parameters is sufficient to describe the behaviour of a pure fluid.

The behaviour of a fluid may also be described accurately by a virial expansion of the form

$$p = \frac{RT}{V_m} + \frac{RTB(T)}{V_m^2} + \frac{RTC(T)}{V_m^3} + ... \tag{2.17}$$

This approach has its foundation in statistical thermodynamics, and is popular in part because the virial coefficients $B(T), C(T), ...$ can be related to the intermolecular potential of the molecules in the fluid.[20]

The simplest EoS in common use is the ideal gas law, and its close relatives, the cubic equations of state.[20] These include the Van der Waals (VdW), Peng-Robinson (PR), Soave-Redlich-Kwong (SRK), Schmidt-Wensel (SW) and Patel-Teja (PT) equations of state, among others. They have in common that the pressure has a cubic dependency on volume, that they have relatively few fitting parameters, and that the parameters have some physical interpretation. Several cubic equations of state have been in industrial use for decades, meaning they have been thoroughly tested and verified. This makes them versatile and reliable for many common usages.

Another EoS worth mentioning is the Carnahan-Starling (CS) EoS for hard spheres.[22] This equation is based on approximating the virial expansion in volume as an infinite geometric series. Manipulation of this series yields an explicit expression for the compressibility factor for hard spheres as a function of the packing fraction, η, given as

$$\eta = \frac{\pi N_A n \left(\sigma^{HS}\right)^3}{6V} \tag{2.18}$$

where n is the mole number of particles, σ^{HS} is the hard sphere diameter and N_A is Avogadros number. Once an expression for the compressibility factor is known, all other properties of interest may be related by various derivatives of this. This EoS has proven highly precise when measured against MD-simulations of hard-sphere particles.[22] Nevertheless, several propositions of extensions and modifications have been made to the theory from its introduction until today, in attempts to further improve its performance.[23,24] An important area of usage for the CS EoS is the ability to accurately represent a theoretical hard sphere state, which can be a convenient reference state.

A frequent starting point in the development of an EoS is aiming to describe the Helmholtz energy (A) of a system. This can be done by regarding the intermolecular potential, the performance of the resulting EoS will reflect how well the chosen intermolecular potential describes the system. Observable properties, and other properties of interest, such as the entropy, chemical potential and so on can be related to the derivatives of the Helmholtz energy. This approach opens several doors: The possibility to estimate molecular parameters from macroscopic observations; firm control of the microscopic description of the system; the option to explicitly include quantum effects, and the possibility to create equations of state for theoretical fluids, such as the Lennard-Jones fluid. Apart from accurately describing real fluids, this means one can construct an EoS that, in principle, should exactly reproduce the results of molecular dynamics (MD) simulations, which can be useful in the development of thermodynamic models.

Many equations of state have been developed using the approach outlined above. Of particular interest in the context of this report is the SAFT-VR-MIE EoS. This EoS utilises a general Mie potential to describe the monomer-monomer interactions in a fluid, which in turn can be related to the Helmholtz energy.[25] This is done by using the framework of Barker-Henderson (BH) perturbation theory to show that the residual Helmholtz energy may be written as the sum of a hard sphere term, which may be determined by the Carnahan-Starling (CS) EoS,[22] several "dispersion" terms, and a chain term describing the formation of chains of Mie-segments. This EoS has been shown to give highly accurate predictions of fluid-phase equilibria PVT-behaviour and second-derivative properties for both pure fluids and mixtures.

Up until this point the discussion has been mostly limited to pure fluids. When applying and EoS to a mixture, composition must be taken into account. This is accomplished by the use of mixing rules.[20] A mixing rule is an equation that in some way combines or averages the parameters of the components in a mixture such that an EoS can be applied. These equations are to a large degree empirical in nature, and are typically expressed on the form

$$\varphi_m = \sum_i \sum_j x_i x_j \varphi_{ij} \tag{2.19}$$

where φ_m is some property of the mixture, and φ_{ii}, φ_{jj} are the properties of the pure components. Various combining rules can be chosen to determine the interaction terms φ_{ij}. An example of such combining rules are the Lorentz-Berthelot (LB) rules for combining the parameters of a Mie-potential

$$\sigma_{ij} = \frac{1}{2}\left(\sigma_{ii} + \sigma_{jj}\right), \qquad \varepsilon_{ij} = \sqrt{\varepsilon_{ii}\varepsilon_{jj}}. \tag{2.20}$$

These are of special significance in this report, and may be modified to create the more general mixing rules hereafter termed the modified Lorentz-Berthelot rules,[26,27] given as

$$\sigma_{ij} = \frac{1}{2}\left(\sigma_{ii} + \sigma_{jj}\right), \qquad \varepsilon_{ij} = (1 - k_{ij})\frac{\left(\sigma_{ii}\sigma_{jj}\right)^{\frac{3}{2}}}{\sigma_{ij}^3}\sqrt{\varepsilon_{ii}\varepsilon_{jj}}, \tag{2.21}$$

where k_{ij} is a parameter that may be adjusted represent the behaviour of fluids for which particle interaction is energetically favourable ($k_{ij} > 0$), stabilising the liquid phase; or fluids for which interaction is less favourable ($k_{ij} < 0$), destabilising the liquid phase and lowering the boiling point.

2.3 Kinetic gas theory

The kinetic theory of gases was initiated with the development of the Maxwell-Boltzmann equations in the mid- to late 19th century.[11] The equations are based in statistical mechanics, and consider the effects of collisions between particles. The solutions to these equations, developed by Chapman and Enskog in the early 20th century, are termed the Chapman-Enskog or Enskog solutions, and the resulting theory is referred to as Enskog theory. This theory has later been expanded and elaborated upon by Chapman and Cowling, among many others.[12,13]

The theory is highly mathematical in nature and at times difficult to follow. Nevertheless the goal of this section is to present a pedagogical summary of the derivations and results integral to this report. For a complete, rigorous explanation of the theory, the reader is referred to the text by Chapman and Cowling.[11] It is worth mentioning that despite being a compressed summary, this section is characterised by a large volume of notation and definitions. This is due to the theory itself being characterised by multiply nested definitions, and notation that requires explaining. Note also that the notation employed here differs somewhat from that of Chapman and Cowling so as to remain consistent throughout the report.

The goal of this section is to arrive at a set of explicit equations that can be solved for the interdiffusion- and thermal diffusion coefficients, such that a value for α_T^{ig} may be supplied to the Kempers-model. This will require a rigorous definition of how these coefficients relate to the average velocities of particles in a mixture. It may be fruitful to have the final result in mind when reading, to have this as a reference point as new variables and functions are introduced. By the end of this section the integrals

$$\begin{aligned} D_{12} \equiv & \frac{\rho_1\rho_2}{3\rho}\{\mathbf{D},\mathbf{D}\} \\ = & \frac{\rho_1\rho_2}{3\rho^3}\int \mathbf{D}_1 \iiint f_1^{(0)} f_{1'}^{(0)} (\mathbf{D}_1 + \mathbf{D}_{1'} - \mathbf{D}'_1 - \mathbf{D}'_{1'}) b\mathrm{d}b\mathrm{d}\epsilon\mathrm{d}\mathbf{u}_{1'}\mathrm{d}\mathbf{u}_1 \\ & + \frac{\rho_1\rho_2}{6\rho^3}\iiiint f_1^{(0)} f_2^{(0)} (\mathbf{D}_1 + \mathbf{D}_2 - \mathbf{D}'_1 - \mathbf{D}'_2)^2 b\mathrm{d}b\mathrm{d}\epsilon\mathrm{d}\mathbf{u}_1\mathrm{d}\mathbf{u}_2 \\ & + \frac{\rho_1\rho_2}{3\rho^3}\int \mathbf{D}_2 \iiint f_2^{(0)} f_{2'}^{(0)} (\mathbf{D}_2 + \mathbf{D}_{2'} - \mathbf{D}'_2 - \mathbf{D}'_{2'}) b\mathrm{d}b\mathrm{d}\epsilon\mathrm{d}\mathbf{u}_{2'}\mathrm{d}\mathbf{u}_2 \end{aligned} \tag{2.22}$$

$$\begin{aligned} D_T \equiv & \frac{\rho_1\rho_2}{3\rho}\{\mathbf{D},\mathbf{A}\} \\ = & \frac{\rho_1\rho_2}{3\rho^3}\int \mathbf{A}_1 \iiint f_1^{(0)} f_{1'}^{(0)} (\mathbf{D}_1 + \mathbf{D}_{1'} - \mathbf{D}'_1 - \mathbf{D}'_{1'}) b\mathrm{d}b\mathrm{d}\epsilon\mathrm{d}\mathbf{u}_{1'}\mathrm{d}\mathbf{u}_1 \\ & + \frac{\rho_1\rho_2}{6\rho^3}\iiiint f_1^{(0)} f_2^{(0)} (\mathbf{D}_1 + \mathbf{D}_2 - \mathbf{D}'_1 - \mathbf{D}'_2)(\mathbf{A}_1 + \mathbf{A}_2 - \mathbf{A}'_1 - \mathbf{A}'_2) b\mathrm{d}b\mathrm{d}\epsilon\mathrm{d}\mathbf{u}_1\mathrm{d}\mathbf{u}_2 \\ & + \frac{\rho_1\rho_2}{3\rho^3}\int \mathbf{A}_2 \iiint f_2^{(0)} f_{2'}^{(0)} (\mathbf{D}_2 + \mathbf{D}_{2'} - \mathbf{D}'_2 - \mathbf{D}'_{2'}) b\mathrm{d}b\mathrm{d}\epsilon\mathrm{d}\mathbf{u}_{2'}\mathrm{d}\mathbf{u}_2 \end{aligned} \tag{2.23}$$

will be defined, and a method for approximating their value will be introduced.

2.3.1 The Boltzmann-equations

To begin, the Maxwell-Boltzmann equations are derived by assuming that collisions - i.e. interactions between particles, occupy only a very small amount of a particles life time. This gives rise to a differential equation for the velocity distribution function $f_i = f_i(\mathbf{u}_i, \mathbf{r}, t)$, describing the probability of finding a particle of species

i with velocity $\mathbf{u}_i$ at position $\mathbf{r}$ at time t. This equation reads

$$\frac{\partial f_i}{\partial t} + \mathbf{u}_i \nabla f_i + \mathbf{F_i} \frac{\partial f_i}{\partial \mathbf{u}_i} = \frac{\partial_e f_i}{\partial t} \tag{2.24}$$

where $\mathbf{F}$ denotes an external force on the particle and $\frac{\partial_e f}{\partial t}$ describes the rate of change owing to encounters between molecules. The latter of these may be expanded as a sum over the change due to encounters of different types, that is

$$\frac{\partial_e f_i}{\partial t} = \sum_j \left(\frac{\partial_e f_i}{\partial t} \right)_j \tag{2.25}$$

where subscript j denotes the particle type that particle i encounters, and the sum runs over all particle species. To describe this differential, a description of the dynamics of a binary encounter between particles is required. This description is done through a set of rather involved geometric considerations that are difficult to summarise shortly. Therefore, only a summary of the variables involved, their significance and their dependencies are included here, shown graphically in Figure 2.1. Let $\mathbf{g}_{12}$ and $\mathbf{g}_{21}$ denote the initial velocity

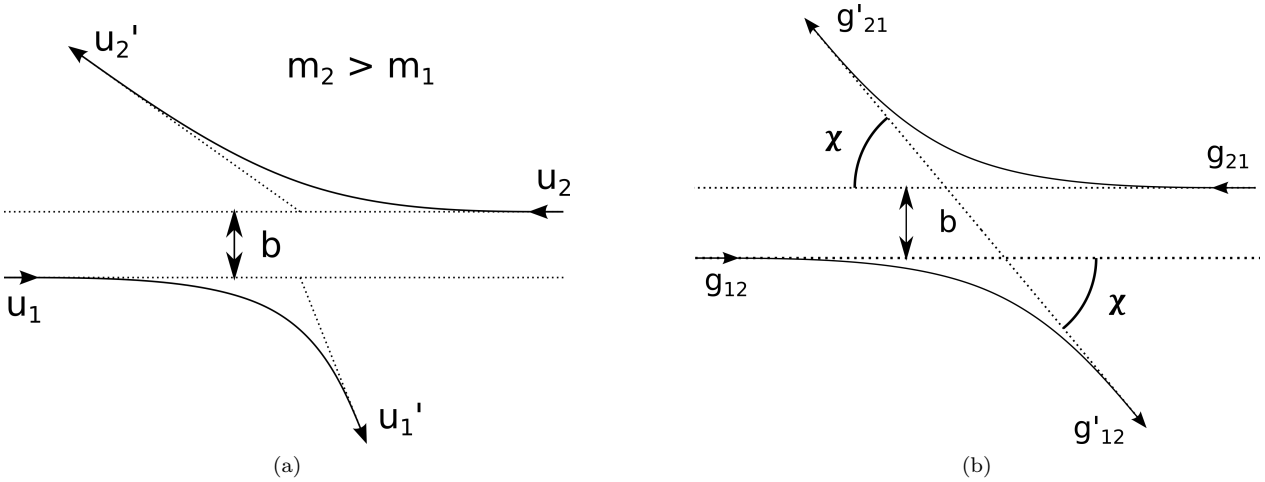

Figure 2.1: The geometry of a binary encounter.

of particle 1 relative to 2, and 2 relative to 1. Evidently $\mathbf{g}_{12} = \mathbf{u}_1 - \mathbf{u}_2 = -\mathbf{g}_{12}$. Primes on the velocities will denote the post-collision velocities, $\mathbf{g}'_{12} = \mathbf{u}'_1 - \mathbf{u}'_2 = -\mathbf{g}'_{12}$. Due to conservation of energy and momentum, the encounter can be completely described by the change in direction of the relative velocities, as the centre of mass velocity is constant. Further, assume that the forces acting between the particles act along the line connecting their centres of mass. For spherical particles this is clearly correct, but for chain-like molecules it cannot be expected to hold.

Now, let χ denote the deflection angle of the relative velocity, that is $\cos\chi = \mathbf{g}_{12} \cdot \mathbf{g}'_{12}$. To describe χ, one must also define the impact parameter b. This can be thought of as the "closest passing distance" the particles would have had if they had been non-interacting point particles, as visualised in Figure 2.1. It is clear that χ is a function of b, and that the functional form is dependent on the intermolecular potential. For a hard-sphere potential, an analytical expression can be derived without extended effort. For other potentials however, the dependency on $\mathbf{g}_{12}$ and the molecular masses requires one to employ numerical methods. For now, χ will be left as some function of $\mathbf{g}_{12}$, b, m_1 and m_2.

Finally, to expand the geometry of Figure 2.1 to three dimensions, define a cylindrical coordinate system centred on particle 1, with the vertical axis perpendicular to $\mathbf{g}_{12}$, such that b takes the role of the radial coordinate. Denote the angular coordinate of this system as ϵ. This coordinate system is shown in Figure 2.2. Following these geometric considerations it can be shown that

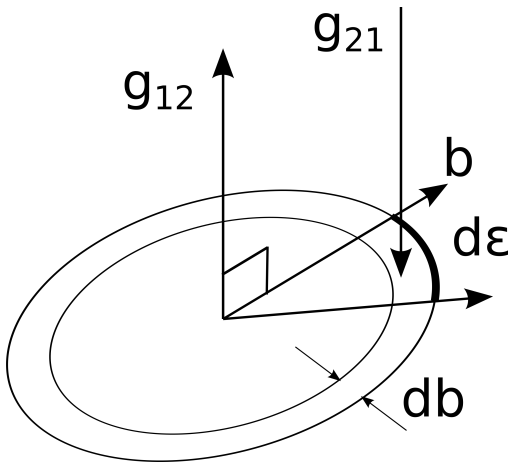

Figure 2.2: Cylindrical coordinate system to describe an encounter.

$$\left(\frac{\partial_e f_i}{\partial t}\right)_j = \iiint \left(f_i' f_j' - f_i f_j\right) b\mathrm{d}b\mathrm{d}\epsilon\mathrm{d}\mathbf{u}_j. \tag{2.26}$$

The truncation of an interaction potential at some distance now amounts to limiting the integral over db to that distance. The case of $i = j$ follows the exact same row of arguments as the case $i \neq j$, but the notation employed can quickly lead to confusion. The integral in Equation (2.26) passes over $\mathbf{u}_j$, and is therefore a function only of $\mathbf{u}_i$. If $i = j$, recognise that the integral still only passes over the velocity of one particle in the colliding pair, such that it is still a function of the velocity of the other particle. Notation-wise Chapman and Cowling solve this by denoting the velocity of the two particles as $\mathbf{u}$ and $\mathbf{u}_i$ and writing

$$\left(\frac{\partial_e f_i}{\partial t}\right)_i = \iiint \left(f_i' f' - f_i f\right) b\mathrm{d}b\mathrm{d}\epsilon\mathrm{d}\mathbf{u}. \tag{2.27}$$

To avoid confusion as to what function f at any time refers to, the notation employed here will denote the velocity of the two particles as $\mathbf{u}_{i'}$ and $\mathbf{u}_i$, such that

$$\left(\frac{\partial_e f_i}{\partial t}\right)_i = \iiint \left(f_i' f_{i'}' - f_i f_{i'}\right) b\mathrm{d}b\mathrm{d}\epsilon\mathrm{d}\mathbf{u}_{i'}. \tag{2.28}$$

For brevity, the integral in equation (2.26) will later be written as

$$-\left(\frac{\partial_e f_i}{\partial t}\right)_j \equiv \begin{cases} J_{ij}(f_i f_j) & i \neq j \\ J_i(f_{i'} f_i) & i = j \end{cases} \tag{2.29}$$

Where the prime in $J_i(f_{i'} f_i)$ indicates the variable of integration, the differentiation will become important later. The left hand side of equation (2.24) will be written as $\mathscr{D}_i f_i$, thus the Boltzmann equation for a single-component (simple) gas reads

$$\mathscr{D}_i f_i + J_i(f_{i'} f_i) = 0 \tag{2.30}$$

2.3.2 The first approximation for a simple gas

Now that the notation and formulation of the Boltzmann-equations has been established, the time is ripe for introducing the Enskog solution method. Assume that the true solution, f, of equation (2.24) can be written as an infinite series $f = \sum_{r=0}^{\infty} f^{(r)}$. The operators $\mathscr{D}$ and J can also be subdivided. First, introduce the operator $\frac{\partial_r}{\partial t}$, with the property

$$\frac{\partial \varphi}{\partial t} \equiv \sum_r \frac{\partial_r \varphi}{\partial t}, \qquad \varphi = \{\rho, T, \mathbf{u}^n\} \tag{2.31}$$

where $\mathbf{u}^n$ denotes the mole average velocity of the gas, and ρ denotes the number density of the gas. For the formal definition of $\frac{\partial_r}{\partial t}$ the reader is referred to Chapman and Cowling, pp. 116.[11] Enskog now subdivides the operator $\mathscr{D}$ such that

$$\begin{aligned} \mathscr{D}_1 f_1 &= \sum_r \mathscr{D}^{(r)}, \qquad \mathscr{D}^{(0)} = 0 \\ \mathscr{D}_1^{(r)} &= \sum_{i=0}^{r-1} \frac{\partial_r f_1^{(r-1-i)}}{\partial t} + \mathbf{u} \cdot \nabla f_1^{(r-1)} + \mathbf{F}_1 \cdot \nabla f_1^{(r-1)}, \qquad r > 0. \end{aligned} \tag{2.32}$$

Similarly, J can be subdivided such that

$$J_1^{(r)} = \sum_{i=0}^{r} J_1(f_{1'}^{(i)} f_1^{(r-i)}). \tag{2.33}$$

It is important to note that this manner of subdividing $\mathscr{D}$ and J is a matter of choice, and that the key to the Enskog solution lies in choosing to subdivide them in this way. The result of the subdivision is that Equation (2.30) may be written as

$$\sum_r \mathscr{D}_1^{(r)} + J_1^{(r)} = 0 \tag{2.34}$$

This equation is fulfilled if $\mathscr{D}_1^{(r)} + J_1^{(r)} = 0, \forall\, r$, and the manner in which $\mathscr{D}$ and J have been subdivided ensures that each of these equations is solvable. The equation corresponding to $r = 0$ becomes $J_1(f_{1'}^{(0)} f_1^{(0)}) = 0$, of which

$$f_1^{(0)} = \exp\left(\alpha^{(1)} + \boldsymbol{\alpha}^{(\mathbf{2})} m\mathbf{u}_1 + \alpha^{(3)} \frac{1}{2} m u_1^2\right) \tag{2.35}$$

is the general solution, with $\alpha^{(1)}, \boldsymbol{\alpha}^{(\mathbf{2})}$ and $\alpha^{(3)}$ arbitrary quantities independent of $\mathbf{u}_1$, and $u_1 = |\mathbf{u}_1|$ is the particle speed. Making some convenient choices for these, yields

$$f_1^{(0)} = \rho \left(\frac{m_1}{2\pi k_B T}\right)^{\frac{3}{2}} \exp\left(-\frac{m_1 U_1^2}{2 k_B T}\right), \tag{2.36}$$

where $\mathbf{U}_i = \mathbf{u}_i - \mathbf{u}^n$ is the peculiar velocity of species i, and U is its magnitude, the peculiar speed. Note that $J_1(f^{(0)} f_1^{(0)}) = 0$ is the exact equation describing a gas in which collisions have no net effect on the velocity distribution function, such that $f^{(0)}$ is the velocity distribution function in a homogeneous (uniform) steady state gas. It is evident then, that to describe a non-uniform state, a solution for the second approximation $f^{(1)}$ must be found. Before moving on, note some properties of the velocity distribution function regarding the *summational invariants*, ρ, $m\mathbf{U}$ and $\frac{1}{2} m U^2$. That is, the number density, momentum and kinetic energy of the gas. These must all be conserved over time. It then follows that

$$\begin{aligned} \int f_1^{(0)} \mathrm{d}\mathbf{u}_1 = \rho_1 = \int f_1 \mathrm{d}\mathbf{u}_1 \\ \int (f_1 - f_1^{(0)}) \mathrm{d}\mathbf{u}_1 = 0 \end{aligned} \tag{2.37}$$

and similarly for the other invariants,

$$\int (f_1 - f_1^{(0)}) \varphi \mathrm{d}\mathbf{u}_1 = 0, \qquad \varphi = \{m\mathbf{U}_1, \frac{1}{2} m U_1^2\}. \tag{2.38}$$

Inserting for $f_1 = \sum_{r=0}^{\infty} f_1^{(r)}$ then yields

$$\sum_{r=1}^{\infty} \int f_1^{(r)} \varphi \mathrm{d}\mathbf{u}_1 = 0, \qquad \varphi = \{1, m\mathbf{U}_1, \frac{1}{2} m U_1^2\}. \tag{2.39}$$

This equation is clearly fulfilled if

$$\int f_1^{(r)} \varphi \mathrm{d}\mathbf{u}_1 = 0 \quad \forall \quad i > 0, \qquad \varphi = \{1, m\mathbf{U}_1, \frac{1}{2} m U_1^2\}. \tag{2.40}$$

2.3.3 The second approximation for a simple gas

It can be shown that a valid second approximation to f can be written on the form $f_1^{(1)} = f_1^{(0)}\Phi_1^{(1)}$. Just like the first approximation, the second approximation satisfies Equation (2.34) if

$$\mathscr{D}_1^{(1)} + J_1^{(1)} = 0. \tag{2.41}$$

Here, $\mathscr{D}^{(1)}$ may be expanded as

$$\begin{aligned}\mathscr{D}_1^{(1)} &= f_1^{(0)}\left[\left(\frac{mU_1^2}{2k_BT} - \frac{5}{2}\right)\mathbf{U}_1\nabla\ln T + \frac{m}{k_BT}\mathbf{U}_1\overset{\circ}{\mathbf{U}}_1 : \nabla\mathbf{u}^n\right] \\ &= f_1^{(0)}\left[\left(\boldsymbol{\mathscr{U}}_1 - \frac{5}{2}\right)\mathbf{U}_1\nabla\ln T + \frac{m}{k_BT}\boldsymbol{\mathscr{U}}_1\overset{\circ}{\boldsymbol{\mathscr{U}}}_1 : \nabla\mathbf{u}^n\right]\end{aligned} \tag{2.42}$$

where for a 3d vector $\mathbf{v}$, $\overset{\circ}{\mathbf{vv}}$ is the operation

$$\overset{\circ}{\mathbf{vv}} = \begin{bmatrix} v_1 & & \\ & v_2 & \\ & & v_3\end{bmatrix}\begin{bmatrix} v_1 & v_2 & v3 \\ v_1 & v_2 & v3 \\ v_1 & v_2 & v3\end{bmatrix} - \frac{1}{3}v^2\underline{\boldsymbol{I}} \tag{2.43}$$

and for two matrices $\underline{\boldsymbol{\phi}}_1 : \underline{\boldsymbol{\phi}}_2 = \phi_{1,ij}\phi_{2,ji} = \sum_i\sum_j a_{ij}b_{ji}$ denotes the double dot product. $\boldsymbol{\mathscr{U}}_i$ is the dimensionless peculiar velocity $\boldsymbol{\mathscr{U}}_i \equiv \left(\frac{m_i}{2k_BT}\right)^{\frac{1}{2}}\mathbf{U}_i$. Further, the term $J^{(1)}$ can be expanded and rewritten as

$$\begin{aligned}J_1^{(1)} &= J_1(f_{1'}^{(0)}f_1^{(1)}) + J_1(f_{1'}^{(1)}f_1^{(0)}) \\ &= \rho^2 I_1\left(\Phi_1^{(1)}\right)\end{aligned} \tag{2.44}$$

where the integral $I_1\left(\Phi_1^{(1)}\right)$ has been introduced.

This is a convenient time to step aside and introduce some integral notation that will be heavily employed later. Recognise how Equations (2.22) and (2.23) are written with exactly this integral notation. Let F and G be functions defined on $\mathbf{u}_1$ and K be a function defined on $\mathbf{u}_1$ and $\mathbf{u}_2$. Then, using the notation $F_i = F(\mathbf{u}_i)$ and $K_{ij} = K_{ji} = K(\mathbf{u}_i, \mathbf{u}_j)$,

$$\begin{aligned}\rho_1^2 I_1(F) &\equiv \iiint f_1^{(0)}f_{1'}^{(0)}\left(F_1 + F_{1'} - F_1' - F_{1'}'\right)gb\mathrm{d}b\mathrm{d}\epsilon\mathrm{d}\mathbf{u}_{1'} \\ \rho_2^2 I_2(F) &\equiv \iiint f_2^{(0)}f_{2'}^{(0)}\left(F_2 + F_{2'} - F_2' - F_{2'}'\right)gb\mathrm{d}b\mathrm{d}\epsilon\mathrm{d}\mathbf{u}_{2'} \\ \rho_1\rho_2 I_{12}(K) &\equiv \iiint f_1^{(0)}f_2^{(0)}\left(K_{12} - K_{12}'\right)gb\mathrm{d}b\mathrm{d}\epsilon\mathrm{d}\mathbf{u}_2 \\ \rho_1\rho_2 I_{21}(K) &\equiv \iiint f_1^{(0)}f_2^{(0)}\left(K_{12} - K_{12}'\right)gb\mathrm{d}b\mathrm{d}\epsilon\mathrm{d}\mathbf{u}_1\end{aligned} \tag{2.45}$$

Note that $I_1(F)$ and $I_{12}(K)$ are functions of $\mathbf{u}_1$, while $I_2(F)$ and $I_{21}(K)$ are functions of $\mathbf{u}_2$. Further define the bracket integrals

$$[F, G]_i \equiv \int G_i I_i(F)\mathrm{d}\mathbf{u}_i, \qquad i = \{1, 2\} \tag{2.46}$$

For functions F and H defined on $\mathbf{u}_1$, and G and K defined on $\mathbf{u}_2$, define

$$[F_1 + G_2, H_1 + K_2]_{12} \equiv \int F_1 I_{12}(H_1 + K_2)\mathrm{d}\mathbf{u}_1 + \int G_2 I_{21}(H_1 + K_2)\mathrm{d}\mathbf{u}_2 \tag{2.47}$$

Expanding Equation (2.47), one quickly sees that $[F_1 + G_2, H_1 + K_2]_{12} = [H_1 + K_2, F_1 + G_2]_{12}$. Finally, for functions F and G both defined on $\mathbf{u}_1$ and $\mathbf{u}_2$, define the bracket integral

$$\rho^2\{F, G\} = \rho_1^2[F, G]_1 + \rho_1\rho_2[F_1 + F_2, G_1 + G_2]_{12} + \rho^2[F, G]_2. \tag{2.48}$$

Returning to the problem of determining the second approximation $f_1^{(1)} = f_1^{(0)}\Phi_1^{(1)}$, inserting Equations (2.44) and (2.42) into Equation (2.41) yields

$$\rho^2 I_1\left(\Phi_1^{(1)}\right) = -f_1^{(0)}\left[\left(\mathscr{U}_1{}^2 - \frac{5}{2}\right)\mathbf{U}_1\nabla\ln T + \frac{m}{k_B T}\boldsymbol{\mathscr{U}}_1\overset{\circ}{\boldsymbol{\mathscr{U}}}_1 : \nabla\mathbf{u}^n\right]. \tag{2.49}$$

Observe that $I_1\left(\Phi_1^{(1)}\right)$ is linear in $\Phi_1^{(1)}$, and that the right hand side of this equation is linear in the components of $\nabla\ln T$ and $\mathbf{u}^n$. Thereby, $\Phi_1^{(1)}$ can be written as a linear combination of the components of $\nabla\ln T$ and $\mathbf{u}^n$ and the solution to the equation $I_1\left(\Phi_1^{(1)}\right) = 0$. The latter can be recognised as a solution of the form in equation (2.35), such that for some vector $\mathbf{A}$, matrix $\underline{\boldsymbol{B}}$, and constants $\alpha^{(1,1)}, \boldsymbol{\alpha}^{(\mathbf{2,1})}, \alpha^{(3,1)}$

$$\Phi_1^{(1)} = -\frac{1}{\rho}\left(\frac{2k_B T}{m_1}\right)^{\frac{1}{2}}\mathbf{A}\nabla\ln T - \frac{2}{\rho}\underline{\boldsymbol{B}} : \nabla\mathbf{u}^n + \alpha^{(1,1)} + \boldsymbol{\alpha}^{(\mathbf{2,1})}m_1\mathbf{u}_1 + \alpha^{(3,1)}\frac{1}{2}m_1 U_1^2, \tag{2.50}$$

Where the prefactors to $\mathbf{A}$ and $\underline{\boldsymbol{B}}$ are chosen for later convenience. Substituting this into equation (2.49), using the fact that $I_1(F + G) = I_1(F) + I_1(G)$, and equating the coefficients to each of the gradient terms yields a set of equations for $\mathbf{A}$ and $\underline{\boldsymbol{B}}$,

$$\begin{aligned}\rho I_1(\mathbf{A}) &= f_1^{(0)}\left(\mathscr{U}_1{}^2 - \frac{5}{2}\right)\boldsymbol{\mathscr{U}} \\ \rho I_1(\underline{\boldsymbol{B}}) &= f_1^{(0)}\boldsymbol{\mathscr{U}}_1\overset{\circ}{\boldsymbol{\mathscr{U}}}_1.\end{aligned} \tag{2.51}$$

It is clear from the first of these equations that $\mathbf{A}$ must be a vector parallel to $\boldsymbol{\mathscr{U}}$, such that one can write

$$\mathbf{A} = A(\mathscr{U}, \rho, T)\boldsymbol{\mathscr{U}}, \tag{2.52}$$

where $\mathscr{U} \equiv |\boldsymbol{\mathscr{U}}|$ is the dimensionless peculiar speed. It is less clear, but can be shown, that $\underline{\boldsymbol{B}}$ is a symmetric, traceless matrix. All symmetric, traceless matrices that can be formed from $\boldsymbol{\mathscr{U}}$ are multiples of $\boldsymbol{\mathscr{U}}_1\overset{\circ}{\boldsymbol{\mathscr{U}}}_1$. Therefore, $\underline{\boldsymbol{B}}$ can be written as

$$\underline{\boldsymbol{B}} = B(\mathscr{U}, \rho, T)\boldsymbol{\mathscr{U}}_1\overset{\circ}{\boldsymbol{\mathscr{U}}}_1. \tag{2.53}$$

The constants $\alpha^{(1,1)}, \boldsymbol{\alpha}^{(\mathbf{2,1})}$ and $\alpha^{(3,1)}$ can be chosen such that $f_1^{(1)}$ satisfies the constraints posed by the summational invariants, from Equation (2.40). Analysing these constraints, one finds that $\alpha^{(1,1)} = \boldsymbol{\alpha}^{(\mathbf{2,1})} = \alpha^{(3,1)} = 0$ is a valid choice. Equation (2.50) then reduces to

$$\Phi_1^{(1)} = -\frac{1}{\rho_1}\left(\frac{2k_B T}{m_1}\right)^{\frac{1}{2}}\mathbf{A}\nabla\ln T - \frac{2}{\rho}\underline{\boldsymbol{B}} : \nabla\mathbf{u}^n. \tag{2.54}$$

Until now, for pedagogical reasons, only a simple gas has been considered. The method for arriving at Equation (2.54) for a binary system follows the exact same steps as those presented so far. Because the goal of this section is to describe diffusion, we now move to a binary case and in short words describe how the equation for $\Phi_1^{(1)}$ will differ from Equation (2.54).

2.3.4 The binary solutions

The Boltzmann equations for a binary system are directly analogous to that for a unary system,

$$\frac{\partial f_i}{\partial t} + \mathbf{u}\nabla f_i + \mathbf{F_i}\frac{\partial f_i}{\partial \mathbf{u}} = \frac{\partial_e f_i}{\partial t}, \qquad i = \{1, 2\}. \tag{2.55}$$

Rewriting this in terms of the operators $\mathscr{D}$ and J gives

$$\begin{aligned} \mathscr{D}_1 f_1 + J_1(f_1 f_{1'}) + J_{12}(f_1 f_2) = 0 \\ \mathscr{D}_2 f_2 + J_2(f_2 f_{2'}) + J_{21}(f_2 f_1) = 0 \end{aligned} \tag{2.56}$$

The subdivision of f_i and $\mathscr{D}_i$ follow the same procedure as the one outlined in the unary case. For J_i, the function $J_i^{(r)}$ takes the form

$$J_i^{(r)} \equiv \sum_{k=0}^{r} J_i(f_i^{(k)} f_{i'}^{(r-k)}) + J_{ij}(f_i^{(k)} f_j^{(r-k)}). \tag{2.57}$$

Again, requiring that $\mathscr{D}_i^{(r)} + J_i^{(r)} = 0 \ \forall \ r$ gives solutions to the first approximation identical to Equation (2.36). In the solution of the second approximation, a difference turns up. Inserting $f_1^{(1)} = f_1^{(0)}\Phi_1^{(1)}$ and $f_2^{(1)} = f_2^{(0)}\Phi_2^{(1)}$ into the expression for $J_1^{(1)}$ yields

$$J_1^{(1)} = \rho_1^2 I_1(\Phi_1^{(1)}) + \rho_1\rho_2 I_{12}(\Phi_1^{(1)} + \Phi_2^{(1)}). \tag{2.58}$$

Expanding $\mathscr{D}_1^{(1)}$ now yields

$$\mathscr{D}_1^{(1)} = f_1^{(0)}\left[\left(\boldsymbol{\mathscr{U}}_1 - \frac{5}{2}\right)\mathbf{U}_1\nabla\ln T + \frac{m}{k_B T}\boldsymbol{\mathscr{U}}_1\overset{\circ}{\boldsymbol{\mathscr{U}}}_1 : \nabla\mathbf{u}^n + x_1^{-1}\mathbf{d}_{12}\mathbf{U}_1\right] \tag{2.59}$$

Where the only difference from Equation (2.42) is the appearance of the trailing term

$$\mathbf{d}_{12} \equiv \nabla x_1 + \frac{\rho_1\rho_2(m_2 - m_1)}{\rho\rho_m}\nabla\ln p - \frac{\rho_{m,1}\rho_{m,2}}{\rho_m p}\left(\mathbf{F}_1 - \mathbf{F}_2\right), \tag{2.60}$$

where x_i denotes the mole fraction of species i, and ρ_m denotes the mass density. Just as in the previous section, it is now clear that $\Phi_1^{(1)}$ and $\Phi_2^{(1)}$ must be linear functions of $\nabla\ln T$, $\mathbf{d}_{12}$ and $\nabla\mathbf{u}^n$. Therefore, for some $\mathbf{A}$, $\mathbf{D}$ and $\underline{\boldsymbol{B}}$, the $\Phi_i^{(1)}$ may be written as

$$\Phi_i^{(1)} = -\mathbf{A}_i\nabla\ln T - \mathbf{D}_i\mathbf{d}_{12} - 2\underline{\boldsymbol{B}}_i : \nabla\mathbf{u}^n, \qquad i = \{1, 2\} \tag{2.61}$$

Inserting Equations (2.61) and (2.59) for $\Phi_i^{(1)}$ and $\mathscr{D}_i^{(1)}$ into Equations (2.56) and matching the coefficients of the gradients now leads to a set of equations that determine $\mathbf{A}$, $\mathbf{D}$ and $\underline{\boldsymbol{B}}$, analogous to Equations (2.51),

$$\begin{aligned} f_1^{(0)}(\boldsymbol{\mathscr{U}}_1^2 - \frac{5}{2})\mathbf{U}_1 &= \rho_1^2 I_1(\mathbf{A}_1) + \rho_1\rho_2 I_{12}(\mathbf{A}_1 + \mathbf{A}_2) \\ f_2^{(0)}(\boldsymbol{\mathscr{U}}_2^2 - \frac{5}{2})\mathbf{U}_2 &= \rho_2^2 I_2(\mathbf{A}_2) + \rho_2\rho_1 I_{21}(\mathbf{A}_2 + \mathbf{A}_1) \\ x_1^{-1} f_1^{(0)}\mathbf{U}_1 &= \rho_1^2 I_1(\mathbf{D}_1) + \rho_1\rho_2 I_{12}(\mathbf{D}_1 + \mathbf{D}_2) \\ -x_2^{-1} f_2^{(0)}\mathbf{U}_2 &= \rho_2^2 I_2(\mathbf{D}_2) + \rho_2\rho_1 I_{21}(\mathbf{D}_2 + \mathbf{D}_1) \\ f_1^{(0)}\boldsymbol{\mathscr{U}}_1\overset{\circ}{\boldsymbol{\mathscr{U}}}_1 &= \rho_1^2 I_1(\underline{\boldsymbol{B}}_1) + \rho_1\rho_2 I_{12}(\underline{\boldsymbol{B}}_1 + \underline{\boldsymbol{B}}_2) \\ f_2^{(0)}\boldsymbol{\mathscr{U}}_2\overset{\circ}{\boldsymbol{\mathscr{U}}}_2 &= \rho_2^2 I_2(\underline{\boldsymbol{B}}_2) + \rho_2\rho_1 I_{21}(\underline{\boldsymbol{B}}_2 + \underline{\boldsymbol{B}}_1) \end{aligned} \tag{2.62}$$

Thus, to a second approximation, the velocity distribution function is given as

$$\begin{aligned} f_i &= f_i^{(0)}(1+\Phi_i^{(1)}), \qquad i=\{1,2\} \\ &= f_i^{(0)}\left[1-\mathbf{A}_i\nabla\ln T-\mathbf{D}_i\mathbf{d}_{12}-2\underline{\boldsymbol{B}}_i:\nabla\mathbf{u}^n\right]. \end{aligned} \tag{2.63}$$

Note that $\mathbf{A}$, $\mathbf{D}$ and $\underline{\boldsymbol{B}}$ have been established to be unique, but determining their exact functional form still remains.

2.3.5 Diffusion

Now that an expression for the velocity distribution function has been obtained, the analysis of diffusion can begin. The two components of a mixture are diffusing relative to each other if $\bar{\mathbf{u}}_1-\bar{\mathbf{u}}_2\equiv\bar{\mathbf{U}}_1-\bar{\mathbf{U}}_2\neq 0$. Where the bar denotes the mean values of the velocity. From the velocity distribution function, the differences in mean velocity are

$$\bar{\mathbf{U}}_1-\bar{\mathbf{U}}_2=\frac{1}{\rho_1}\int f_1\mathbf{U}_1\mathrm{d}\mathbf{u}_1-\frac{1}{\rho_2}\int f_2\mathbf{U}_2\mathrm{d}\mathbf{u}_2. \tag{2.64}$$

Inserting the velocity distribution function from Equation (2.63), and noting that $f_i^{(0)}\mathbf{U}$, and $\underline{\boldsymbol{B}}_i:\nabla\mathbf{u}^n\mathbf{U}$ are odd functions such that their integrals vanish yields

$$\begin{aligned} \bar{\mathbf{U}}_1-\bar{\mathbf{U}}_2=-\frac{1}{3}\Bigg[&\left(\frac{1}{\rho_1}\int f_1^{(0)}\mathbf{U}_1\mathbf{D}_1\mathrm{d}\mathbf{u}_1-\frac{1}{\rho_2}\int f_2^{(0)}\mathbf{U}_2\mathbf{D}_2\mathrm{d}\mathbf{u}_2\right)\mathbf{d}_{12} \\ &+\left(\frac{1}{\rho_1}\int f_1^{(0)}\mathbf{U}_1\mathbf{A}_1\mathrm{d}\mathbf{u}_1-\frac{1}{\rho_2}\int f_2^{(0)}\mathbf{U}_2\mathbf{A}_2\mathrm{d}\mathbf{u}_2\right)\nabla\ln T\Bigg] \end{aligned} \tag{2.65}$$

Now, from Equations (2.62) it can be shown that for any vector function $\mathbf{a}$ defined on $\mathbf{u}_1$ and $\mathbf{u}_2$,

$$\begin{aligned} \rho^2\{\mathbf{A},\mathbf{a}\}&=\int f_1^{(0)}(\mathscr{U}_1^2-\frac{5}{2})\mathbf{U}_1\mathbf{a}_1\mathrm{d}\mathbf{u}_1+\int f_2^{(0)}(\mathscr{U}_2^2-\frac{5}{2})\mathbf{U}_2\mathbf{a}_2\mathrm{d}\mathbf{u}_2 \\ \rho^2\{\mathbf{D},\mathbf{a}\}&=x_1^{-1}\int f_1^{(0)}\mathbf{U}_1\mathbf{a}_1\mathrm{d}\mathbf{u}_1-x_2^{-1}\int f_2^{(0)}\mathbf{U}_2\mathbf{a}_2\mathrm{d}\mathbf{u}_2. \end{aligned} \tag{2.66}$$

Since $\mathbf{A}$ and $\mathbf{D}$ are exactly such vector functions, Equation (2.65) may be contracted to

$$\bar{\mathbf{U}}_1-\bar{\mathbf{U}}_2=-\frac{1}{3}\rho\left[\{\mathbf{D},\mathbf{D}\}\mathbf{d}_{12}+\{\mathbf{D},\mathbf{A}\}\nabla\ln T\right]. \tag{2.67}$$

Considering the cases in which either $\mathbf{d}_{12}=0$ or $\nabla T=\mathbf{F}_1=\mathbf{F}_2=\nabla p=0$ allows us to define the interdiffusion coefficient D_{12} and the thermal diffusion coefficient D_T for a binary mixture. In the first case,

$$\begin{aligned} \bar{\mathbf{u}}_1-\bar{\mathbf{u}}_2&=-\frac{\rho^2}{\rho_1\rho_2}D_T\nabla\ln T, \qquad \mathbf{d}_{12}=0 \\ &=-\frac{D_T}{x_1x_2}\nabla\ln T \\ D_T&\equiv\frac{\rho_1\rho_2}{3\rho}\{\mathbf{D},\mathbf{A}\} \end{aligned} \tag{2.68}$$

and in the second,

$$\begin{aligned} \bar{\mathbf{u}}_1-\bar{\mathbf{u}}_2&=-\frac{\rho^2}{\rho_1\rho_2}D_{12}\nabla x_1, \qquad \nabla T=\mathbf{F}_1=\mathbf{F}_2=\nabla p=0 \\ &=-\frac{D_{12}}{x_1x_2}\nabla x_1 \\ D_{12}&\equiv\frac{\rho_1\rho_2}{3\rho}\{\mathbf{D},\mathbf{D}\}. \end{aligned} \tag{2.69}$$

Additionally, the thermal diffusion ratio may be defined as

$$k_T \equiv \frac{D_T}{D_{12}} = \frac{\{\mathbf{D}, \mathbf{A}\}}{\{\mathbf{D}, \mathbf{D}\}} \tag{2.70}$$

To acquire values for the diffusion coefficients, it is thereby necessary to evaluate the integrals $\{\mathbf{D}, \mathbf{D}\}$ and $\{\mathbf{D}, \mathbf{A}\}$. To accomplish this, first introduce the auxiliary function $\tilde{\mathbf{A}}_i = \mathbf{A}_i - k_T \mathbf{D}_i$, then write the functions $\tilde{\mathbf{A}}_i$ and $\mathbf{D}_i$ as polynomial expansions using an orthogonal set of polynomials known as the Sonine polynomials, denoted $S_m^{(n)}(\varphi)$. These have the property

$$\int_0^\infty e^{-\varphi} S_m^{(p)}(\varphi) S_m^{(q)}(\varphi) \varphi^m d\varphi = \frac{\Gamma(m+p+1)}{p!} \delta_{pq} \tag{2.71}$$

where Γ denotes the gamma function and δ_{pq} is the Kronecker delta. $\mathbf{D}$ and $\tilde{\mathbf{A}}$ are expanded as

$$\mathbf{D}_1 = \sum_{p=-\infty}^{\infty} d_p \mathbf{a}_1^{(p)} \qquad \mathbf{D}_2 = \sum_{p=-\infty}^{\infty} d_p \mathbf{a}_2^{(p)} \tag{2.72}$$

$$\tilde{\mathbf{A}}_1 = \sum_{\substack{p=-\infty \\ p \neq 0}}^{\infty} a_p \mathbf{a}_1^{(p)} \qquad \tilde{\mathbf{A}}_2 = \sum_{\substack{p=-\infty \\ p \neq 0}}^{\infty} a_p \mathbf{a}_2^{(p)} \tag{2.73}$$

where

$$\mathbf{a}_1^{(p)} \equiv 0 \qquad \mathbf{a}_2^{(p)} \equiv S_{3/2}^{(p)}\left(\mathscr{U}_2^2\right) \boldsymbol{\mathscr{U}}_2 \qquad p < 0 \tag{2.74}$$

$$\mathbf{a}_1^{(0)} \equiv M_1^{\frac{1}{2}} \rho_{m,2} \rho_m^{-1} \boldsymbol{\mathscr{U}}_1 \qquad \mathbf{a}_2^{(0)} \equiv -M_2^{\frac{1}{2}} \rho_{m,1} \rho_m^{-1} \boldsymbol{\mathscr{U}}_2 \qquad p = 0 \tag{2.75}$$

$$\mathbf{a}_1^{(p)} \equiv S_{3/2}^{(p)}\left(\mathscr{U}_1^2\right) \boldsymbol{\mathscr{U}}_1 \qquad \mathbf{a}_2^{(p)} \equiv 0 \qquad p > 0 \tag{2.76}$$

Now, recall from Equation (2.66) that for any vector function $\mathbf{a}_i^{(p)}$, we may write

$$\rho^2 \{\mathbf{D}, \mathbf{a}^{(p)}\} = x_1^{-1} \int f_1^{(0)} \mathbf{U}_1 \mathbf{a}_1^{(p)} \mathrm{d}\mathbf{u}_1 - x_2^{-1} \int f_2^{(0)} \mathbf{U}_2 \mathbf{a}_2^{(p)} \mathrm{d}\mathbf{u}_2. \tag{2.77}$$

this integral can be evaluated analytically to give

$$\{\mathbf{D}, \mathbf{a}^{(p)}\} = \delta_p, \qquad \delta_p = \begin{cases} \frac{3}{2\rho}\left(\frac{2k_B T}{m_0}\right)^{\frac{1}{2}}, & p = 0 \\ 0, & p \neq 0, \end{cases}. \tag{2.78}$$

where $m_0 = m_1 + m_2$. Thus, by substituting the expansion of $\mathbf{D}$ from Equation (2.73), and utilising the orthogonality properties of the Sonine polynomials,

$$\sum_{p=-\infty}^{\infty} d_p \{\mathbf{a}^{(p)}, \mathbf{a}^{(q)}\} = \delta_q. \tag{2.79}$$

Exposing the integral $\{\tilde{\mathbf{A}}, \mathbf{a}^{(p)}\}$ to the same procedure yields

$$\sum_{\substack{p=-\infty \\ p \neq 0}}^{\infty} a_p \{\mathbf{a}^{(p)}, \mathbf{a}^{(q)}\} = \alpha_q, \qquad \alpha_q = \begin{cases} -\frac{15}{4}\frac{\rho_1}{\rho^2}\left(\frac{2k_B T}{m_1}\right)^{\frac{1}{2}} & q = 1 \\ 0 & q \neq \pm 1 \\ -\frac{15}{4}\frac{\rho_2}{\rho^2}\left(\frac{2k_B T}{m_2}\right)^{\frac{1}{2}} & q = -1 \end{cases} \tag{2.80}$$

These sets of linear equations uniquely determine the d_p and a_p, and thereby uniquely determine the functions $\mathbf{D}$, $\tilde{\mathbf{A}}$ and $\mathbf{A}$. For a finite approximation $|p| < N$, $|q| < N$, termed the Nth-order approximation, they may be written in matrix form as

$$\begin{bmatrix} a_{-N-N} & \dots & a_{-N0} & \dots & a_{-NN} \\ \vdots & \ddots & \vdots & & \vdots \\ a_{0-N} & \dots & a_{00} & \dots & a_{0N} \\ \vdots & & \vdots & \ddots & \vdots \\ a_{N-N} & \dots & a_{N0} & \dots & a_{NN} \end{bmatrix} \begin{pmatrix} d_{-N} \\ \vdots \\ d_0 \\ \vdots \\ d_N \end{pmatrix} = \begin{pmatrix} 0 \\ \vdots \\ 0 \\ \delta_0 \\ 0 \\ \vdots \\ 0 \end{pmatrix}, \tag{2.81}$$

$$\begin{bmatrix} a_{-N-N} & \dots & a_{-N-1} & a_{-N1} & \dots & a_{-NN} \\ \vdots & \ddots & \vdots & \vdots & & \vdots \\ a_{-1-N} & \dots & a_{-1-1} & a_{-11} & \dots & a_{-1N} \\ a_{1-N} & \dots & a_{1-1} & a_{11} & \dots & a_{1N} \\ \vdots & & \vdots & \vdots & \ddots & \vdots \\ a_{N-N} & \dots & a_{N-1} & a_{N1} & \dots & a_{NN} \end{bmatrix} \begin{pmatrix} a_{-N} \\ \vdots \\ a_{-1} \\ a_1 \\ \vdots \\ a_N \end{pmatrix} = \begin{pmatrix} 0 \\ \vdots \\ 0 \\ \alpha_{-1} \\ \alpha_1 \\ 0 \\ \vdots \\ 0 \end{pmatrix}, \tag{2.82}$$

Where $a_{pq} \equiv \{\mathbf{a}^{(p)}, \mathbf{a}^{(q)}\} = a_{qp}$. Further, inserting the expansions of $\mathbf{D}$ and $\tilde{\mathbf{A}}$ into the integrals $\{\mathbf{D}, \mathbf{D}\}$ and $\{\tilde{\mathbf{A}}, \tilde{\mathbf{A}}\}$ one arrives at

$$\{\mathbf{D}, \mathbf{D}\} = d_0\delta_0, \qquad \{\tilde{\mathbf{A}}, \tilde{\mathbf{A}}\} = a_1\alpha_1 + a_{-1}\alpha_{-1}, \qquad \{\mathbf{D}, \mathbf{A}\} = d_1\alpha_1 + d_{-1}\alpha_{-1}. \tag{2.83}$$

This means that evaluating the integrals a_{pq} is the final step to obtaining the diffusion coefficients. Recognise that when looking through all the nested notation that has been introduced, a_{pq} is simply the integral of two orthogonal polynomials. By all means, it is an octuple integral over six velocities and two collision parameters, but given an intermolecular potential it is essentially a number that can be evaluated (numerically if need be). The major issue is that the number of integrals that must be evaluated, and the complexity of these integrals, increases rapidly as one increases the order of approximation of $\mathbf{D}$ and $\mathbf{A}$, i.e. uses more polynomials in their expansions.

2.3.6 The summational expressions

To evaluate the integral $\{\mathbf{a}^{(p)}, \mathbf{a}^{(q)}\}$, Chapman and Cowling begin by inserting the definitions of $\mathbf{a}^{(p)}$ into the integral, and simplifying the expressions by using the orthogonality properties of the polynomials. This gives expressions for a_{pq} in terms of the square bracket integrals

$$\begin{aligned} a_{pq} &= x_1^2 \left[S_{3/2}^{(p)}(\mathscr{U}_1^2)\boldsymbol{\mathscr{U}}_1, S_{3/2}^{(q)}(\mathscr{U}_1^1)\boldsymbol{\mathscr{U}}_1 \right]_1 + x_1x_2 \left[S_{3/2}^{(p)}(\mathscr{U}_1^1)\boldsymbol{\mathscr{U}}_1, S_{3/2}^{(q)}(\mathscr{U}_1^2)\boldsymbol{\mathscr{U}}_1 \right]_{12} \\ a_{p-q} &= x_1x_2 \left[S_{3/2}^{(p)}(\mathscr{U}_1^2)\boldsymbol{\mathscr{U}}_1, S_{3/2}^{(q)}(\mathscr{U}_2^2)\boldsymbol{\mathscr{U}}_2 \right]_{12} \\ a_{-pq} &= x_1x_2 \left[S_{3/2}^{(p)}(\mathscr{U}_2^2)\boldsymbol{\mathscr{U}}_2, S_{3/2}^{(q)}(\mathscr{U}_1^2)\boldsymbol{\mathscr{U}}_1 \right]_{21} \\ a_{-p-q} &= x_2^2 \left[S_{3/2}^{(p)}(\mathscr{U}_2^2)\boldsymbol{\mathscr{U}}_2, S_{3/2}^{(q)}(\mathscr{U}_2^2)\boldsymbol{\mathscr{U}}_2 \right]_2 + x_1x_2 \left[S_{3/2}^{(p)}(\mathscr{U}_2^1)\boldsymbol{\mathscr{U}}_2, S_{3/2}^{(q)}(\mathscr{U}_2^2)\boldsymbol{\mathscr{U}}_2 \right]_{21}. \end{aligned} \tag{2.84}$$

It is noted from the symmetry properties of the square bracket integrals that only the evaluation of

$$\begin{aligned} H_1^{(1)}(p,q) &\equiv \left[S_{3/2}^{(p)}(\mathscr{U}_1^2)\boldsymbol{\mathscr{U}}_1, S_{3/2}^{(q)}(\mathscr{U}_1^1)\boldsymbol{\mathscr{U}}_1\right]_1 \\ H_{12}^{(1)}(p,q) &\equiv \left[S_{3/2}^{(p)}(\mathscr{U}_1^1)\boldsymbol{\mathscr{U}}_1, S_{3/2}^{(q)}(\mathscr{U}_1^2)\boldsymbol{\mathscr{U}}_1\right]_{12} \\ H_{12}^{(12)}(p,q) &\equiv \left[S_{3/2}^{(p)}(\mathscr{U}_1^2)\boldsymbol{\mathscr{U}}_1, S_{3/2}^{(q)}(\mathscr{U}_2^2)\boldsymbol{\mathscr{U}}_2\right]_{12} \end{aligned} \tag{2.85}$$

is required, and the rest can be obtained by index swapping. Recognise now that all information about the intermolecular potential is contained in the integral over $\mathrm{d}b\mathrm{d}\epsilon$, while the integrals over velocity may be carried out without specifying any such potential. It is therefore convenient to define the *collision integrals* $\Omega_{12}^{(\ell)}(r)$ and $\Omega_i^{(\ell)}(r)$, $i = \{1,2\}$

$$\begin{aligned} \Omega_{12}^{(\ell)}(r) &\equiv \frac{1}{2}\sigma_1 2^2 \left(\frac{k_B T}{2\pi m_0 M_1 M_2}\right)^{\frac{1}{2}} W_{12}^{(\ell)}(r) \\ W_{12}^{(\ell)}(r) &\equiv \int_0^\infty \exp(-\mathfrak{g}^2)\mathfrak{g}^{2r+3} \int_0^\pi \left(1-\cos^l(\chi)\right)\left(\frac{b}{\sigma_{12}}\right) d\left(\frac{b}{\sigma_{12}}\right) d\mathfrak{g}_{21} \end{aligned} \tag{2.86}$$

where $\mathfrak{g}_{21} = \left(\frac{m_0 M_1 M_2}{2k_B T}\right)^{\frac{1}{2}} \mathbf{g_{21}}$ is the non-dimensional relative velocity, and a change of integration variables has been employed to map $\mathrm{d}b\mathrm{d}\epsilon \mapsto d\left(\frac{b}{\sigma_{12}}\right) d\mathfrak{g}_{21}$. The equivalent expression for $\Omega_i^{(\ell)}(r)$ is

$$\Omega_i^{(\ell)}(r) \equiv \sigma_i^2 \left(\frac{\pi k_B T}{m_1}\right)^{\frac{1}{2}} W_i^{(\ell)}(r), \qquad i = \{1,2\} \tag{2.87}$$

where $W_i^{(\ell)}(r)$ is obtained simply by replacing σ_{12} with σ_i in Equation (2.86). The collision integrals can be evaluated numerically for any given intermolecular potential, by using this potential to relate χ to b and $\mathfrak{g}$, as described in detail by Chapman and Cowling pp. 167.[11] In addition, Reid et al. give several methods of approximating the collision integrals under various conditions.[20] However, for a HS-potential the integrals can be evaluated analytically to give

$$\begin{aligned} \Omega_1^{(\ell),HS}(r) &= (\sigma_1^{HS})^2 \left(\frac{\pi k_B T}{m_1}\right)^{\frac{1}{2}} W_r^{(\ell),HS} \\ \Omega_2^{(\ell),HS}(r) &= (\sigma_2^{HS})^2 \left(\frac{\pi k_B T}{m_2}\right)^{\frac{1}{2}} W_r^{(\ell),HS} \\ \Omega_{12}^{(\ell),HS}(r) &= \frac{1}{2}(\sigma_{12}^{HS})^2 \left(\frac{2\pi k_B T}{m_0 M_1 M_2}\right)^{\frac{1}{2}} W_r^{(\ell),HS} \\ W_r^{(\ell),HS} &= \frac{1}{4}\left[2 - \frac{1}{l+1}\left(1+(-1)^l\right)\right](r+1)!. \end{aligned} \tag{2.88}$$

Having defined the collision integrals, Chapman and Cowling expand the integrals over $\mathbf{u}_1$ and $\mathbf{u}_2$ and determine that the complete integrals may be written as linear combinations of the collision integrals,

$$\begin{aligned} H_1^{(1)}(p,q) &= 8 \sum_{l=2}^{(\min[p,q]+1)} \sum_{r=l}^{(p+q+2-\ell)} A'''_{pqr\ell}\Omega_1^{(\ell)}(r) \\ H_{12}^{(1)}(p,q) &= 8 \sum_{l=1}^{(\min[p,q]+1)} \sum_{r=l}^{(p+q+2-\ell)} A'_{pqr\ell}\Omega_{12}^{(\ell)}(r) \\ H_{12}^{(12)}(p,q) &= 8M_2^{(p+\frac{1}{2})}M_1^{(q+\frac{1}{2})} \sum_{l=1}^{(\min[p,q]+1)} \sum_{r=l}^{(p+q+2-l)} A_{pqr\ell}\Omega_{12}^{(\ell)}(r) \end{aligned} \tag{2.89}$$

with $A_{pqr\ell}$, $A'''_{pqr\ell}$ as yet undetermined weights, independent of any molecular properties. $A'_{pqr\ell}$ is an undetermined number that is a function of the particle masses. Identifying explicit expressions for these weights is an abnormally extensive exercise in analytical integration and pattern matching that was carried out by Thompson et al.[28–31] For the derivation the reader is referred to their papers. The results they give are

$$\begin{aligned} A'''_{pqr\ell} = \left(\frac{1}{2}\right)^{(p+q+1)} \sum_{i=(l-1)}^{(\min[p,q,r,(p+q+1-r)])} & \frac{8^i (p+q-2i)!\left(1+(-1)^l\right)}{(p-i)!(q-i)!(\ell)!(i+1-l)!} \\ & \times \frac{(-1)^{(r+i)}(r+1)!(2(p+q+2-i))!2^{2r}}{(r-i)!(p+q+1-i-r)!(2r+2)!(p+q+2-i)!4^{(p+q+1)}} \\ & \times [(i+1-l)(p+q+1-i-r)-\ell(r-i)] \end{aligned} \tag{2.90}$$

$$\begin{aligned} A'_{pqr\ell} = & \sum_{i=(l-1)}^{\min[p,q,r,(p+q+1-r)]} \sum_{k=(l-1)}^{\min[l,i]} \sum_{w=0}^{(\min[p,q,(p+q+1-r)]-i)} \frac{8^i (p+q-2i-w)!}{(p-i-w)!(q-i-w)!} \\ & \times \frac{(-1)^{(r+i)}(r+1)!(2(p+q+2-i-w))!4^{(r+w)}F^{(i+k)}G^w M_1^i M_2^{(p+q-i-w)}}{(r-i)!(p+q+1-i-r-w)!(2r+2)!(p+q+2-i-w)!4^{(p+q+1)}(k)!(i-k)!(w)!} \\ & \times \left(M_1(p+q+1-i-r-w)\delta_{k,l} - M_2(r-i)\delta_{k,(l-1)}\right) \\ & F \equiv \frac{M_1^2+M_2^2}{M_1 M_2}, \qquad G \equiv \frac{M_1-M_2}{M_2} \end{aligned} \tag{2.91}$$

$$\begin{aligned} A_{pqr\ell} = & \sum_{i=(l-1)}^{\min[p,q,r,(p+q+1-r)]} \frac{8^i (p+q-2i)!}{(p-i)!(q-i)!(\ell)!(i+1-l)!(r-i)!} \\ & \times \frac{(-1)^{(l+r+i)}(r+1)!(2(p+q+2-i))!4^r}{(p+q+1-i-r)!(2r+2)!(p+q+2-i)!4^{(p+q+1)}} \\ & \times [(i+1-l)(p+q+1-i-r)-\ell(r-i)] \end{aligned} \tag{2.92}$$

These three factors will later be collectively referred to as the "A_{pqrl} factors".

2.3.7 Summary

Though the derivation outlined above is quite lengthy, notice that the implementation of the final result is almost trivial once one understands the significance of each variable. With explicit expressions for the $A_{pqr\ell}$, $A'_{pqr\ell}$ and $A'''_{pqr\ell}$, the evaluation of the linear combinations in Equation (2.89) for a given (p,q) is straight forward. Once these are evaluated, the corresponding a_{pq} matrix element in the linear set of equations (2.82) have been determined. To compute the diffusion coefficients at a given order of approximation N, all the a_{pq}, $(p,q) \in (-N,N) \times (-NN)$, matrix elements must be computed such that the matrix equation (2.82) can be solved to obtain the d_{-1}, d_0 and d_1.

3 Derivations

In order to implement the Kempers-model some relationships must be derived. The Enskog solutions supply a model for the thermal diffusion ratio (k_T), interdiffusion coefficient (D_{12}) and thermal diffusion coefficient (D_T), all related to the average particle velocities in the fixed FoR, or "laboratory" FoR. The Kempers-model requires the thermal diffusion factor in the ideal gas state (α_T^{ig}), related to the mole fraction- and temperature gradients. The goal of these derivations is to find a relationship between α_T, k_T and S_T, and to determine whether this relationship depends on the FoR.

First, a general relationship between the diffusive fluxes in different reference frames is derived. Then, this relationship is utilised to find a relationship between the various coefficients used to describe thermal diffusion.

3.1 Frames of reference

The magnitude of a diffusive flux is not an absolute quantity, but dependent on what frame of reference (FoR) is chosen. The FoR dictates which macroscopic property that defines the bulk velocity. That is, in the volume centre frame of reference, the bulk velocity is the velocity with which a systems centre of volume moves. Equivalently one can use mass, mole numbers, enthalpy or any other extensive variable as the frame of reference.

A diffusive flux is also characterised by a basis, the most common are mass and molar but in principle any extensive variable can be used as a basis. The basis simply defines how one measures the amount of a species. In the following discussion, all diffusive fluxes will be denoted as $\mathbf{J}_i^{AB}$, where i is the diffusing component, A is the property used as the basis, and B is the property used as the frame of reference. The corresponding partial molar properties of the components and total molar properties of the mixture will be denoted a_i, b_i and a, b respectively.

To begin the discussion, the bulk velocity in the fixed FoR, $\mathbf{u}^B$ must be defined. Here the B in $\mathbf{u}^B$ indicates which property is used to define the bulk velocity, so $\mathbf{u}^m$ is the barycentric velocity, $\mathbf{u}^n$ is the molar average velocity and so on. That is, for a system divided by a control surface moving at the bulk velocity $\mathbf{u}^B$, there is by definition always the same amount of B on both sides of the surface. This implies that, given no sources or sinks for B, the flux of B through any control surface moving at the bulk velocity must be zero. Further, in the absence of a temperature or pressure gradient,

$$dB = \sum_i b_i dn_i = 0, \qquad b_i = \left(\frac{\partial B}{\partial n_i}\right)_{T,p,n_{j\neq i}} \tag{3.1}$$

must hold for both sides of the control surface. If the mean velocity of particles of species i at the surface in the fixed FoR is $\bar{\mathbf{u}}_i$ and the molar density of species i at the surface is ρ_i, it follows that for each side of the surface,

$$\begin{aligned} \frac{dB}{dt} &= \sum_i b_i \frac{dn_i}{dt} = 0 \\ \sum_i b_i \rho_i (\bar{\mathbf{u}}_i - \mathbf{u}^B)\hat{\mathbf{n}}_{CS} &= 0 \\ \mathbf{u}^B \sum_i b_i \rho_i &= \sum_i b_i \rho_i \bar{\mathbf{u}}_i \\ \mathbf{u}^B &= \frac{1}{b}\sum_i b_i x_i \bar{\mathbf{u}}_i \end{aligned} \tag{3.2}$$

where $b = \sum_i b_i x_i$ is the molar B of the mixture and $\hat{\mathbf{n}}_{CS}$ is the unit vector perpendicular to the control surface. Letting the diffusive flux of species i now be defined as the flux through this surface, this flux can be related to the mean velocity of each particle species, and the chosen basis

$$\begin{aligned}
\mathbf{J}_i^{AB} &\equiv a_i \rho_i (\bar{\mathbf{u}}_i - \mathbf{u}^B) \\
&= a_i \rho_i \left(\bar{\mathbf{u}}_i - \frac{1}{b} \sum_j b_j x_j \bar{\mathbf{u}}_j \right) \\
&= a_i \rho_i \left(\bar{\mathbf{u}}_i \left(1 - \frac{b - \sum_{k \neq i} b_k x_k}{b} \right) - \frac{1}{b} \sum_{j \neq i} b_j c_j \bar{\mathbf{u}}_j \right) \\
&= a_i \rho_i \left(\bar{\mathbf{u}}_i \frac{1}{b} \sum_{k \neq i} x_k b_k - \frac{1}{b} \sum_{j \neq i} x_j b_j \bar{\mathbf{u}}_j \right) \\
&= \frac{a_i \rho_i}{b} \sum_{j \neq i} x_j b_j \left(\bar{\mathbf{u}}_i - \bar{\mathbf{u}}_j \right)
\end{aligned} \tag{3.3}$$

in the simple case of a binary system this simplifies to

$$\mathbf{J}_1^{AB} = \rho a_1 x_1 x_2 \frac{b_2}{b} (\bar{\mathbf{u}}_1 - \bar{\mathbf{u}}_2). \tag{3.4}$$

It is also easy to confirm in the general case that the expression fulfills the initial requirement of no net flux of B across the control surface,

$$\begin{aligned}
\sum_i \mathbf{J}_i^{AB} \frac{b_i}{a_i} &= \frac{\rho}{b} \sum_i x_i b_i \sum_{j \neq i} x_j b_j (\bar{\mathbf{u}}_i - \bar{\mathbf{u}}_j) \\
&= \frac{\rho}{b} \sum_i x_i b_i \left(\bar{\mathbf{u}}_i \sum_{j \neq i} x_j b_j - \sum_{j \neq i} x_j b_j \bar{\mathbf{u}}_j \right) \\
&= \frac{\rho}{b} \sum_i x_i b_i \left(\bar{\mathbf{u}}_i \left(b - x_i b_i \right) - \left(\mathbf{u}^B b - b_i x_i \bar{\mathbf{u}}_i \right) \right) \\
&= \frac{\rho}{b} \left(b \underbrace{\sum_i x_i b_i \bar{\mathbf{u}}_i}_{= b \mathbf{u}^B} - \mathbf{u}^B b \underbrace{\sum_i x_i b_i}_{= b} \right) = 0.
\end{aligned} \tag{3.5}$$

3.1.1 Translating between frames of reference

To translate between frames of reference B and B', The fluxes $\mathbf{J}_i^{AB}$ must be related to the $\mathbf{J}_i^{AB'}$. Beginning from the first line of equation (3.3)

$$\begin{aligned}
\mathbf{J}_i^{AB} &= a_i \rho_i (\bar{\mathbf{u}}_i - \mathbf{u}^B) \\
&= a_i \rho_i (\bar{\mathbf{u}}_i - \mathbf{u}^B + (\mathbf{u}^{B'} - \mathbf{u}^{B'})) \\
&= a_i \rho_i (\bar{\mathbf{u}}_i - \mathbf{u}^{B'}) + a_i \rho_i (\mathbf{u}^{B'} - \mathbf{u}^B).
\end{aligned} \tag{3.6}$$

Identifying the first term as $\mathbf{J}_i^{AB'}$ and inserting for the definition of the bulk velocities gives

$$\begin{aligned}\mathbf{J}_i^{AB} &= \mathbf{J}_i^{AB'} + a_i\rho_i \sum_j \left(\frac{x_j b'_j}{b'} - \frac{x_j b_j}{b}\right) \bar{\mathbf{u}}_j \\ &= \mathbf{J}_i^{AB'} + a_i\rho_i \sum_j \left(\frac{x_j b'_j}{b'} - \frac{x_j b_j}{b}\right) \left(\frac{\mathbf{J}_j^{AB'}}{a_j c_j} + \mathbf{u}^{B'}\right)\end{aligned} \tag{3.7}$$

where the definition of the diffusive flux on the first line of equation (3.3) has been inserted for the average particle velocity to get the final equality. Now, note that

$$a_i\rho_i \mathbf{u}^{B'} \sum_j \left(\frac{x_j b'_j}{b'} - \frac{x_j b_j}{b}\right) = 0 \tag{3.8}$$

because $b = \sum_j x_j b_j$. Further, because only $N-1$ of the N fluxes are independent due to the constraint of Equation (3.5), one flux $\mathbf{J}_k^{AB'}$ can be expressed as a linear combination of the other fluxes

$$\begin{aligned}\sum_j \frac{b'_j}{a_j} \mathbf{J}_j^{AB'} &= 0 \\ \mathbf{J}_k^{AB'} &= -\frac{a_k}{b'_k} \sum_{j\neq k} \frac{b'_j}{a_j} \mathbf{J}_j^{AB'}.\end{aligned} \tag{3.9}$$

Extracting $\mathbf{J}_k^{AB'}$ from the sum in (3.7) and inserting for Equation (3.9) yields

$$\mathbf{J}_i^{AB} = \mathbf{J}_i^{AB'} + \frac{a_i\rho_i}{a_k c_k}\left(\frac{x_k b'_k}{b'} - \frac{x_k b_k}{b}\right)\left(-\frac{a_k}{b'_k}\sum_{j\neq k}\frac{b'_j}{a_j}\mathbf{J}_j^{AB'}\right) + a_i\rho_i \sum_{j\neq k}\left(\frac{x_j b'_j}{b'} - \frac{x_j b_j}{b}\right)\frac{\mathbf{J}_j^{AB'}}{a_j c_j}. \tag{3.10}$$

Noting that $\rho_i \frac{x_j}{c_j} = x_i$ and combining the sums yields

$$\begin{aligned}\mathbf{J}_i^{AB} &= \mathbf{J}_i^{AB'} - a_i x_i \sum_{j\neq k}\left[\left(\frac{b'_j}{b'} - \frac{b'_j b_k}{b b'_k}\right) - \left(\frac{b'_j}{b'} - \frac{b_j}{b}\right)\right]\frac{\mathbf{J}_j^{AB'}}{a_j} \\ &= \mathbf{J}_i^{AB'} - a_i x_i \sum_{j\neq k}\left(\frac{b_j}{b} - \frac{b'_j b_k}{b b'_k}\right)\frac{\mathbf{J}_j^{AB'}}{a_j} \\ &= \sum_j \psi_{ijk}^{BB'} \mathbf{J}_j^{AB'}\end{aligned} \tag{3.11}$$

where the final equality defines

$$\psi_{ijk}^{BB'} \equiv \delta_{ij} - \frac{a_i x_i}{a_j}\left(\frac{b_j}{b} - \frac{b'_j b_k}{b b'_k}\right). \tag{3.12}$$

Checking the specific cases Ψ_{ijN}^{nV}, Ψ_{ijN}^{nm} and Ψ_{ijN}^{mn}, shown in Table 3.1, in the molar basis ($a_i = a_j = 1$) yields the same expressions as those given by Krishna and Taylor.[32] Showing that the fluxes in reference frame B are independent of the chosen component k, that is

$$\sum_j \psi_{ijk}^{BB'} \mathbf{J}_j^{AB'} = \sum_j \psi_{ijl}^{BB'} \mathbf{J}_j^{AB'}, \qquad \forall \qquad k, l \tag{3.13}$$

is simply done by recognising the fluxes $\mathbf{J}_k^{AB'}$ and $\mathbf{J}_l^{AB'}$ from equation (3.9),

$$\begin{aligned}
\sum_j \psi_{ijk}^{BB'} \mathbf{J}_j^{AB'} &= \sum_j \psi_{ijl}^{BB'} \mathbf{J}_j^{AB'} \\
\mathbf{J}_i^{AB'} - a_i x_i \sum_{j \neq k} \left(\frac{b_j}{b} - \frac{b'_j b_k}{b b'_k} \right) \frac{\mathbf{J}_j^{AB'}}{a_j} &= \mathbf{J}_i^{AB'} - a_i x_i \sum_{j \neq l} \left(\frac{b_j}{b} - \frac{b'_j b_l}{b b'_l} \right) \frac{\mathbf{J}_j^{AB'}}{a_j} \\
\sum_{j \neq k} \frac{b_j}{a_j} \mathbf{J}_j^{AB'} - \frac{b_k}{b'_k} \sum_{j \neq k} \frac{b'_j}{a_j} \mathbf{J}_j^{AB'} &= \sum_{j \neq l} \frac{b_j}{a_j} \mathbf{J}_j^{AB'} - \frac{b_l}{b'_l} \sum_{j \neq l} \frac{b'_j}{a_j} \mathbf{J}_j^{AB'} \\
\sum_{j \neq k} \frac{b_j}{a_j} \mathbf{J}_j^{AB'} + \frac{b_k}{a_k} \mathbf{J}_k^{AB'} &= \sum_{j \neq l} \frac{b_j}{a_j} \mathbf{J}_j^{AB'} + \frac{b_l}{a_l} \mathbf{J}_l^{AB'}.
\end{aligned} \tag{3.14}$$

Because the choice of component k is arbitrary one can denote $\psi_{ij}^{BB'} \mapsto \psi_{ijk}^{BB'}$, dropping k from the subscript. Equation (3.11) can also be written in matrix form as

$$\mathbf{J}^{AB} = \underline{\mathbf{\Psi}}^{BB'} \mathbf{J}^{AB'}. \tag{3.15}$$

The matrix elements $\psi_{ij}^{BB'}$ for transformations between the mass- molar- and volume centre frame of reference are summarised in Table 3.1. Note that the form of the transformations changes with basis. Using a molar basis for the flux gives $a_i = a_j = 1$, while if one uses a mass basis, a_i and a_j become the molar masses.

Table 3.1: Some specific forms of $\psi_{ij}^{BB'}$. Note that starting from the general form, one can easily arrive at different formulations for $\psi_{ij}^{BB'}$, this process can also give some additional insight into how the fluxes change from one FoR to another. $\phi_i = \frac{v_i n_i}{V}$ denotes the volume fraction of species i.

		Transform from FoR		
		m	n	V
To FoR	m		$\delta_{ij} - \frac{a_i x_i}{a_j} \left(\frac{w_j}{x_j} - \frac{w_k}{x_k} \right)$	$\delta_{ij} - \frac{a_i x_i}{a_j} \left(\frac{w_j}{x_j} - \frac{w_k \phi_j}{\phi_k x_j} \right)$
	n	$\delta_{ij} - \frac{a_i x_i}{a_j} \left(1 - \frac{w_j x_k}{x_j w_k} \right)$		$\delta_{ij} - \frac{a_i x_i}{a_j} \left(1 - \frac{\phi_j x_k}{x_j \phi_k} \right)$
	V	$\delta_{ij} - \frac{a_i x_i}{a_j} \left(\frac{\phi_j}{x_j} - \frac{w_j \phi_k}{x_j w_k} \right)$	$\delta_{ij} - \frac{a_i x_i}{a_j} \left(\frac{\phi_j}{x_j} - \frac{\phi_k}{x_k} \right)$	

3.2 Relating S_T, α_T and k_T

Various coefficients are used to describe thermal diffusion. This section aims to define and relate the Soret coefficient S_T, the thermal diffusion factor α_T and the thermal diffusion ratio k_T through the Onsager phenomenological coefficients. This is required, as the Enskog solutions provide a manner of computing the

thermal diffusion ratio, but the Kempers-models requires the thermal diffusion factor from kinetic gas theory as input. For a binary system, the coefficients are defined as

$$S_{T,i} = -\frac{\nabla x_i}{x_i(1-x_i)\nabla T}, \qquad \alpha_{T_i} = TS_{T,i}, \qquad k_T = \frac{D_{T,1}}{D_{12}} \tag{3.16}$$

Where $D_{T,1}$ and D_{12} are the thermal diffusion and interdiffusion coefficient as described in Section 2.3, indirectly defined as

$$\bar{\mathbf{u}}_1 - \bar{\mathbf{u}}_2 = -\frac{D_{T,1}}{x_1 x_2}\nabla \ln T, \qquad \nabla x = \nabla p = \mathbf{F}_1 = \mathbf{F}_2 = 0 \tag{3.17}$$

where p indicates pressure, and $\mathbf{F}_i$ indicate external forces on species i. Relating this coefficient to the flux through equation (3.4) yields

$$\left(\mathbf{J}_1^{AB}\right)_{\mathbf{d}_{12}=0} = -\rho a_1 x_1 x_2 \frac{b_2}{b}\frac{D_{T,1}}{x_1 x_2}\nabla \ln T, \qquad \mathbf{d}_{12} = \nabla x_1 + \frac{\rho_1\rho_2(m_2-m_1)}{\rho\rho_m}\nabla \ln p - \frac{\rho_{m,2}\rho_{m,2}}{\rho_m p}(\mathbf{F}_1 - \mathbf{F}_2) \tag{3.18}$$

Where m_i are the molecular masses, ρ is the molar density and ρ_m is the mass density. On a molar basis, $a_i = 1$ giving

$$\left(\mathbf{J}_1^{nB}\right)_{\mathbf{d}_{12}=0} = -\rho\frac{b_2}{b}D_{T,1}\nabla \ln T. \tag{3.19}$$

From the entropy production,

$$\mathbf{J}_1^{nm} = L_{\mu\mu}\left(-\frac{1}{T}\nabla_T \mu_1\right) + L_{\mu q}\nabla\left(\frac{1}{T}\right) \tag{3.20}$$

where ∇_T indicates that the gradient is taken at constant temperature. The fluxes $\mathbf{J}_1^{nm}$ and $\mathbf{J}_1^{nB}$ are related by equation (3.11), as

$$\mathbf{J}_1^{nB} = \mathbf{J}_1^{nm}\left(\psi_{11}^{Bm} - \psi_{12}^{Bm}\right) \equiv \mathbf{J}_1^{nm}\psi^{Bm} \tag{3.21}$$

where M_i is the molar mass of species i and the final equality defines ψ^{Bm}. The thermal diffusion coefficient can then be related to the phenomenological coefficients of equation (3.20) as

$$\begin{aligned}
\left(\mathbf{J}_1^{nm}\right)_{\nabla_T\mu=0}\psi^{Bm} &= \left(\mathbf{J}_1^{nB}\right)_{\mathbf{d}_{12}=0} \\
L_{\mu q}\nabla\left(\frac{1}{T}\right)\psi^{Bm} &= -\rho\frac{b_2}{b}D_{T,1}\nabla \ln T \\
D_{T,1} &= \frac{L_{\mu q}\psi^{Bm}b}{\rho T b_2}
\end{aligned} \tag{3.22}$$

where the first line follows from $\mathbf{d}_{12} = 0 \iff \nabla_T\mu = 0$. Following the same procedure for the interdiffusion coefficient,

$$\left(\bar{\mathbf{u}}_1 - \bar{\mathbf{u}}_2\right)_{\nabla T=0} = -D_{12}\frac{\rho^2}{\rho_1\rho_2}\nabla x_1 \tag{3.23}$$

Inserting this into equation (3.4) yields

$$\begin{aligned}\left(\mathbf{J}_1^{nB}\right)_{\nabla T=0} &= -\rho x_1 x_2 \frac{b_2}{b} D_{12} \frac{\rho^2}{\rho_1 \rho_2} \nabla x_1 \\ &= -\frac{b_2}{b} \rho D_{12} \nabla x_1.\end{aligned} \tag{3.24}$$

From Equation (3.20),

$$(\mathbf{J}_1^{nm})_{\nabla T=0} = L_{\mu\mu} \left(-\frac{\nabla_T \mu_1}{T}\right). \tag{3.25}$$

The chemical potential gradient is related to the mole fraction gradient by

$$\begin{aligned}\mu_i &= \mu_i^\circ + RT \ln \gamma_x x_i \\ \nabla \mu_{i,T} &= \frac{RT}{x_i} \left(1 + \left(\frac{\partial \ln \gamma_x}{\partial \ln x_i}\right)\right) \nabla x_i \\ \nabla \mu_{i,T} &\equiv \frac{RT}{x_i} \Gamma_1^* \nabla x_i,\end{aligned} \tag{3.26}$$

where γ_x is the mole fraction based activity coefficient, and the final equality defines Γ_1^*. The flux of species 1 can then be written as

$$(\mathbf{J}_1^{nm})_{\nabla_T=0} = -\frac{1}{T} L_{\mu\mu} \frac{RT}{x_1} \Gamma_1^* \nabla x_1 = -\frac{R L_{\mu\mu}}{x_1} \Gamma^* \nabla x_1 \tag{3.27}$$

The interdiffusion coefficient can now be related to the phenomenological coefficients by comparing equations (3.24) and (3.27), giving

$$\begin{aligned}(\mathbf{J}_1^{nm})_{\nabla_T=0}\, \psi^{Bm} &= \left(\mathbf{J}_1^{nB}\right)_{\nabla T=0} \\ -\frac{R L_{\mu\mu}}{x_1} \Gamma_1^* \psi^{Bm} \nabla x_1 &= -\frac{b_2}{b} \rho D_{12} \nabla x_1 \\ D_{12} &= \frac{R L_{\mu\mu} b}{\rho_1 b_2} \Gamma_1^* \psi^{Bm}.\end{aligned} \tag{3.28}$$

Now, to relate the Soret coefficient to the thermal diffusion ratio, regard the flux equation of component 1 in the state in which the mass flux vanishes ($\mathbf{J} = 0$),

$$\begin{aligned}\mathbf{J}_1^{nm} = L_{\mu\mu} \left(-\frac{\nabla \mu_{1,T}}{T}\right) + L_{\mu q} \nabla \left(\frac{1}{T}\right) &= 0 \\ -\frac{R L_{\mu\mu}}{\rho_1} \Gamma_1^* \nabla x_1 + L_{\mu q} \nabla \left(\frac{1}{T}\right) &= 0 \\ -\frac{\nabla x_1}{x_1 \nabla T} &= \frac{L_{\mu q}}{R T^2 L_{\mu\mu} \Gamma_1^*}.\end{aligned} \tag{3.29}$$

Inserting the expressions from Equation (3.22) and (3.28) in the definition of the thermal diffusion ratio gives

$$k_{T,1} = \frac{D_{T,1}}{D_{12}} = \frac{L_{\mu q} x_1}{RTL_{\mu\mu}\Gamma_1^*}. \tag{3.30}$$

It is noted that the dependencies of $D_{T,1}$ and D_{12} on the frame of reference B cancel, such that $k_{T,1}$ is independent of the frame of reference. Identifying the thermal diffusion ratio in equation (3.29) yields

$$\begin{aligned} -\frac{\nabla x_1}{x_1 \nabla T} = \frac{1}{x_1 T} k_{T,1} &= S_{T,1}(1 - x_1) \\ S_{T,1} &= \frac{k_{T,1}}{x_1(1-x_1)T}. \end{aligned} \tag{3.31}$$

Apart from conveniently relating the coefficients, $k_{T,1}$ and $S_{T,1}$ (and thereby $\alpha_{T,1}$), this derivation also shows that the relation between the three coefficients is independent of the FoR, as all factors relating to the FoR have cancelled.

3.2.1 Expanding to the multicomponent case

The working implementation of the Enskog solutions used in this work is restricted to binary systems, using the Equations presented in Section (2.3), therefore no time will be spent elaborating on the derivation of the multicomponent Enskog solutions. However, to facilitate the future possibility of coupling a multicomponent implementation of the Enskog solutions to the working implementation of the Kempers-model, the relation between $S_{T,i}$ and $k_{T,i}$ in a multicomponent mixture is derived here. For a detailed derivation of the relations used as a starting point here, the reader is referred to Chapman and Cowling. [11]

In the case of multicomponent mixtures, the Enskog solutions yield an expression relating particle velocities to the compositional- and thermal gradients

$$\bar{\mathbf{u}}_i - \mathbf{u}^n = -\sum_j \Delta_{ij} \nabla x_j - D_{T,i} \nabla \ln T \tag{3.32}$$

where Δ_{ij} are $\frac{1}{2}\left(N^2 - N\right)$ independent, generalised diffusion coefficients. These are constrained by the symmetry relation $\Delta_{ij} = \Delta_{ji}$ and the condition $\sum_j \rho_j \Delta_{ij} = 0$. The thermal diffusion coefficients $D_{T,i}$ are not independent either, being constrained by an analogous relation, $\sum_i m_i \rho_i D_{T,i} = 0$. The multicomponent thermal diffusion ratio is then identified by rewriting equation (3.32) in a manner analogous to the binary case,

$$\bar{\mathbf{u}}_i - \mathbf{u}^n = -\sum_j \Delta_{ij} \left(\nabla x_j + k_{T,j} \nabla \ln T\right). \tag{3.33}$$

Where $k_{T,j}$ is now defined by $D_{T,i} \equiv \sum_j \Delta_{ij} k_{T,j}$ and $\sum_j k_{T,j} = 0$. The latter equation is necessary because only $N - 1$ of the $D_{T,j}$ are independent. Equation (3.32) may be rewritten to matrix form, as

$$\tilde{\mathbf{u}} = \underline{\boldsymbol{\Delta}} \left(\nabla \mathbf{x} - \mathbf{k}_T \nabla \ln T\right), \qquad \tilde{\mathbf{u}} = \begin{pmatrix} \bar{\mathbf{u}}_1 - \mathbf{u}^n \\ \bar{\mathbf{u}}_2 - \mathbf{u}^n \\ \vdots \\ \bar{\mathbf{u}}_n - \mathbf{u}^n \end{pmatrix}. \tag{3.34}$$

The goal now is to find a manner in which to relate the vector $\mathbf{k}_T$ to the gradients in composition and temperature, such that it can be related to the Soret-coefficients. Note that the matrix $\underline{\boldsymbol{\Delta}}$ is singular due to

the summational constraint on the Δ_{ij}. Solve this problem by explicitly including the constraint that the thermal diffusion ratios and the mole fraction gradients must sum to zero. That is, define

$$\underline{\boldsymbol{\Delta}}' = \begin{bmatrix} 0 & 1 & 1 & \dots & 1 \\ 1 & \Delta_{11} & \Delta_{12} & \dots & \Delta_{1N} \\ 1 & \Delta_{21} & \Delta_{22} & \dots & \Delta_{2N} \\ \vdots & \vdots & \vdots & \ddots & \vdots \\ 1 & \Delta_{N1} & \Delta_{N2} & \dots & \Delta_{NN} \end{bmatrix} \quad \tilde{\mathbf{u}}' = \begin{pmatrix} 0 \\ \bar{\mathbf{u}}_1 - \mathbf{u}^n \\ \bar{\mathbf{u}}_2 - \mathbf{u}^n \\ \vdots \\ \bar{\mathbf{u}}_N - \mathbf{u}^n \end{pmatrix} \quad \mathbf{x}' = \begin{pmatrix} 0 \\ x_1 \\ x_2 \\ \vdots \\ x_N \end{pmatrix} \tag{3.35}$$

such that

$$\tilde{\mathbf{u}}' = \underline{\boldsymbol{\Delta}}' \left(\nabla \mathbf{x}' - \mathbf{k}_T' \nabla \ln T \right). \tag{3.36}$$

The matrix $\underline{\boldsymbol{\Delta}}'$ can now be identified as invertible by multiplying with the matrix

$$\underline{\boldsymbol{\rho}} = \begin{bmatrix} 0 & -\rho_1 & -\rho_2 & \dots & -\rho_N \\ \rho_1 & 0 & \rho_1 & \dots & \rho_1 \\ \rho_2 & \rho_2 & 0 & & \vdots \\ \rho_3 & \rho_3 & \rho_3 & \ddots & \\ & \vdots & & & \rho_{N-1} \\ \rho_N & \rho_N & \dots & \rho_N & 0 \end{bmatrix}. \tag{3.37}$$

This product can quickly be seen to be invertible, and

$$\det\left(\underline{\boldsymbol{\Delta}}'\underline{\boldsymbol{\rho}}\right) \neq 0 \iff \det\left(\underline{\boldsymbol{\Delta}}'\right) \neq 0 \wedge \det\left(\underline{\boldsymbol{\rho}}\right) \neq 0 \tag{3.38}$$

such that $\underline{\boldsymbol{\Delta}}'$ must be invertible. With this established, it is safe to rewrite Equation (3.36) to the form

$$\left(\underline{\boldsymbol{\Delta}}'\right)^{-1} \tilde{\mathbf{u}}' = \left(\nabla \mathbf{x}' - \mathbf{k}_T' \nabla \ln T \right). \tag{3.39}$$

At steady state, $\tilde{\mathbf{u}}' = 0$, such that this set of equations reads

$$\begin{aligned} \nabla x_i + k_{T,i} \nabla \ln T &= 0 \\ k_{T,i} &= -\frac{T \nabla x_i}{\nabla T} \\ S_{T,i} &= \frac{k_{T,i}}{T x_i (1 - x_i)}. \end{aligned} \tag{3.40}$$

Where the final equality follows from the definition of the Soret coefficient. This expression is clearly equivalent to the expression in Equation (3.31) in the case of a binary mixture, as expected.

A note on the diffusion coefficient

It should be noted that the generalized diffusion coefficients Δ_{ij} do not reduce to the binary diffusion coefficient in the binary case. If one instead of regarding the matrix $\underline{\boldsymbol{\Delta}}$, regards $\left(\underline{\boldsymbol{\Delta}}'\right)^{-1}$ in Equation (3.39), coefficients more closely related to the Fickean diffusion coefficients can be obtained. Chapman and Cowling identify the elements of this matrix as

$$\frac{\mathrm{Co}(\Delta_{ij})}{\det\left(\underline{\boldsymbol{\Delta}}'\right)} \equiv \frac{x_i x_j}{D_{ij}} \tag{3.41}$$

by Cramers' rule.[11] Here, $\mathrm{Co}(\Delta_{ij})$ denotes the cofactor of the element Δ_{ij} in the matrix $\underline{\boldsymbol{\Delta}}'$. Equation (3.39) can then be written as

$$\begin{aligned} -\sum_j \frac{x_i x_j}{D_{ij}} \left(\mathbf{u}_j - \mathbf{u}^n \right) &= \nabla x_i + k_{T,i} \nabla \ln T \\ \sum_i \frac{x_i}{D_{ij}} &= 0. \end{aligned} \tag{3.42}$$

It is a simple exercise to show that this reduces to the binary diffusion coefficient D_{12} as defined in Equation (3.23) for a binary mixture.

3.2.2 Alternative definitions

The relationships presented here are obviously a result of how the various coefficients are defined. It deserves mention that various authors have defined them in different ways. For example the thermal diffusion coefficient has been defined by Zárate through, [33]

$$(\mathbf{J}_1^{nn})_{\nabla x=0} = \rho x_1(1-x_1)D'_T\nabla T. \tag{3.43}$$

It is stated that the advantage of this definition of D'_T is that it becomes independent of the FoR, so using the same coefficient one can express the flux of component 1 as

$$(\mathbf{J}_1^{nm})_{\nabla w=0} = \rho w_1(1-w_1)D'_T\nabla T. \tag{3.44}$$

If the Soret coefficient is defined in the same manner as in equation (3.16), the relation to the thermal diffusion coefficient and the Fick diffusion coefficient D (which is different from the Maxwell-Stefan diffusion coefficient in equation (3.23)) is then

$$S_T = \frac{D'_T}{D} = Tk'_T, \qquad k'_T = \frac{D'_T}{D}. \tag{3.45}$$

Zárate continues by proposing a definition of the Soret coefficient for multicomponent systems that keeps the Soret coefficient independent of the FoR, defining it through the equation

$$\begin{pmatrix} S'_{T,1} \\ S'_{T,2} \end{pmatrix} = \begin{bmatrix} x_1(1-x_1) & -x_1x_2 \\ -x_2x_1 & x_2(1-x_2) \end{bmatrix}^{-1} \frac{\nabla \mathbf{x}}{\nabla T}, \qquad \mathbf{x} = \begin{pmatrix} x_1 \\ x_2 \end{pmatrix}. \tag{3.46}$$

Zárate states that the advantage of this definition is that it is consistent with the chosen definition of D'_T, and that it removes the need to regard the frame of reference when conducting experiments or simulations. However, following his procedure for showing that the definition is independent of the FoR reveals that it only holds when translating between the CoM- and molar centre FoR. Because the Kempers-model deals with the CoV FoR, this manner of defining the Soret coefficient is not pursued further in this work.

4 Methods

4.1 Equations of State

All equations of state used in this work are implemented in the open-source thermodynamic library ThermoPack.[26] This includes a database of parameters for the various equations of state. The parameters used are those listed as the default parameters for each fluid, except in the case of the computations in Section 5.3 and 5.4. In those sections, the parameters reported by Reith and Müller-Plathe are used such that the results obtained here will be comparable to those they have reported.[8]

4.2 The Enskog solutions

As indicated in Section 2.3.7, implementation of the Enskog solutions using the explicit summational expressions obtained by Tompson et al. is straight forward. A practical issue of note is that the factorial operations in the sums defining the A_{pqrl} factors tend to cause overflow issues already at quite low orders of approximation. Already at order $N = 5$, the factorial 24! must be evaluated, which is too large for a 64-bit unsigned integer. To remedy this, it was noted that although there are very large numbers involved in the evaluation of the A_{pqrl}-factors, they largely cancel in the fractions. Therefore, a "smart" evaluation of factorials and fractions was implemented. The implementation defines data types for factorials, products and fractions with the multiplication and division operator defined such that fractions containing products of integers and factorials can be exactly represented. This is done by treating a product as a list of integers, and a fraction as two products; the numerator and the denominator. If a product is multiplied by a non-integer type, the non-integer part of the product is stored separately. The actual evaluation of the products is not done until explicitly required. Upon evaluation of the fractions, common integers in the numerator and denominator are cancelled, then the simplified numerator and denominator are evaluated and the results divided by each other, much like one would do the computation manually. This was tested up to approximation order $N = 25$ and prevented overflow up to that order.

Another practical question of interest is what potential and parameters one should use for the collision integrals. In this work, the hard-sphere collision integrals were implemented, using two different approaches to obtain the hard-sphere diameters. The first approach simply uses Mie-potential σ-parameters. The argument for this is that the Mie-potential rises very steeply, behaving almost like a hard sphere potential, at $r < \sigma$. Therefore, σ should be a reasonable first approximation to the shortest possible distance between the centre of mass of two particles. The second approach employs the Barker-Henderson (BH) diameter (d_{BH}) defined as

$$d_{BH} = \int_0^\sigma 1 - \exp\left(-\frac{u^{Mie}(r)}{k_B T}\right) dr \tag{4.1}$$

where u^{Mie} is the Mie potential,

$$u^{Mie}(r) = C\varepsilon\left[\left(\frac{\sigma}{r}\right)^{\lambda_r} - \left(\frac{\sigma}{r}\right)^{\lambda_a}\right], \qquad C = \frac{\lambda_r}{\lambda_r - \lambda_a}\left(\frac{\lambda_r}{\lambda_a}\right)^{\frac{\lambda_a}{\lambda_r - \lambda_a}}. \tag{4.2}$$

Here, λ_r and λ_a are the repulsive and attractive exponents. The specific case $\lambda_r = 12$, $\lambda_a = 6$ is the commonly known Lennard-Jones (LJ) potential or the LJ (12-6) potential.

The BH-diameter is very close to the σ-parameter at low temperatures but decreases with increasing temperature, as shown in Figure 4.1. This simulates the fact that particles moving at a higher velocity (higher temperature) will come closer together before deflecting. In a sense, this can be thought of as a rough manner of approximating the effect one would see if the collision integrals were implemented using a purely repulsive potential similar to the repulsive part of the Mie-potential. The difference in these two approaches is investigated in Section 5.2, and discussed further in Section 6.

Finally, the convergence of the Enskog solutions with increasing order of approximation was investigated. As shown in Figure 4.2, the coefficients d_{-1}, d_0 and d_1 converge already at the fourth or fifth order approximation. A fifth order approximation was used to generate the results presented in Sections 5.3, 5.4 and

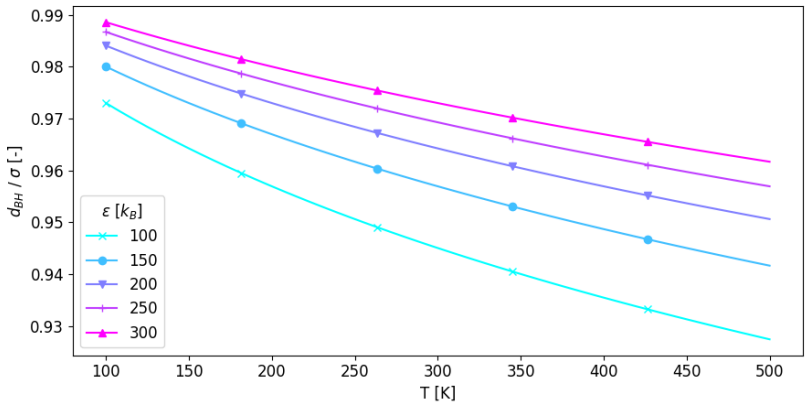

Figure 4.1: Ratio of the BH-diameter to the σ-parameter of the Lennard-Jones 12-6 potential as a function of temperature, for different ε-values. The ratio is not a function of the σ-parameter, as can be shown by differentiating Equation (4.1).

5.5. In the making of this report it was recognised that the thermal diffusion ratio predicted at higher order approximations ($N > 7$) was divergent under certain conditions. This is investigated and discussed in closer detail in Section 5.6.

The final implementation of the Enskog solutions used in this work can be found in a public repository on GitHub. [34]

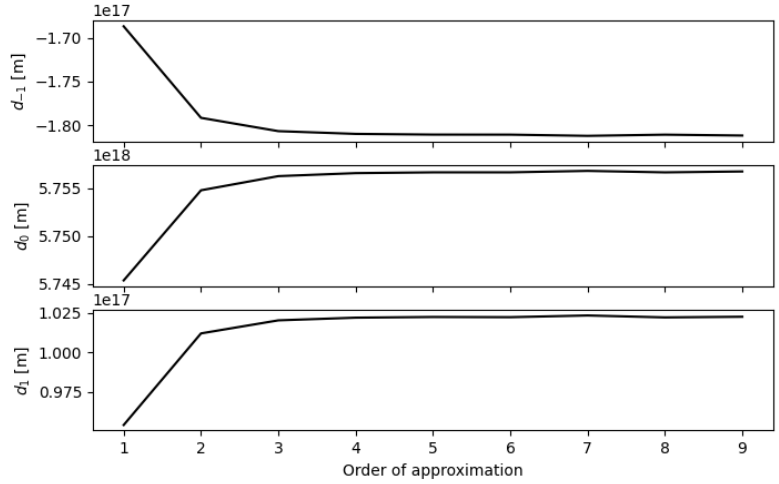

Figure 4.2: Convergence of the computed d_{-1}, d_0 and d_1 with increasing order of approximation. Using $m_1 = 15\,\mathrm{g\,mol^{-1}}$, $m_2 = 10\,\mathrm{g\,mol^{-1}}$, $\sigma_1 = 1.5$ Å, $\sigma_2 = 2$ Å and $\sigma_{12} = 1.75$ Å, with a hard-sphere potential for the collision integrals.

4.2.1 Numerical error

In the study of the higher order Enskog solutions, the effect and magnitude of the numerical error introduced in the solution of Equation (2.81), which yields the expansion coefficients d_{-1}, d_0 and d_1, was investigated.

To do this, a meaningful manner in which to measure the error in the matrix inversion must be identified. For convenience of notation, Equation (2.81) may be written as

$$\underline{\boldsymbol{D}}_N \left[\mathbf{d}\right]_N = \boldsymbol{\delta}, \tag{4.3}$$

where $\left[\mathbf{d}\right]_N$, is the exact Nth approximation to the vector of Sonine polynomial expansion coefficients, devoid of numerical error and $\underline{\boldsymbol{D}}_N$ is the matrix containing some truncation error from the evaluation of the a_{pq} elements. $\boldsymbol{\delta}$ is the vector of all zeros, except the central element δ_0, which is a float value with inherent truncation error. The numerical solution to Equation (4.3) is denoted $[\tilde{\mathbf{d}}]_N$. A simple manner of investigating the expected error introduced when inverting $\underline{\boldsymbol{D}}_N$ is computing the condition number, $\kappa(\underline{\boldsymbol{D}}_N)$. This number gives an indication of how much a change in $\underline{\boldsymbol{D}}_N$ or $\boldsymbol{\delta}$ will effect the solution to the equation, i.e. how sensitive it is to float truncation error. A large condition number indicates an ill-conditioned problem, with high potential error. The remainder of this section presents an alternative measure for the deviation of the numerical solution from the true solution.

Assuming that the numerical error introduced in the evaluation of the a_{pq} matrix elements is negligible, all error in $[\tilde{\mathbf{d}}]_N$ stems from the matrix inversion. This is likely a reasonable assumption, because the implemented "smart" evaluation of the A_{pqrl} factors simplifies all fractions in Equations (2.90) to (2.92) by an exact method before evaluation. This reduces the absolute value of the numerator and denominator such that float truncation error becomes less significant. Now, upon numerically inverting the matrix $\underline{\boldsymbol{D}}_N$, assume that some error ϵ is introduced, such that

$$\begin{aligned} \left[\mathbf{d}\right]_N &= [\tilde{\mathbf{d}}]_N + \boldsymbol{\epsilon} \\ &= \underline{\boldsymbol{D}}_N^{-1}\boldsymbol{\delta} + \boldsymbol{\epsilon}. \end{aligned} \tag{4.4}$$

Further, because Equation (4.3) is assumed to hold exactly, left-multiplication by $\underline{\boldsymbol{D}}_N$ yields

$$\begin{aligned} \boldsymbol{\delta} &= \underline{\boldsymbol{D}}_N\underline{\boldsymbol{D}}_N^{-1}\boldsymbol{\delta} + \underline{\boldsymbol{D}}_N\boldsymbol{\epsilon} \\ \underline{\boldsymbol{D}}_N\boldsymbol{\epsilon} &= \left(\underline{\boldsymbol{I}} - \underline{\boldsymbol{D}}_N\underline{\boldsymbol{D}}_N^{-1}\right)\boldsymbol{\delta} \end{aligned} \tag{4.5}$$

where $\underline{\boldsymbol{I}}$ is the identity matrix. This obviously holds, as the factor in the parentheses on the right hand side is identically zero if there is no error in the matrix inversion. Left-multiplying by $\underline{\boldsymbol{D}}_N^{-1}$ gives

$$\boldsymbol{\epsilon} = \underline{\boldsymbol{D}}_N^{-1}\left(\underline{\boldsymbol{I}} - \underline{\boldsymbol{D}}_N\underline{\boldsymbol{D}}_N^{-1}\right)\boldsymbol{\delta} + \boldsymbol{\epsilon}' \tag{4.6}$$

Neglecting the error introduced in this operation, $\boldsymbol{\epsilon}'$, then gives

$$\boldsymbol{\epsilon} \approx \underline{\boldsymbol{D}}_N^{-1}\left(\underline{\boldsymbol{I}} - \underline{\boldsymbol{D}}_N\underline{\boldsymbol{D}}_N^{-1}\right)\boldsymbol{\delta}. \tag{4.7}$$

Finally, because it is the error in the three components d_{-1}, d_0 and d_1 that is of interest, and the value of $\left[\mathbf{d}\right]_N$ is a function of particle masses, HS-diameters and composition, define the relative error

$$\epsilon_N^r \equiv \left|\frac{\epsilon_{-1}}{[d_{-1}]_N}\right| + \left|\frac{\epsilon_0}{[d_0]_N}\right| + \left|\frac{\epsilon_1}{[d_1]_N}\right|. \tag{4.8}$$

When interpreting the value of ϵ_N^r, note that floating point precision in the computations in this work is 10^{-16}, so a relative error on the order of $10^{-16} - 10^{-14}$ indicates that no error beyond that inherent to floating point arithmetic has been introduced in the matrix inversion.

4.3 The Kempers-model

All quantities required for the implementation of the model developed by Kempers, with the exception of $\left(\frac{\partial \mu_i}{\partial x_j}\right)_{T,p}$, are readily available through ThermoPack.[26] This section relates the quantity $\left(\frac{\partial \mu_i}{\partial x_j}\right)_{T,p}$ to other properties that are available.

Begin from the definition of the chemical potential as the derivative of Helmholtz energy and invert the order of differentiation,

$$\left(\frac{\partial \mu_i}{\partial n_j}\right)_{T,p} = \left(\frac{\partial}{\partial n_j}\left(\frac{\partial A}{\partial n_i}\right)_{T,V}\right)_{T,p} = \left(\frac{\partial}{\partial n_i}\left(\frac{\partial A}{\partial n_j}\right)_{T,p}\right)_{T,V}. \tag{4.9}$$

From the total differential of the Helmholtz energy, $dA = -SdT - pdV + \sum_i \mu_i dn_i$,

$$\begin{aligned}
\left(\frac{\partial A}{\partial n_j}\right)_{T,p} &= -p\left(\frac{\partial V}{\partial n_j}\right)_{T,p} + \mu_j \\
\left(\frac{\partial}{\partial n_i}\left(\frac{\partial A}{\partial n_j}\right)_{T,p}\right)_{T,V} &= \left(\frac{\partial \mu_j}{\partial n_i}\right)_{T,V} - v_j\left(\frac{\partial p}{\partial n_i}\right)_{T,V} - p\underbrace{\left(\frac{\partial v_j}{\partial n_i}\right)_{T,V}}_{=0} \\
\left(\frac{\partial \mu_i}{\partial n_j}\right)_{T,p} &= \left(\frac{\partial \mu_j}{\partial n_i}\right)_{T,V} - v_j\left(\frac{\partial p}{\partial n_i}\right)_{T,V}.
\end{aligned} \tag{4.10}$$

The total differential of the chemical potential at constant pressure and temperature is

$$d\mu_i = \sum_j \left(\frac{\partial \mu_i}{\partial n_j}\right)_{T,p,n_{k\neq j}} dn_j. \tag{4.11}$$

Further inserting for the total differential of the mole number of each species yields

$$\begin{aligned}
d\mu_i &= \sum_j \left(\frac{\partial \mu_i}{\partial n_j}\right)_{T,p,n_{k\neq j}} (x_j dn + n dx_j) \\
d\mu_i &= \sum_j \left(\frac{\partial \mu_i}{\partial n_j}\right)_{T,p,n_{k\neq j}} n dx_j + \left(\underbrace{\sum_j \left(\frac{\partial \mu_i}{\partial n_j}\right)_{T,p,n_{k\neq j}} x_j}_{=0}\right) dn \\
&= \sum_j \left(\frac{\partial \mu_i}{\partial x_j}\right)_{T,p,n_{k\neq j}} dx_j
\end{aligned} \tag{4.12}$$

where the second term on the second line vanishes by the Gibbs-Duhem relation, and the partial derivative of interest may be readily identified as $\left(\frac{\partial \mu_i}{\partial x_j}\right)_{T,p,n_{k\neq j}} = n\left(\frac{\partial \mu_i}{\partial n_j}\right)_{T,p,n_{k\neq j}}$. This expression was validated numerically by evaluating the total derivative of μ_i at varying composition and total number of moles.

The entirety of the implementation of the Kempers model can be found in a public repository on GitHub. [35]

4.4 Systems with large gradients

In systems with large variations in temperature, density and concentrations, the Soret coefficient may also vary appreciably throughout the system. The approximate Soret coefficient, defined as

$$S_{T,i}^{appr} = \frac{\Delta x_i}{\bar{x}_i(1-\bar{x}_i)\Delta T} \neq \frac{\nabla x_i}{x_i(1-x_i)\nabla T} = S_{T,i} \tag{4.13}$$

where $\bar{x}_i$ is the average, or total, composition of the system, can therefore not be expected to accurately describe the Soret coefficient in the system, as it only accounts for the total concentration, temperature and density. Essentially, if the variation in composition and temperature is small enough, and the Soret coefficient is close to constant throughout the system, the concentration profile will be practically linear. In that case, $S_{T,i}^{appr}$ will be very close to the true Soret coefficient at the total composition and average temperature of the system, $S_{T,i}$. This cannot, however, generally be expected to be the case in systems with large variations in composition and temperature. To compare the Soret coefficient as measured in MD simulations with those predicted by the Kempers-model, it may therefore be insufficient to compare the reported $S_{T,i}^{appr}$[1] with the predicted $S_{T,i} = -x_i(1-x_i)\frac{\nabla x_i}{\nabla T}$. To accurately compare the results, the concentration profile in the simulation cell should be predicted and compared to the observed results. Alternatively, once one has predicted the concentration profile, it is a simple matter to compute $S_{T,i}^{appr} = -x_i(1-x_i)\frac{\Delta_{pred}x_i}{\Delta T}$, where $\Delta_{pred}x_i$ is the predicted absolute mole fraction difference accross the cell, and compare this value to the one obtained from simulations.

Two methods have been implemented to predict the concentration profile in a simulation cell, given the cell average temperature, total composition and average density. The first utilises a dynamic integration step, while the second requires a nonlinear numerical solver. Both are based on integrating the equation

$$\frac{\partial x_i}{\partial z} = -x_i(1-x_i)S_{T,i}\frac{\partial T}{\partial z} \tag{4.14}$$

across the simulation cell, assuming that the thermal conductivity is constant throughout the cell, thereby implying a constant temperature gradient at steady state.

4.4.1 Two-way integration

For the fist method, begin at a point with properties equal to the average properties of the cell, that is

$$x_i^0 = x_i, \qquad T^0 = \bar{T}, \qquad \rho^0 = \bar{\rho}. \tag{4.15}$$

Where superscripts denote the index of the integration step, and x_i denotes the total composition of the cell. In each iteration, take one step towards the hot side of the cell, $\Delta_+^n z$ and one step towards the cold side, $\Delta_-^n z$, such that

$$x_i^1 = x_i^0 + \left.\frac{\partial x}{\partial z}\right|_{z=z_0}\Delta_+^0 z \qquad x_i^{-1} = x_i^0 + \left.\frac{\partial x}{\partial z}\right|_{z=z_0}\Delta_-^0 z \tag{4.16}$$

$$x_i^{n+1} = x_i^n + \left.\frac{\partial x}{\partial z}\right|_{z=z_n}\Delta_+^n z \qquad x_i^{-n-1} = x_i^{-n} + \left.\frac{\partial x}{\partial z}\right|_{z=z_{-n}}\Delta_-^n z \tag{4.17}$$

$$T^{n+1} = \frac{\partial T}{\partial z}\Delta_+^n z \qquad T^{-n-1} = \frac{\partial T}{\partial z}\Delta_-^n z \tag{4.18}$$

$$\rho^{n+1} = \rho(\mathbf{x}^{n+1}, T^{n+1}) \qquad \rho^{-n-1} = \rho(\mathbf{x}^{-n-1}, T^{-n-1}). \tag{4.19}$$

As depicted in Figure 4.3, note that the step length towards the hot side and cold side are are given separate symbols, and that in general $\Delta_-^n z \neq -\Delta_+^n z$. This is intentional, and the added degree of freedom is used to ensure that the total composition of the system is conserved throughout the integration, such that the total composition at the end of integration is equal to the composition in the starting point. Because the total composition of the system should equal the composition in the starting point, it can be required that the total composition must be conserved in every integration step. This requirement can be formulated as

$$\frac{n_i^n + n_i^{-n}}{\sum_i n_i^n + n_i^{-n}} = x_i \tag{4.20}$$

[1] Note that prediction of the Soret coefficient in MD-simulations cam be more sophisticated than this. However they do, in some manner, rely on finite differences in temperature and concentration for their computation. [8,36,37]

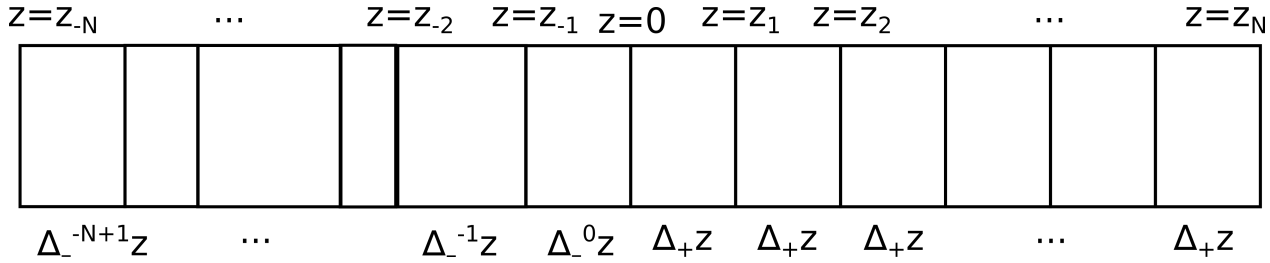

Figure 4.3: Graphical schematic of the two-way integration scheme described in Equation (4.19), with variable step lengths in one direction as described by equation (4.22).

where n_i^n and n_i^{-n} denote the number of moles of species i in the volume elements $A_{cell}\Delta_+^n z$ and $A_{cell}\Delta_-^n z$ respectively, with A_{cell} the cross sectional area of the cell. This can be expanded as

$$x_i^n \rho^n \Delta_+^n z + x_i^{-n} \rho^{-n} \Delta_-^n z = x_i \left(\rho^n \Delta_+^n z + \rho^{-n} \Delta_-^n z \right) \tag{4.21}$$

where it has been used that $n_i^{\pm n} = A_{cell} x_i^{\pm n} \rho^{\pm n} \Delta_\pm^n z$, and the cross sectional area cancels if it is constant across the cell length. Solving this equation for $\Delta_-^n z$ yields

$$\Delta_-^n z = \Delta_+^n z \frac{\rho^n (x_i^n - x_i)}{\rho^{-n}(x_i - x_i^{-n})}. \tag{4.22}$$

Thus, a fixed step length $\Delta_+ z = \Delta_+^n z \ \forall \ n$ can be chosen, while the step length in the opposite direction varies according to Equation (4.22) to ensure that the total composition of the system is conserved.

Recall that the conductivity of the fluid was assumed to be constant, thereby implying a constant temperature gradient at steady state. One can therefore write

$$\Delta_+^n T = T^{n+1} - T^n = \frac{\partial T}{\partial z} \Delta_+^n z \qquad \Delta_-^n T = T^{-n-1} - T^{-n} = \frac{\partial T}{\partial z} \Delta_-^n z \tag{4.23}$$

$$\Delta_+^n z = \frac{\Delta_+^n T}{\frac{\partial T}{\partial z}} \qquad \Delta_-^n z = \frac{\Delta_-^n T}{\frac{\partial T}{\partial z}}. \tag{4.24}$$

By substituting these expressions into the integration scheme in Equation (4.19), it is now possible to integrate over temperature rather than position. This is desirable because the concentration profile is then directly related to the Soret coefficient rather than the product of the Soret coefficient and the temperature gradient. Additionally, the need to take the dimensions of the simulation cell into account is removed. It is also advantageous because composition, temperature and density vary more rapidly with position in systems with large temperature gradients, thereby requiring shorter integration steps. By integrating over temperature rather than position one has direct control over the variation in temperature within each integration step. The integration algorithm is shown schematically in Figure 4.4.

Note that the procedure outlined here is possible also with a varying thermal conductivity, given that $T(z)$ is a one-to-one function across the entire domain at steady state. The only difference being that the scaling $\Delta_\pm^n z \mapsto \Delta_\pm^n T$ will change. Equation (4.22) relating the step lengths along the temperature axis then becomes

$$\Delta_-^n T = \Delta_+^n T \frac{\rho^n k^n (x_i^n - x_i)}{\rho^{-n} k^{-n} (x_i - x_i^{-n})}, \tag{4.25}$$

where $k^{\pm n}$ is the thermal conductivity in point $z^{\pm n}$, or equivalently, in point $T^{\pm n}$.

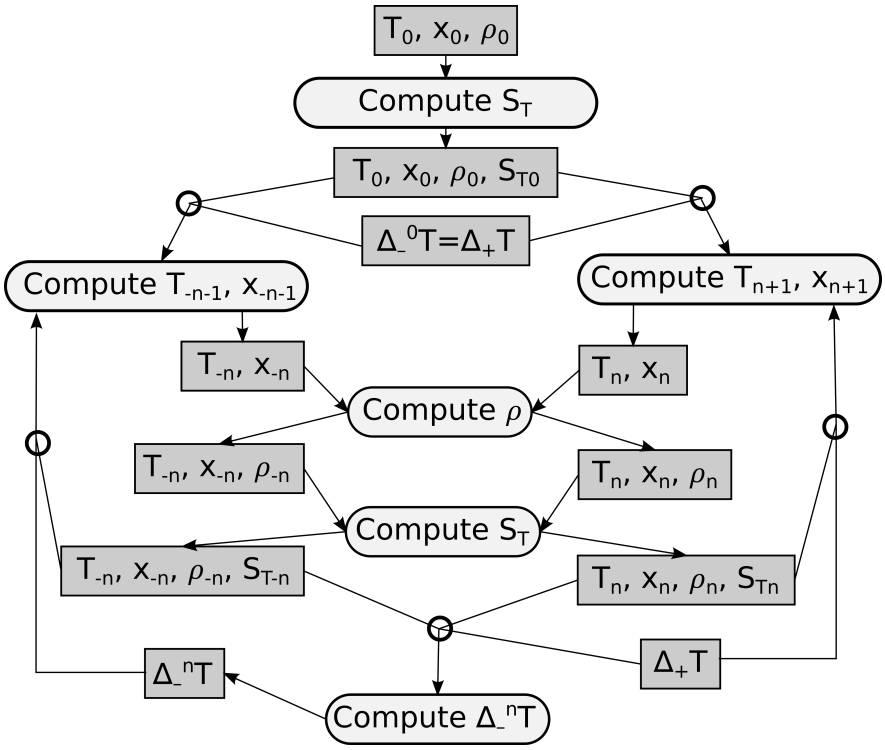

Figure 4.4: Algorithm for two-way integration of the concentration and temperature profile. $\Delta_+ T$ is held constant. Integration ends when $|T_{-n} - T_n| \geq \Delta_{end} T$, where $\Delta_{end} T$ is some predetermined value. Cornered rectangles indicate information stored in variables, rounded rectangles indicate computations, circles indicate the joining of several information streams.

4.4.2 One-way integration

Now that it has been established that one can integrate over temperature rather than position given that $T(z)$ is one-to-one, the second method of integration is far less involved. It quite simply uses a suitable numerical solver to solve the set of Equations

$$\begin{aligned} x_i^{tot} &= \frac{\int_{T_{cold}}^{T_{hot}} x_i \rho dT}{\int_{T_{cold}}^{T_{hot}} \rho dT}, \qquad i = \{1, 2, ..., N-1\} \\ x_N^{tot} &= 1 - \sum_{i=1}^{N-1} x_i. \end{aligned} \tag{4.26}$$

Where the integration is carried out using any reasonable integration scheme.

4.4.3 Comparison

It is worth noting that the two methods do not give identical results. This is not due to some error of implementation, but different boundary conditions and restrictions. The first method starts from the average state of the system $(\mathbf{x}, \bar{T}, \bar{\rho})$ and integrates outwards while conserving the total composition. The latter does not require that there is any point in the system that is at the average state. That is: The point in space where one finds the average composition, may be different from the point in which one finds the average temperature and density.

Many reported MD-results do not report accurately the temperature of the heat source/sink nor do they accurately report the temperature difference across the simulation cell or how the average temperature has been determined. This has implications for how one would compute T_{hot} and T_{cold} if using the one-way integration method. For example: The average temperature may be an arithmetic average, in which case $T_{hot} = \bar{T} + \frac{1}{2}\Delta T$ and $T_{cold} = \bar{T} - \frac{1}{2}\Delta T$ and one-way integration is straightforward. However, it may also be perfectly reasonable to use the mole average temperature $\bar{T} = \frac{\int \rho T dz}{\int \rho dz}$, in which case computing T_{hot} and T_{cold} only given $\bar{T}$ and ΔT is nontrivial, and the two-way integration scheme may be appropriate.

5 Results

Before evaluating the Kempers-model, its building blocks are given a closer look. In Section 5.1, the SAFT-VR-MIE EoS is validated against an extensive set of simulation data. Further, the implementation of the Enskog solutions for diffusion are tested against the Fuller-diffusion model in Section 5.2, and differences between the Fuller diffusion model and the Enskog solutions are discussed.

With the building blocks for the Kempers model analysed and validated, its predictions were tested against both molecular dynamics (MD) simulations and experimental data from real systems, collectively referred to as measurements. Both in the validation process and analysis of the Kempers-model, deviations between predictions and measurements are reported as the relative absolute deviation (RAD), defined as

$$\mathrm{RAD} = \frac{|\varphi^{predicted} - \varphi^{measured}|}{|\varphi^{measured}|}. \tag{5.1}$$

Further, the integration scheme outlined in Section 4.4 was also tested to analyse how the predicted approximate Soret coefficient

$$S_T^{appr} = \frac{\Delta x_i}{x_i(1-x_i)\Delta T}, \tag{5.2}$$

differs from the predicted true Soret coefficient, defined by gradients rather than finite differences.

It was observed that both the Kempers-model and the Enskog-theory implementation predict a divergent Soret coefficient. This is discussed in closer detail in Section 5.6. Finally, the derivation of the Kempers model is discussed in closer detail in Section 6.

5.1 Validation of SAFT-VR-MIE

The ThermoPack implementation of SAFT-VR-MIE was tested against an extensive set of vapour-liquid equilibrium (VLE) and pressure-volume-temperature (PVT) data obtained from MD-simulations to ensure its accuracy. An extensive set of data compiled and reviewed by Stephan et al.[38] as well as phase envelope data for LJ-fluids compiled by NIST,[39,40] were used in this process.

Before the results are reported, note that the LJ-potential in its dimensionless form is equivalent for all substances. Hence, the behaviour of the dimensionless pressure, density, temperature and phase envelope will be analytically equivalent for all substances. Dimensionless properties are marked with an asterisk and are often termed "reduced" variables. Here the term "reduced" is reserved to mean "divided by the critical parameter", and "dimentionless" refers to the transformations described in Table 5.1. Some approximate values of the dimensionless properties at ordinary conditions are also included for the convenience of the reader.

As noted, the dimensionless phase envelope of the LJ-fluid should be invariant upon changing the potential parameters. As shown in Figure 5.1, the computed dimensionless phase envelope is invariant upon changing σ- and ε parameters. However, the EoS is not consistently able to close the phase-envelope, most notably for $\sigma \approx \sigma_{\mathrm{Ar}}$. Additionally, there is some slight discrepancy as to the shape of the liquid/two-phase boundary, seen most clearly when following the thin, green line in the upper left plot of Figure 5.1, this line is centred in the thicker pink line close to the critical point, but is no longer centred at somewhat lower temperature and higher density. This minor discrepancy is deemed small enough to be insignificant.

As this report primarily deals with fluid mixtures, the reproduction of binary phase diagrams was also tested. The dimensionless binary phase envelope for six mixture corresponding to those investigated by Stephan et al.[27] were computed, shown in Figure 5.2. In all six mixtures, $\sigma_1 = \sigma_2 = \sigma_{12}$. Computing the phase envelopes with various ε_1-values produced identical results, as expected.

The general shape of the phase envelopes is as expected, and in good agreement with the envelopes reported by Stephan et al. However, the absolute values of the dimensionless pressures do not coincide with those

Table 5.1: Transformations to obtain dimensionless LJ-units. Note that in mixtures, variables may be reduced either with the parameters of one component, or with the mixing parameters σ_{12}, ε_{12}. In these cases, what parameter has been used used should be explicitly stated.

$$U^*_{LJ}(r^*) = 4\left[\left(\frac{1}{r^*}\right)^{12} - \left(\frac{1}{r^*}\right)^{6}\right]$$

		Value at $p = 1\,\mathrm{bar}$, $T = 300\,\mathrm{K}$, $\rho = 1\,\mathrm{kmol\,m^{-3}}$		
Description	Transformation	Ar	Kr	Xe
Intermolecular potential	$U^* = \frac{U}{\varepsilon}$			
Pressure	$p^* = \frac{p\sigma^3}{\varepsilon}$	$2.4{\cdot}10^{-2}$	$2.0{\cdot}10^{-3}$	$2.3{\cdot}10^{-3}$
Temperature	$T^* = \frac{Tk_B}{\varepsilon}$	2.5	1.3	1.4
Density	$c^* = c\sigma^3$	$2.3{\cdot}10^{-2}$	$3.8{\cdot}10^{-2}$	$4.2{\cdot}10^{-2}$
Time	$t^* = t\sqrt{\frac{\varepsilon}{m\sigma^2}}$			
Length	$r^* = \frac{r}{\sigma}$			

reported. Most notably the binary phase envelopes predicted by SAFT-VR-MIE for the mixture with $\frac{\varepsilon_2}{\varepsilon_1} = 0.9$ are found at a dimensionless pressure a factor of about two lower than those reported by Stephan et al. This clearly stems from a gross disagreement concerning the pure fluid bubble pressure of component 2.

The predictions of the pure fluid bubble pressure was investigated more closely by comparison with the VLE-data compiled by Stephan et al.[38] As shown in Figure 5.3, there is excellent agreement between the predictions of SAFT-VR-MIE and a large number of reported data points. Note that 13 of these data points stem from the same article as that which the binary mixture data is collected from. Results produced using various LJ-parameters were indistinguishable, as expected.

The pressures of the binary mixture phase envelopes reported by Stephan et al.,[27] have reportedly been transformed using the parameters of component 1. If one denotes dimensionless properties transformed using the parameters of component i as $\varphi^{(i)}$, that is $T^{(1)} = \frac{Tk_B}{\varepsilon_1}$, $T^{(2)} = \frac{Tk_B}{\varepsilon_2}$ and so on, it is a simple matter to show that

$$T^{(2)} = \frac{\varepsilon_1}{\varepsilon_2}T^{(1)}, \qquad p^{(2)} = \frac{\varepsilon_1\sigma_2^3}{\varepsilon_2\sigma_1^3}p^{(1)}. \tag{5.3}$$

In this manner, the pure component bubble pressure of component 2 in the $\frac{\varepsilon_2}{\varepsilon_1} = 0.9$ mixture can be compared to other dimensionless VLE-data. This is done in Figure 5.3, and it is clear that the pure component bubble pressure of component 2 in the $\frac{\varepsilon_2}{\varepsilon_1} = 0.9$ mixture falls significantly far from other reported VLE data-points. Therefore, it is believed that the discrepancy in absolute dimensionless pressure is due to confusion as to what parameters have been used to transform the pressure, rather than a significant disagreement between the models.

Finally, the PVT-behaviour of the LJ-fluid was investigated. The results presented were reproduced with various model fluids to confirm the invariance of the dimensionless behaviour of the LJ-fluid. The pressure computed with SAFT-VR-MIE was compared to PVT-data compiled by Stephan et al.[38] in 2923 phase points, shown in Figure 5.4. Aside from the fact that there is good agreement for most regions, there are several clear trends to be noted. SAFT-VR-MIE systematically over-predicts the pressure in the high-density region, both for the liquid and super-critical fluid. The relative discrepancy is largest in the low-temperature liquid region ($\approx$ +20-25 %), and close to constant ($\approx$ +10-5 %) in the super-critical region.

Close to the liquid/two-phase boundary there is a large, negative relative discrepancy ($\approx$ –20-25 %). This coincides with the region in which there is a slight deformity of the phase envelope compared to that reported by Johnson et al.[40], as shown in Figure 5.1. In the same figure, it can be seen that this is the region with

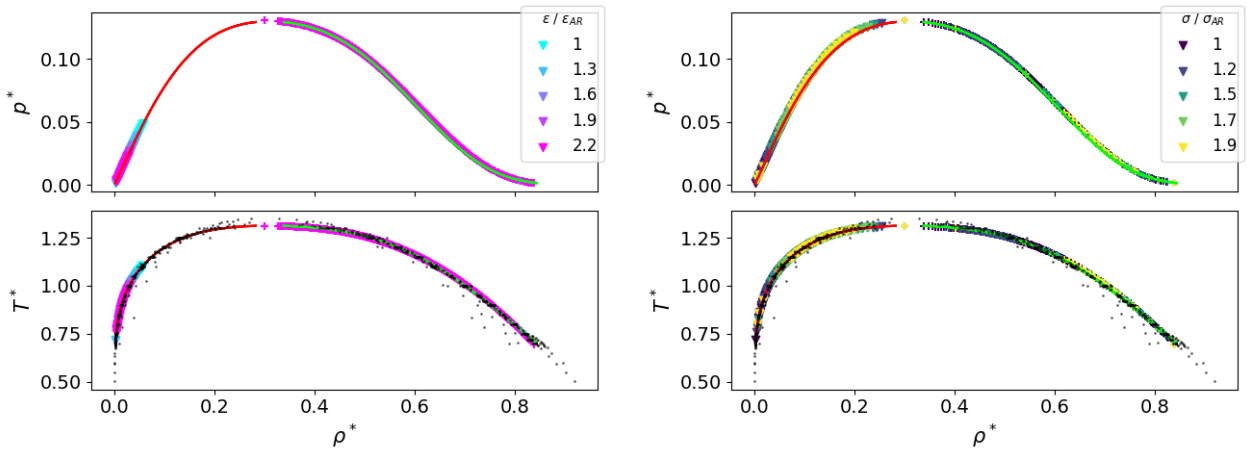

(a) Varying ε

(b) Varying σ

Figure 5.1: Dimensionless phase envelope of LJ-fluid with various σ- and ε parameters. Solid lines indicate phase envelope reported by Johnson et al.,[40] black points indicate data compiled by Stephan et al.[38] + indicates liquid-side, ▼ indicates vapour-side, predicted using SAFT-VR-MIE.

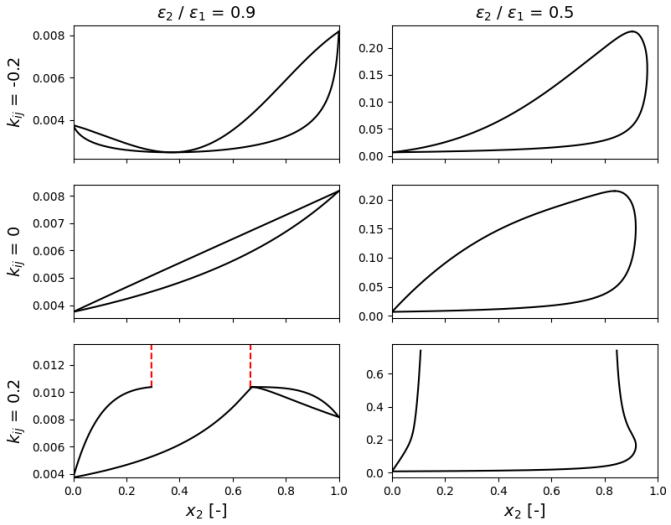

Figure 5.2: Binary liquid-vapour phase envelope for six theoretical LJ-mixtures at $T^* = 0.77$. Vertical axis is dimensionless pressure, all properties are transformed using the LJ-parameters of component 1, which are held constant. k_{ij} refers to the mixing parameter of the modified Lorentz-Berthelot rules (Eq. (2.21)). Red, dashed lines indicate liquid-liquid equilibria. In all six mixtures, $\sigma_1 = \sigma_2 = \sigma_{12}$.

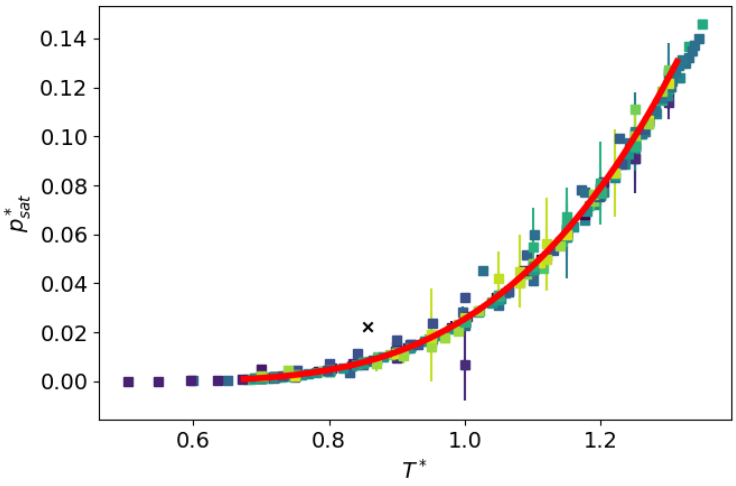

Figure 5.3: Dimensionless vapour saturation pressure of the LJ-fluid. Solid line indicates prediction by SAFT-VR-MIE. Squares indicate data compiled by Stephan et al. [38] Colours indicate different primary sources. 334 data points with statistical uncertainty <0.02 are included. Cross marks pure component bubble pressure of component 2 reported by Stephan et al. [27]

the largest spread in the VLE-data reported by Stephan et al. [38] This indicates that the region is difficult to characterise, and that the uncertainty tied to the reported data may be significant. However, all data shown in Figure 5.4 have been confirmed to not be outliers by statistical analysis by Stephan et al. [38] Additionally, for data points where statistical uncertainty was reported, only points with uncertainty < 0.015 have been included here.

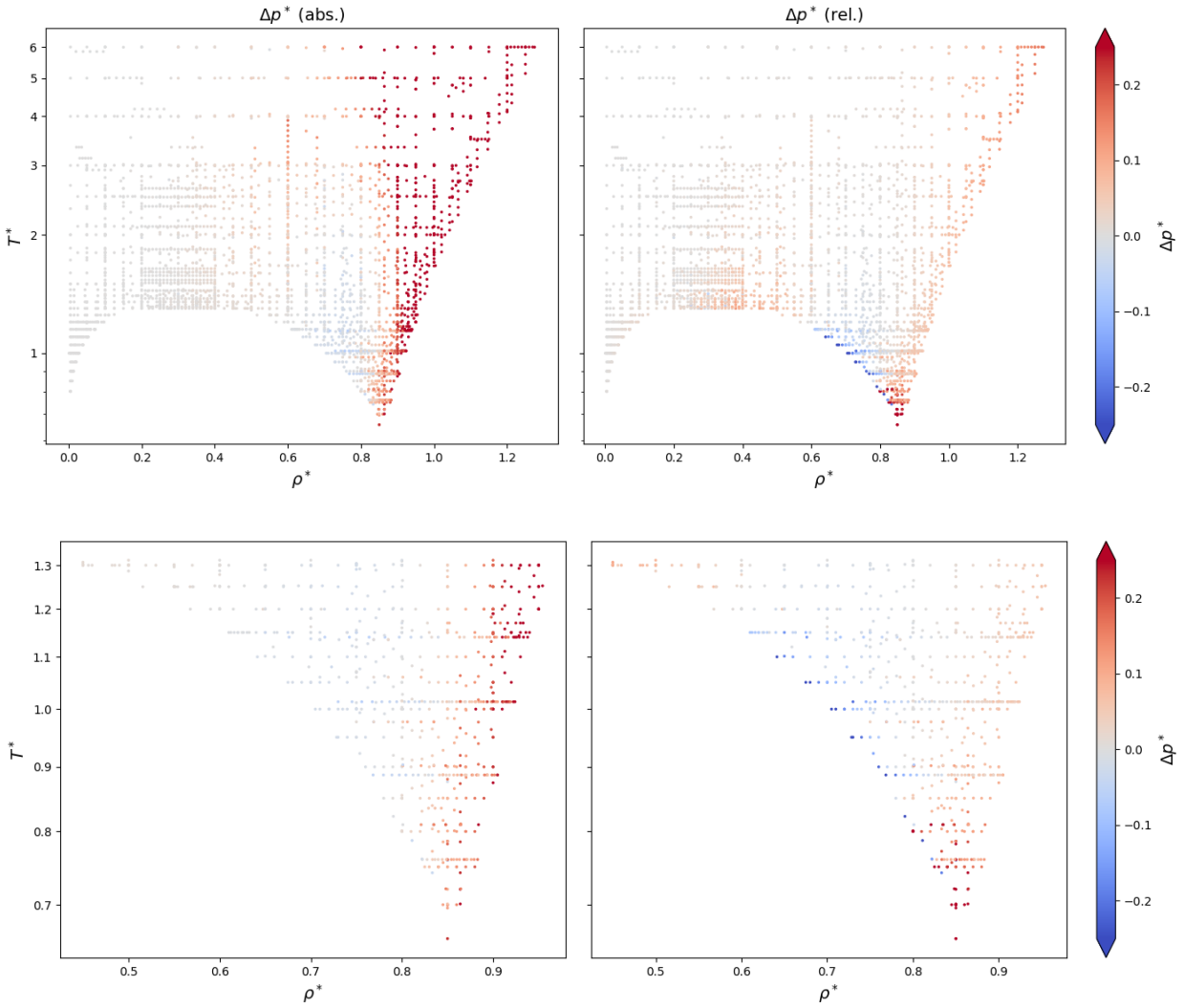

Figure 5.4: Absolute (left) and relative (right) discrepancy between pressure predicted by SAFT-VR-MIE and compiled by Stephan et al.[38] Absolute discrepancy computed as $\Delta p^*_{abs} = p^*_{\text{SAFT-VR-MIE}} - p^*_{\text{reported}}$. Relative discrepancy computed as $\Delta p^*_{rel} = \Delta p^*_{abs}/|p^*_{\text{SAFT-VR-MIE}}|$. Note cut-off values of the colour-map at $\Delta p^* = \pm 0.25$. Note also logarithmic scaling of the T^*-axis.

5.2 Analysis of the Enskog diffusion solutions

The implemented module for solution of the Boltzmann equations was tested to confirm the absence of implementation errors. This was also used as an opportunity to investigate the behaviour of the solutions at different orders of approximation, and the solutions dependencies on the various parameters. The validation was done by comparing predicted diffusion coefficients to those predicted by the Fuller diffusion model.[41] This model is based on empirical fitting of the exponents in the expression resulting from the first Enskog approximation. That is,

$$[D_{12}]_1 = \frac{3}{32\rho\sigma_{12}^2}\left[\frac{8k_BT}{\pi}\left(\frac{1}{m_1}+\frac{1}{m_2}\right)\right]^{\frac{1}{2}} \tag{5.4}$$

where the equation subject to the regression is

$$D_{12} = \frac{AT^b\left(\frac{1}{m_1}+\frac{1}{m_2}\right)^{\frac{1}{2}}}{p\left[\left(\sum_i \upsilon_{1,i}\right)^{\alpha_1}+\left(\sum_i \upsilon_{2,i}\right)^{\alpha_2}\right]^{\alpha_3}}. \tag{5.5}$$

The results of the regression presented by Fuller are shown in Table 5.2.

Table 5.2: Parameters used in Fuller-diffusion model.[41] Diffusion volumes are summed over groups of atoms in each molecule, except in the case of monoatomic species.

Parameter	Description	Value
A	Constant for all mixtures	$0.1\,\mathrm{s\,m^{-1}\,K^{-1.75}}$
b	Temperature exponent	1.75
α_1, α_2	Diffusion volume exponents	$\frac{1}{3}$
α_3	Total volume exponent	2
$\sum_i \upsilon_{1,i}$	Diffusion volume of species 1	$(16.1\,\mathrm{mL})^*$
$\sum_i \upsilon_{2,i}$	Diffusion volume of species 2	$(2.88\,\mathrm{mL})^{**}$

*Argon
**Helium

Because the Fuller-diffusion model is the result of fitting against a large set of empirical data, replication of the predictions by this model is closely analogous to replicating those data. As seen in Figure 5.5a, Enskog theory predicts a too weak temperature dependency of the diffusion coefficient ($D_{12} \sim T^{\frac{3}{2}}$, dashed lines). This was also noted by Fuller, and was his reasoning for fitting the temperature exponent. Using the temperature-dependent BH-diameter, as described in Section 4.2, gives a better fit to the Fuller-model. When using the BH-diameters, the temperature dependency was determined to $D_{12} \sim T^{1.6}$ by a simple regression on the function $D_{12} = aT^b$. Enskog theory predicts the diffusion coefficient to vanish at absolute zero, removing the need for a constant term in the regression. It is also clear that the difference between the 1st and 5th order Enskog approximations are minimal at these conditions.

The Fuller diffusion model does not predict a compositional dependency of the interdiffusion-coefficient. As seen in Figure 5.5b, this coincides with the predictions of the 1st-order Enskog approximation, upon which the Fuller-model is based. It may seem unreasonable that the 1st-order approximation gives the same prediction as the higher-order approximations in the limit of infinite dilution of one component but not the other. A closer investigation shows that in mixtures with large mass ratios, the diffusion coefficient will approach the 1st-order diffusion coefficient in the limit of infinite dilution of the heavier component, as shown in Figure 5.6a. Varying the ratio of the HS-diameters also produces results that are symmetrical about $x_1 = x_2 = 0.5$, as shown in Figure 5.6b.

Finally, the predicted pressure dependency of the diffusion coefficients was investigated. Note that the pressure dependency in the equation subject to the regression is only equivalent to that of Enskog theory for an ideal gas, where $\frac{n}{V} \propto p$, as the expression derived from Kinetic gas theory is explicit in density rather

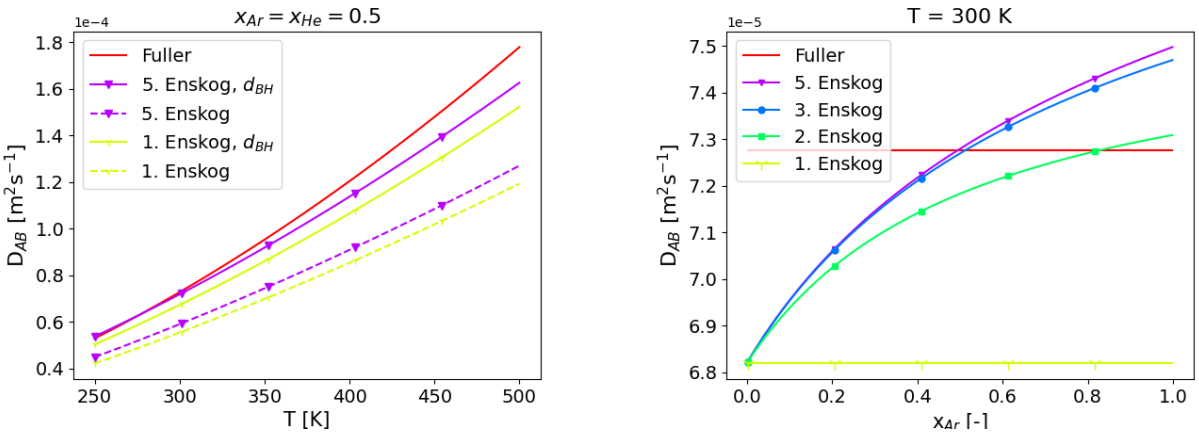

(a)

(b) All predictions with d_{BH}.

Figure 5.5: Predicted diffusion coefficients by Enskog-theory, with and without temperature dependent hard-sphere diameters, and the Fuller diffusion model. d_{BH} indicates predictions using BH-diameters. The diffusion coefficient predicted using BH-diameters has a temperature dependency of $D_{12} \sim T^{1.6}$, determined by regression.

than pressure. The predicted pressure dependency of the diffusion coefficient therefore depends on the EoS chosen to translate between pressure and density. Using the ideal gas law, the results are as shown in Figure 5.7.

Using the 1st-order approximation obviously gives the same pressure dependency as the Fuller-model when using the ideal gas law to compute the mixture density. It is however, worth noting that no additional pressure dependency appears when increasing the order of approximation, as is the case with the compositional dependency.

In summary, the implementation of the Enskog solutions performs as expected. That is, the temperature dependency of the diffusion coefficient is weaker that that which is observed experimentally and there is no compositional dependency in the first order approximation. Additionally, the pressure dependency is identical to that reported by Fuller, which is expected for the first order approximation, as Fuller did not have the pressure exponent as a free variable in the fitting of the Fuller diffusion model. Lastly, using BH-diameters improved the agreement between the Enskog solutions and the Fuller diffusion model. As argued in Section 4.2, the use of BH-diameters is a rough manner in which to approximate the effect of using a more realistic potential in the collision integrals. It was therefore expected that this would improve the agreement with the Fuller model regarding temperature dependency.

Regarding the higher order approximations there are some properties worth noting. The diffusion coefficients dependency on pressure and temperature (when not using BH-diameters) are completely contained in the 1st approximation, while the compositional dependency is contained in the higher order solutions. Mathematically, this has its roots in the fact that the entire density dependence of the diffusion solutions are contained in δ_0 in Equation (2.81), while the compositional dependency is included in every element a_{pq} of the matrix in the same equation. Likewise, the temperature dependency can be factored out of the matrix, meaning that no new temperature dependency is included upon increasing the order of approximation. The latter is shown by recognising the a_{pq} matrix elements as linear combinations of the collision integrals, which all have the same temperature dependence.

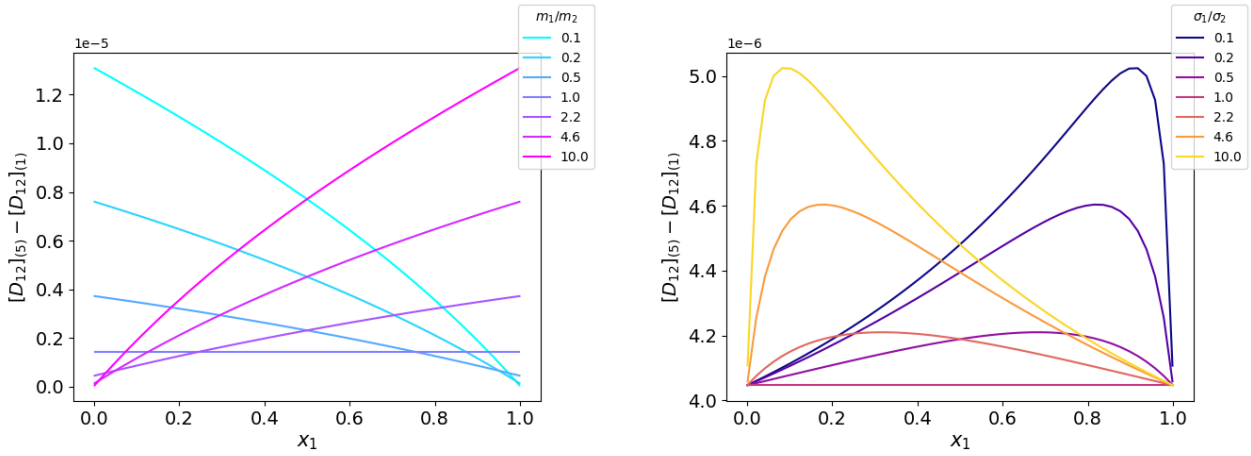

(a) Varying $\frac{m_1}{m_2}$

(b) Varying $\frac{\sigma_1}{\sigma_2}$

Figure 5.6: Compositional dependency of the interdiffusion coefficient at different mass- and hard sphere diameter ratios. In both cases the average value (mass or diameter) is kept constant and equal to $5\,\mathrm{g\,mol^{-1}}$ and 3.405 Å respectively.

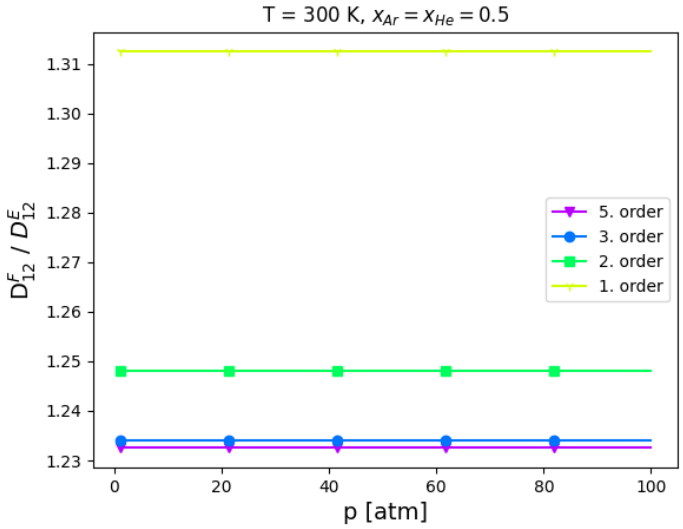

Figure 5.7: Ratio of Fuller-model to Enskog-theory diffusion coefficient, at different order of approximation, with varying pressure. Density computed from ideal gas law.

5.3 Dense Lennard-Jones fluids

In a paper published by Reith and Müller-Plathe,[8] several LJ-mixtures were simulated. The LJ-parameters were varied systematically to investigate the effect of each individual parameter on the Soret effect. A LJ-fluid here referres to a fluid described by the LJ (12,6) potential, other potentials are referred to as Mie-potentials, in which case the exponents are specified. Throughout this section the chemical names Ar, Kr, Xe and CH_4 will be used to refer to LJ-particles with the parameters listed in Table 5.3, mixtures of these particles will be termed "realistic" LJ-mixtures. Reith and Müller-Plathe report that they consistently use the combined parameters ε_{12} and σ_{12}, from the LB-mixing rules, to non-dimensionalise T and ρ. The same transformations will be used here. For the entirety of this section the SAFT-VR-MIE EoS was used, with parameters set equal to those reported for the simulation data.

Table 5.3: LJ-parameters used to produce results in Section 5.3.

Species	m [g mol^{-1}]	ε/k_B [K]	σ [Å]
Ar	39.49	120.27	3.405
Kr	83.80	167.18	3.633
Xe	131.29	206.87	3.975
CH_4	16.04	152.75	3.740

To begin, Reith and Müller-Plathe compare their algorithm to previously reported simulation results for equimolar Kr-Ar mixtures. The Kempers-model was used to predict the Soret coefficient at the same state points as those reported, as displayed in Table 5.4. The dimensionless temperatures involved were low enough that employing a BH-diameter did not change the value of S_T° by more than 0.01 mK^{-1}.

Table 5.4: Soret coefficient of Kr in an equimolar Ar-Kr, compiled by Reith and Müller-Plathe. S_T in [mK^{-1}], dimensionless variables transformed using ε_{12} and σ_{12} from the LB-mixing rules.[8]

ρ^*	T^*	K-CoM	K-CoV	S_T°	S_T Reported
0.7902	0.805	6.2	8.41	2.88	11.3
0.7902	0.824	6.12	7.17	2.82	16.2
0.803	0.81	6.17	6.32	2.87	9.1
0.797	0.805	6.11	7.41	2.88	10.5*
0.81	0.85	6.4	3.55	2.73	14.4*

*By Reith and Müller-Plathe.[8]

As can be seen there is a significant deviation from the reported simulation results, although importantly, the same sign is consistently predicted. However, looking into their sources it is decisively unclear how they have obtained the data shown in Table 5.4. Looking in to the sources, the values found for state points and coefficients are given in Table 5.5. The agreement of the Kempers-model with these data points is good, but the question regarding where the data in Table 5.4 has been found remains.

Table 5.5: Soret coefficient of Kr in an equimolar Ar-Kr mixture, using parameters closely corresponding to those in Table 5.3. Dimensionless variables are transformed using σ_{12} and ε_{12}.

ρ^*	T^*	K-CoM	K-CoV	S_T°	K-Reported
0.7902	0.815	6.16	7.75	2.85	8.19[36]
0.75	0.95	4.84	4.41	2.44	4.2[37]

Moving on, Reith and Müller-Plathe simulate several realistic equimolar mixtures, their results are compared with the Kempers model in Table 5.6. The most striking observation from this comparison is that there is

very good agreement between the Kempers model and the simulations in some cases, while the deviation is very large in others. Additionally, it seems difficult to determine whether the CoM or CoV is the more reasonable frame of reference to describe the simulation. It is not clearly stated what boundary conditions have been used in the simulation, both periodic boundary conditions and "fuzzy wall" boundary conditions have been used in simulations of the Soret effect,[15,36] and this has consequences for which FoR is the more reasonable. Nevertheless, the K-CoM model appears to agree slightly better with the simulation data than the K-CoV model.

Table 5.6: The Soret coefficient [mK^{-1}] in various equimolar mixtures at $T^* = 0.85$, $\rho^* = 0.81$.[8] The Soret coefficient refers to the first component in the mixture. The relative absolute deviation (RAD) is computed as $|S_T^{predicted} - S_T^{reported}|/|S_T^{reported}|$.

Mixture	Reported	CoM	RAD [%] CoM	CoV	RAD [%] CoV
Xe,Kr	5.1	5.5	8	8.2	61
Kr,Ar	14.4	6.8	52	1.9	87
Ar,CH_4	9.3	17.3	86	9.0	3
Xe,Ar	18.6	19.5	5	44.7	140
Kr,CH_4	22.3	16.2	27	6.4	71
Xe,CH_4	23.1	5.6	76	28.8	24

The bulk of the work published by Reith and Müller-Plathe revolves around systematically varying the LJ-parameters of one of the components in a theoretical mixture, hereafter referred to as component 1. The other component is LJ-Argon, hereafter referred to as component 2. Conveniently, the pressure at each phase point they simulated was also reported. This gave the possibility of either supplying the Kempers model with the reported pressure directly, or computing the pressure from the reported temperature and density, and supplying the model with that pressure. Of course, given that SAFT-VR-MIE is a good descriptor for the MD-simulation, the discrepancy between these pressures should be relatively small.

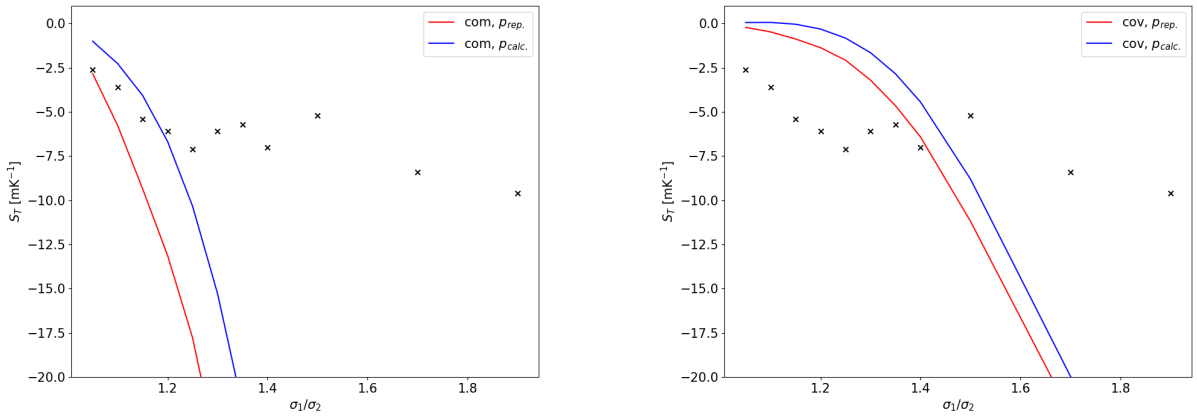

(a) K-CoM

(b) K-CoV

Figure 5.8: Component 1 Soret coefficient variation with σ_1/σ_2 ratio. Component 2 is LJ-Argon. Red line indicates predictions using reported pressure and temperature. Blue line indicates predictions using reported temperature and density. Cross marks indicate data reported by Reith and Müller-Plathe.[8]

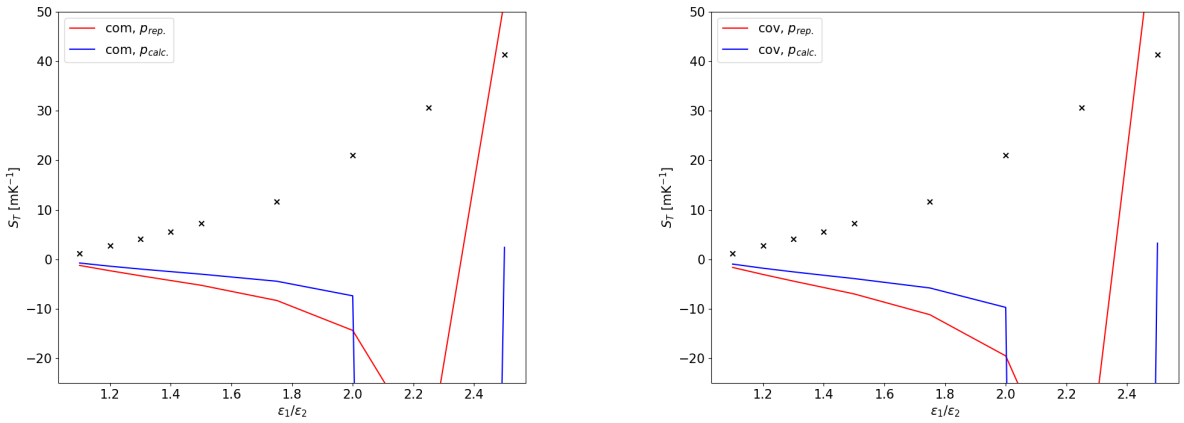

(a) K-CoM

(b) K-CoV

Figure 5.9: Component 1 Soret coefficient variation with $\varepsilon_1/\varepsilon_2$ ratio. Component 2 is LJ-Argon. Red line indicates predictions using reported pressure and temperature. Blue line indicates predictions using reported temperature and density. Cross marks indicate data reported by Reith and Müller-Plathe. [8]

The results of varying the σ_1-parameter are shown in Figure 5.8. Shortly, the fit is rather abysmal. Neither the values or the trend of the Soret coefficient are in close agreement. Further, when varying the ε_1-parameter, there is also disagreement regarding the sign of the Soret coefficient, as shown in Figure 5.9. The model appears to diverge around $\varepsilon_1 = 2.2\varepsilon_2$. The cases in which the Kempers-model is divergent will be discussed in more detail in Section 5.6. For now it suffices to say that this is clearly not in agreement with the simulation results.

The closest match with the simulation results, apart from some of the realistic mixtures, was obtained in the case where the mass ratio was varied. As shown in Figure 5.10, the Kempers-model predicts the same trend as that obtained from the simulation, but at large mass ratios the deviation in the results is still significant (RAD = $\approx$ 60 %) for both the K-CoM and K-CoV model.

As previously mentioned, Dirk and Muller-Plathe report the measured pressure in their simulations. The pressure they report was compared to the pressure computed by SAFT-VR-MIE at the given density and temperature in order to investigate whether SAFT-VR-MIE in fact is a good descriptor for the simulations they have run. As shown in Figure 5.11, the discrepancy is large. Of course, because this is a liquid phase simulation, small imprecisions in the reported density are expected to propagate to large disagreements on pressure, and the density is only reported with two significant figures. More notable is the fact that disagreement on pressure does not appear to correlate with disagreement regarding the Soret coefficient. To clearly illustrate this, the relative deviation in the Soret coefficient versus the disagreement in pressure is shown in Figure 5.12.

Perhaps the most noteworthy trend in Figure 5.11 is that SAFT-VR-MIE predicts the pressure to decrease with an increasing well depth of the first component, while the reported pressure increases. The fact that there is not only a disagreement on the pressure, but a disagreement on the sign of the pressure derivative with respect to the well depth parameter is significant. Intuitively, this appears to be of far more significance than the discrepancies in the absolute value of the pressure. This may also be related to the disagreement on the sign of the Soret coefficient in Figure 5.9.

Further, it was coincidentally recognised that varying the σ_2-parameter, while keeping σ_1 constant, the agreement between the Kempers-model and the simulation results reported for varying $\sigma_1, /\sigma_2$ ratios is far

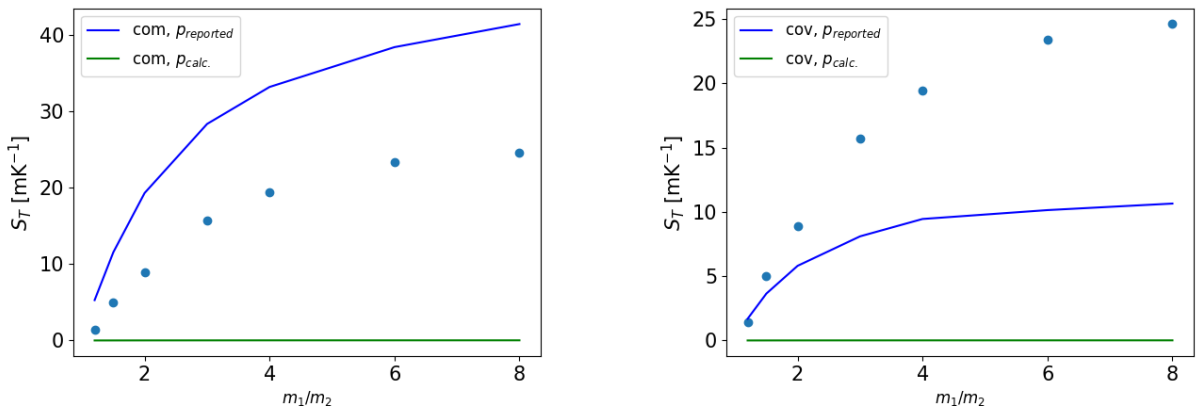

(a) K-CoM (b) K-CoV

Figure 5.10: Component 1 Soret coefficient variation with mass of component 1. Component 2 is LJ-Argon. Red line indicates predictions using reported pressure and temperature. Blue line indicates predictions using reported temperature and density. Cross marks indicate data reported by Reith and Müller-Plathe. [8]

better, especially for mixtures with σ_1/σ_2-ratios below 1.25, as shown in Figure 5.13. However, Reith and Müller-Plathe explicitly state that they have varied the parameters of component 1, while keeping component 2 constant.

Similarly, varying the ε_2-parameter while keeping ε_1 constant, there was good agreement regarding the absolute value of the Soret coefficient for $\varepsilon_1 \leq 2\varepsilon_2$, as shown in Figure 5.14. This, combined with the agreement on sign in all other cases, could raise some questions regarding what component the Soret coefficient has been reported for. However, Reith and Müller-Plathe specifically comment on the physical significance of the sign of the Soret coefficient, stating that the positive sign indicates that species 1 prefers the cold side of the simulation box, so it is believed that the coefficient is reported for component 1. If that is the case, the Kempers-model predicts a Soret coefficient of almost exactly the same magnitude, but of opposite sign compared to that obtained from simulations, as shown in Figure 5.9.

These two observations together raise some important points. First of all, recognise that most realistic mixtures have $\sigma_1/\sigma_2 < 1.25$, and $\epsilon_1/\epsilon_2 < 2$.[8] Therefore, it is not unreasonable to presume that SAFT-VR-MIE is a better descriptor for mixtures that lie in this regime. Secondly, if there has been some minor confusion regarding how Reith and Müller-Plathe have reported their simulation results, the agreement between the Kempers-model and and their results is very good in the "realistic" regime of $\sigma_1/\sigma_2 < 1.25$, and $\epsilon_1/\epsilon_2 < 2$. The agreement is in fact so good, that it is hard to believe it is coincidental. Nevertheless, the results in this section, when taken at face value, show that the Kempers-model is in gross disagreement with MD-simulations in most cases.

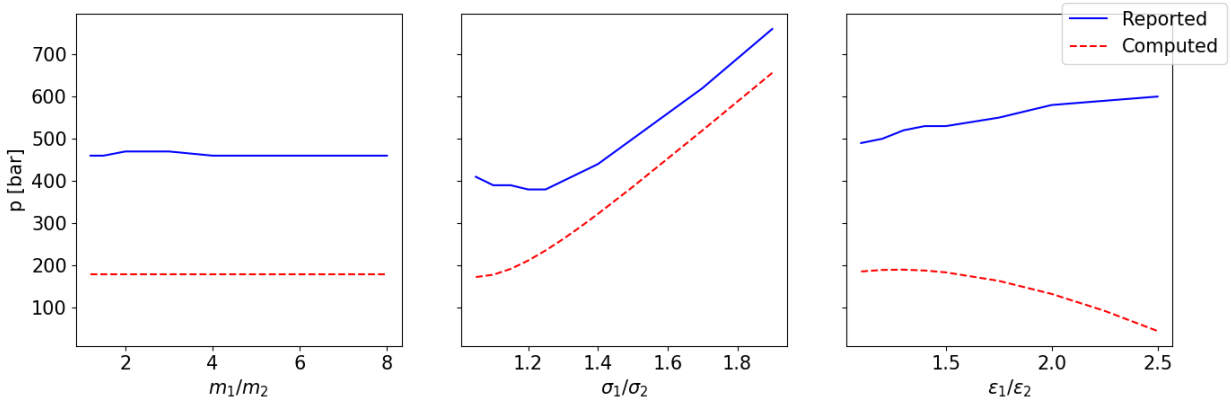

Figure 5.11: Pressure computed by SAFT-VR-MIE at $\rho^* = 0.81$, $T^* = 0.85$ for different mass ratios, HS-diameter ratios and well depth ratios. Component 2 is LJ-Argon. Temperature and density are reduced using the combined parameters σ_{12} and ε_{12}.

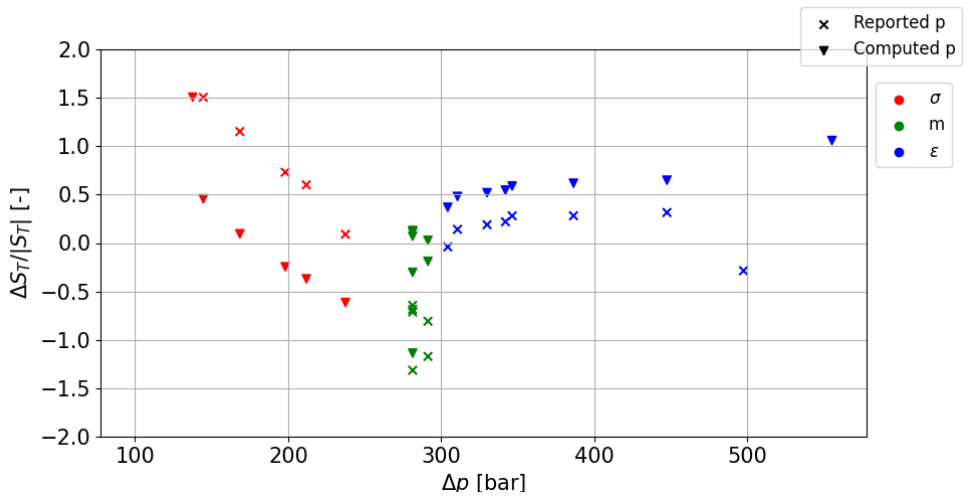

Figure 5.12: Relative discrepancy in the Soret coefficient predicted by the K-CoM model using the SAFT-VR-MIE EoS and the data reported by Reith and Müller-Plathe.[8] Relative discrepancy is computed as $\Delta S_T/|S_T| = (S_T^{reported} - S_T^{predicted})/|S_T^{reported}|$. Pressure difference is computed as $\Delta_p = p_{reported} - p_{computed}$. Crosses indicate computations using the reported pressure, triangles indicate computations using pressure computed from density and temperature by SAFT-VR-MIE. Red marks indicate the data series of varying σ-ratio, green marks indicate series of varying mass ratio, blue marks indicate the series of varying ε-ratio.

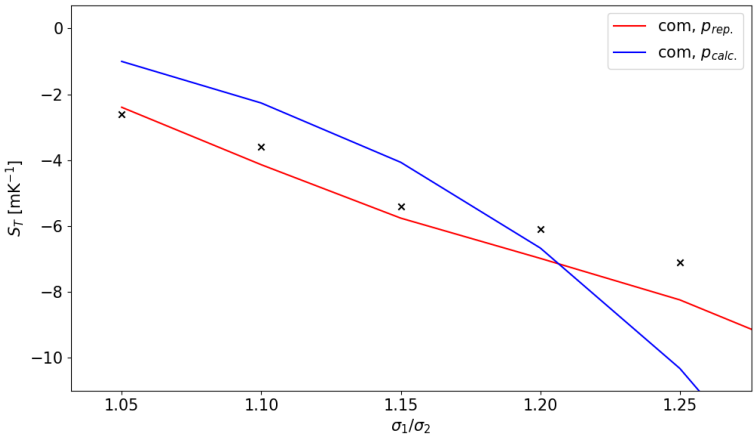

Figure 5.13: Change in the Soret coefficient of LJ-Argon as predicted by the K-CoM model when varying the HS-diameter of the second component in the mixture. The red line indicates predictions using the reported pressure, the blue line indicates predictions using pressure computed by SAFT-VR-MIE. Marks indicate simulation results reported by Reith and Müller-Plathe. [8]

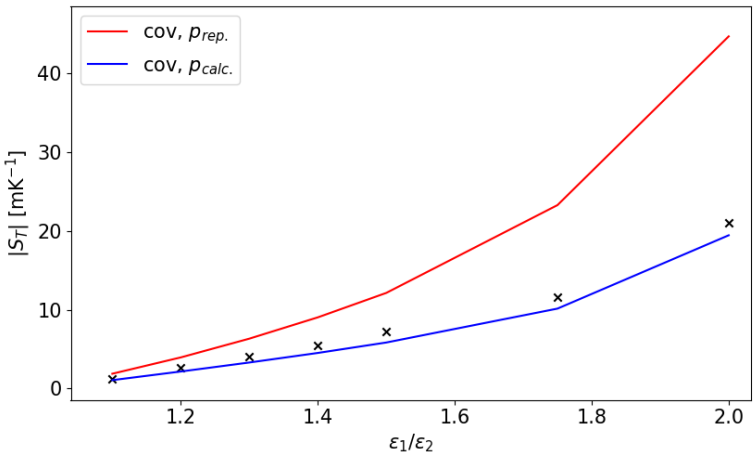

Figure 5.14: Absolute value of the Soret coefficient at various $\varepsilon_1/\varepsilon_2$ ratios. Component 2 is LJ-Argon. Red line indicates predictions using reported pressure and temperature. Blue line indicates predictions using reported temperature and density. Cross marks indicate data reported by Reith and Müller-Plathe. [8]

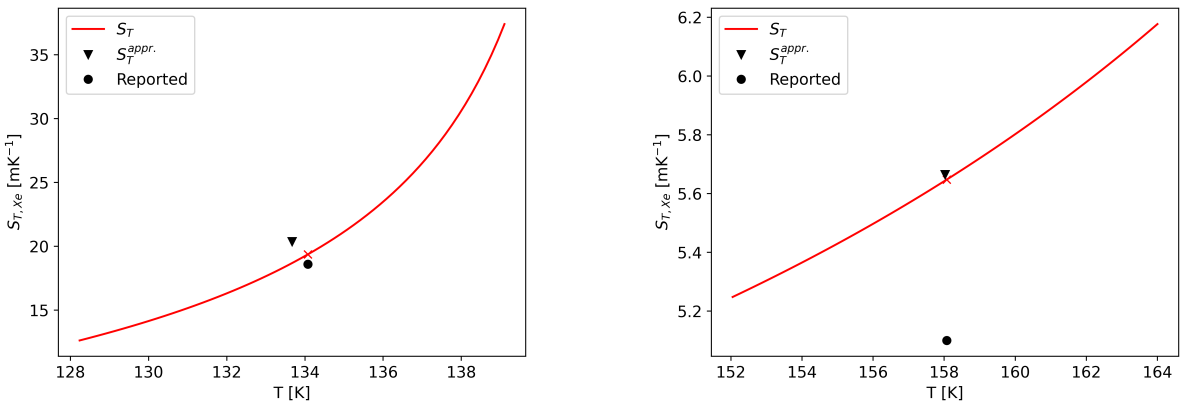

(a) K-CoM, Xe-Ar

(b) K-CoM, Xe-Kr

Figure 5.15: Soret coefficient variation throughout a simulation cell, as predicted by the K-CoM model. Red line indicates Soret coefficient, with the red cross indicating the starting point of integration. Black triangle indicates the approximate Soret coefficient. Black dot indicates the value reported by Reith and Müller-Plathe.[8]

5.4 Large temperature gradients

Due to the gradients in temperature and concentration being very large in MD-simulations, the integration scheme outlined in Section 4.4 was tested to analyse if this may be part of the explanation for the deviations of the Kempers model from the simulations data presented in Section 5.3. Reith and Müller-Plathe report that their simulation cell held a temperature difference of $\Delta T^* \approx 0.075T^* - 0.15T^*$, where $T^* = \frac{1}{2}(T_H^* + T_C^*)$, with T_H^* and T_C^* indicating the hot and cold temperatures.

The two-way integration scheme was used, starting from $T^* = 0.85$, $\rho^* = 0.81$, $x_1 = x_2 = 0.5$, the average temperature and total compositions reported by Reith and Müller-Plathe, and stopping the integration when $\Delta T^* = 0.15T^*$. Then, the approximate Soret coefficient $S_T^{appr.}$ was computed as

$$S_{T,i}^{appr.} = \frac{\Delta x_i}{\bar{x}_i(1-\bar{x}_i)\Delta T} \tag{5.6}$$

where $\bar{x}_i$ is the total composition, which is equal to the composition at the starting point of the integration as guaranteed by the integration scheme. The primary intention behind this procedure was to determine the degree to which the Soret coefficient varies throughout the simulation cell, and the order of magnitude of the potential discrepancy that could arise depending on how the coefficient is measured.

First, the integration was carried out for the Xe-Ar, and Xe-Kr mixtures. As shown in Table 5.6, the K-CoM model was in good agreement with simulation data for these mixtures. The integration results are shown in Figure 5.15.

It is clear that the predicted approximate Soret coefficient is very close to the coefficient predicted at the starting point of integration. What is more interesting to note is that the predicted variation of the Soret coefficient within the simulation cell is very large. For the Xe-Ar mixture, it is far larger than the deviation between the reported and predicted coefficient. In the Xe-Kr mixture, the difference between the reported value and the predicted value is of the same order of magnitude as the predicted variation within the cell.

This raises the question of exactly how Reith and Müller-Plathe have computed the Soret coefficient from their simulations, as they do not state this explicitly. In the cells where there is good agreement between

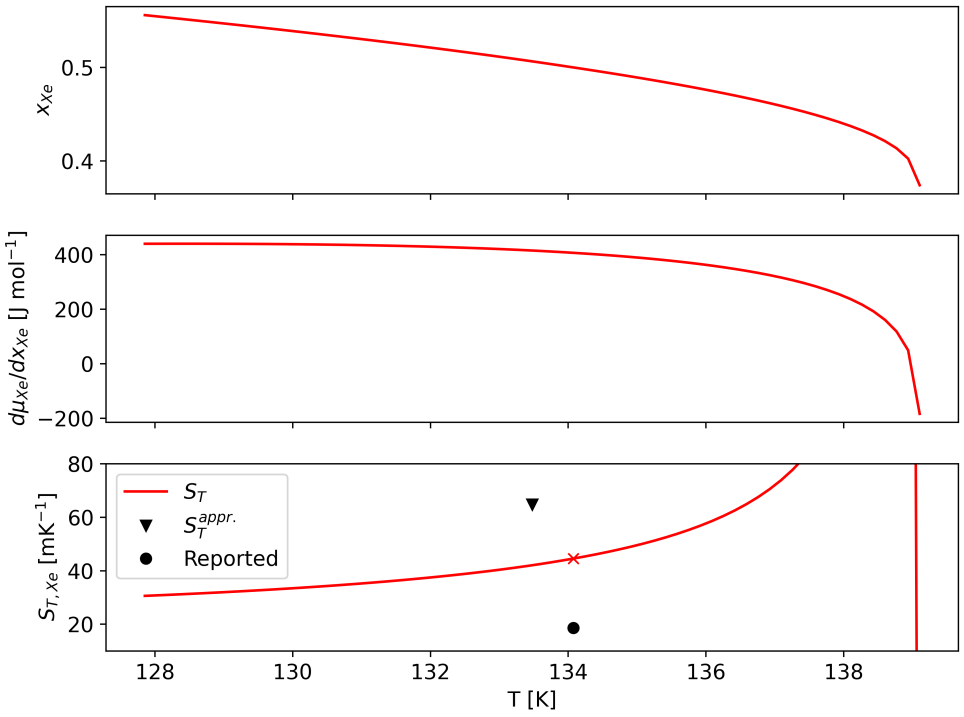

(a) K-CoV, Xe-Ar

Figure 5.16: Variation of the Soret coefficient, mole fraction and chemical potential of Xe in an Xe-Ar mixture, as predicted by the K-CoM model. Red cross marks the starting point of the integration, black dot marks the reported Soret coefficient for the mixture.

the K-CoM model and the simulation data, the Soret coefficient is predicted to vary by about 20 % (Xe-Kr) up to a factor of over 2 (Xe-Ar) between the hot and cold side of the cell. The integrations in Figure 5.15 also show that even though the variation in the Soret coefficient is large, the approximate Soret coefficient $S_T^{appr.}$ is close to the Soret coefficient at the starting point of integration. This means that if the Soret coefficient is computed in the same, very simple, manner $S_T^{appr.}$ is computed the result can be expected to be relatively close to the true Soret coefficient at the average temperature of the cell. Using other methods of computing the Soret coefficient, etc. a polynomial fit to the concentration profile can lead to very different results depending on where in the simulation cell the coefficient is evaluated.

Further, the integration was performed for some of the systems in which the agreement between the Kempers-model and the simulation data was poor. As shown in Figure 5.16, the integration diverges at approximately $x_{\mathrm{Xe}} = 0.4$, $T = 139\,\mathrm{K}$. This coincides with the point in which $\left(\frac{\partial \mu_{\mathrm{Xe}}}{\partial x_{\mathrm{Xe}}}\right)_{T,p} = 0$, indicating that the integration has reached a thermodynamically unstable composition.

To investigate this more closely, the reported points were plotted into the phase diagram predicted by SAFT-VR-MIE, shown in Figure 5.17. The first thing to note is that the manner in which the dimensionless variables are transformed does not give identical dimensionless phase envelopes, even though Reith and Müller-Plathe report that they choose this manner of transforming the variables to their dimensionless form in order to "conserve the the state point in the phase diagram of the mixed system".[8] Another point to note is that the measurements are conducted in the regime where pressure computed by SAFT-VR-MIE was shown in Figure 5.4 to deviate significantly from measured pressure data.

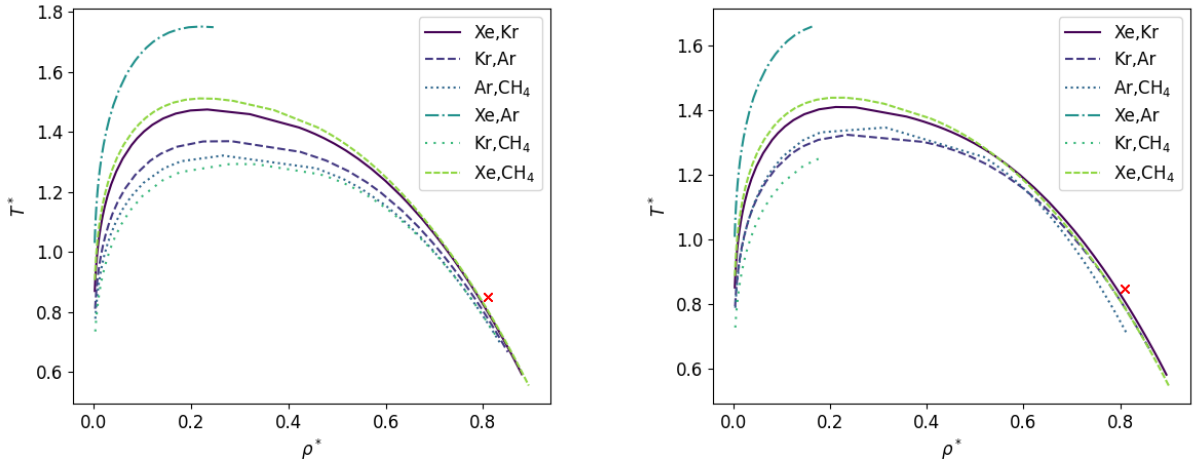

(a) $x_1 = 0.5$ (b) $x_1 = 0.4$

Figure 5.17: Phase envelope of the realistic Lennard-Jones mixtures. Red cross marks the phase point in which the Soret coefficient is reported. All dimensionless variables are transformed using the combined parameters σ_{12} and ϵ_{12} from the LB-mixing rules.

The relative deviation between pressure predicted by SAFT-VR-MIE and that obtained from MD-simulations is high very close to the liquid-two phase boundary, but rapidly decreases as the density increases, as shown in Figure 5.4. However, there is no clear correlation between the distance of the measured point in Figure 5.17 from the two-phase region and the agreement between the Kempers-model and the MD-simulations regarding the Soret coefficient. The K-CoM model agrees well with the simulation data for the Xe-Ar and Xe-Kr mixtures, but SAFT-VR-MIE does not even close the phase envelope of the Xe-Ar mixture, while the Xe-Kr two-phase region is very close to the measured point.

Perhaps the primary observation of note in this section is the large degree to which the Soret coefficient is predicted to vary within a simulation cell. This means that if meaningful comparison is to be made between a thermodynamic model and simulation results, the manner in which the Soret coefficient has been obtained from the simulation should be clear. Also worth noting is the observation that there is no clear correlation between the agreement between the Kempers-model and simulations, and the proximity of the measured point to the liquid-two phase boundary. This observation is investigated further in Section 5.5.

5.5 Real systems

It was observed in the testing against simulation data that the Kempers-model fit far better to simulations of real fluids than theoretical mixtures. In this section, the effect of using different equations of state is investigated, with the goal of determining whether the large deviations of predictions using SAFT-VR-MIE from the simulation data reported by Dirk and Müller-Plathe can be attributed to the EoS. The Kempers-models' predictions were tested against a set of measurements on liquid-phase n-alkane mixtures reported by Alonso et al.[42] as well as an extensive set of measurements on the ethanol-water system, reported by Königer et al.[43]

5.5.1 *n*-Alkane mixtures

The measurements of n-alkane mixtures by Alonso et al. are reported at varying mass density,[42] and converting the densities they report to molar densities unveils that also the molar densities were varied. They do not report the pressure at which their data is recorded. Computing the pressure from the reported densities and temperature using SRK gave pressures in the range of 100-1000 bar. There is no indication in the article that the measurements have been conducted at extremely high pressures, so this is likely a result of small errors in liquid-phase density measurements having a large impact on predicted pressure.

The critical pressure of the different mixtures computed using the SRK EoS is in the range 19-38 bar. For comparisons with the reported data, the Kempers-model was therefore supplied with a pressure of 10 bar. This pressure was chosen somewhat arbitrarily as a pressure well above the bubble pressure for all mixtures investigated, as computed by all the equations of state employed, but well below the critical pressure.

The pressure dependency of the Soret coefficient is not a primary focus of this section, but to investigate the effect the selected pressure of 10 bar may have on the primary results presented here, the Soret coefficient of equimolar mixtures predicted by the K-CoM model was computed in the range 1 - 40 bar. The trend was close to linear for all mixtures, extrema are shown in Table 5.7. The change in the Soret coefficient from 1 bar to 40 bar is in the order of approximately 10-15 %, meaning that predictions at 10 bar should be comparable to the measurements conducted by Alonso et al., given that these are in the subcritical regime.

Table 5.7: Soret coefficient of second component in several equimolar n-alkane mixtures at 1 bar and 40 bar, predicted using the K-CoM model with the SRK EoS. The Soret coefficient varied close to linearly with pressure between the two values presented in the table for all mixtures.

	$S_{T,2}$ [mK^{-1}]			$S_{T,2}$ [mK^{-1}]	
Mixture	1 bar	40 bar	Mixture	1 bar	40 bar
n-C$_{10}$/n-C$_5$	2.7	3.04	n-C$_{12}$/n-C$_8$	2.88	3.1
n-C$_{12}$/n-C$_6$	3.82	4.13	n-C$_{12}$/n-C$_7$	4.1	4.38

Several cubic equations of state are expected to be good descriptors for liquid phase n-alkane mixtures, both regarding the VLE and PVT behaviour.[44] As seen in Figure 5.18 predictions for the Soret coefficient using these equations of state are in relatively good agreement with experimental data. Although the predicted trend differs from that measured, there is agreement regarding the sign for all the mixtures, and the deviation in value is small for most compositions.

Also seen in Figure 5.18 are the predictions obtained when the K-CoM model is supplied with the PC-SAFT EoS. This leads to completely different predictions, even changing the sign of the predicted Soret coefficient. Additionally, although all the cubic equations of state give predictions in somewhat reasonable agreement with measurements, the mutual discrepancy between the various cubic equations of state is significantly larger than what was initially expected, given the similarity of these equations.[44] The large discrepancy between the equations of state is believed to result from the fact that they are, to a large degree, optimised for prediction of the VLE and PVT-behaviour, which do not depend on differences in partial molar properties

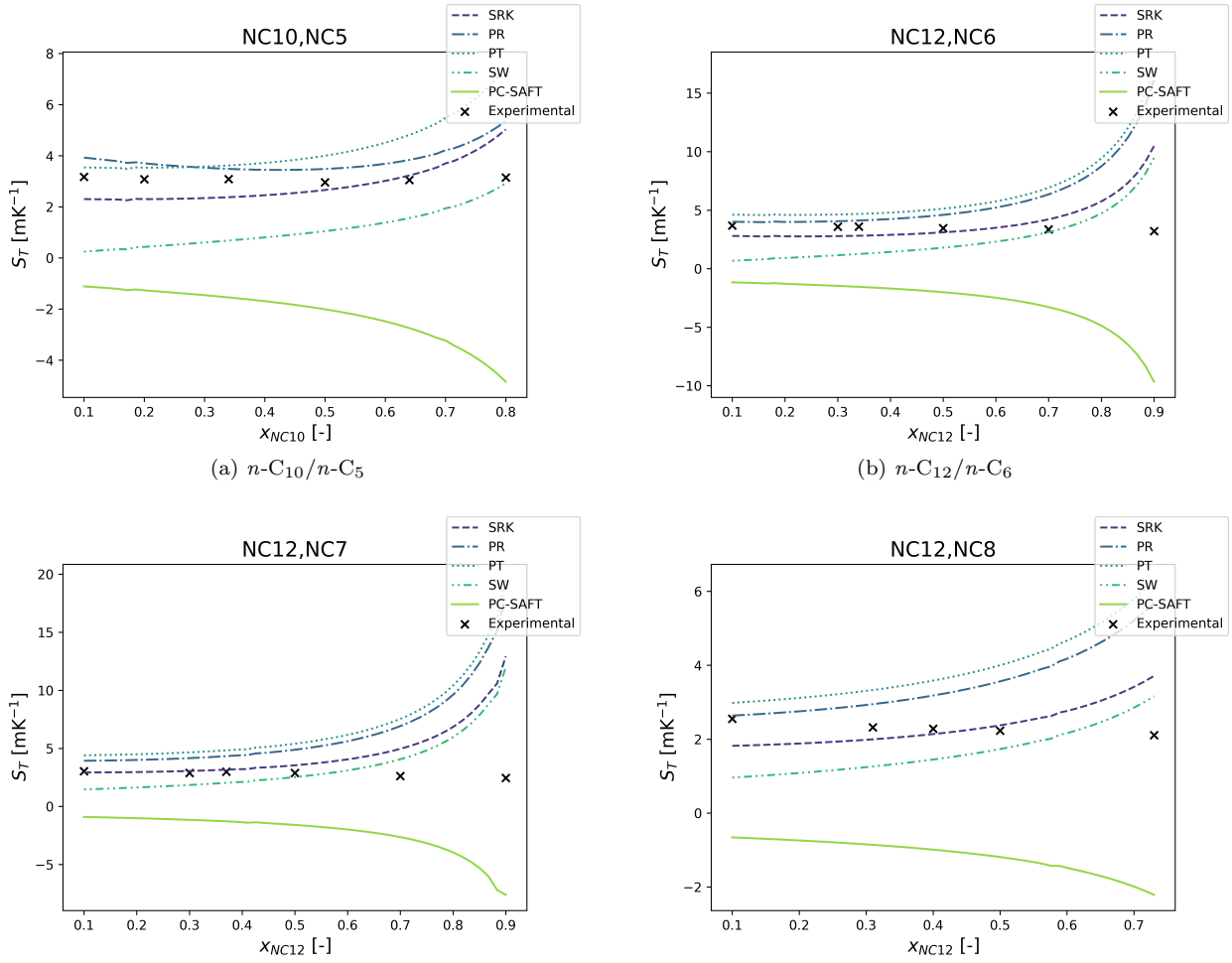

(a) n-C_{10}/n-C_5 (b) n-C_{12}/n-C_6

(c) n-C_{12}/n-C_7 (d) n-C_{12}/n-C_8

Figure 5.18: Soret coefficient in several n-alkane mixtures as a function of composition at 298 K and 10 bar. Predictions using K-CoM, data reported by Alonso et al. are recorded at mass densities varying between 0.638 g cm^{-3} and 0.741 g cm^{-3}.[42]

such as the Kempers-model.[18] To investigate this, the differences in partial molar enthalpy predicted by the different equations of state were plotted as a function of composition, as shown in Figure 5.19.

The first clear observation from Figure 5.19 is that the deviation of PC-SAFT from the cubic equations seems to be explained by the large disagreement regarding the difference in partial molar enthalpy of the components. Further, the SW-EoS appears as a slight outlier among the cubic equations, especially at low mole fractions of the heavier component in the mixture. Looking back at Figure 5.18 this disagreement is reflected in the disagreement regarding the Soret coefficient. Finally, the SRK- PR- and PT- EoS agree well on the trend of the partial molar enthalpy difference, but disagree slightly regarding the absolute value. This is again reflected in the predictions of the Soret coefficient, where the Kempers-model predicts similar trends, but varying magnitudes of the Soret coefficient when supplied with these equations of state.

Equations of state are often compared on their ability to reproduce experimental VLE data,[44] specifically the phase envelope of the systems they are used to model. The predicted phase envelope for the various n-alkane mixtures using the different equations of state are presented in Figure 5.20. Though there is notable

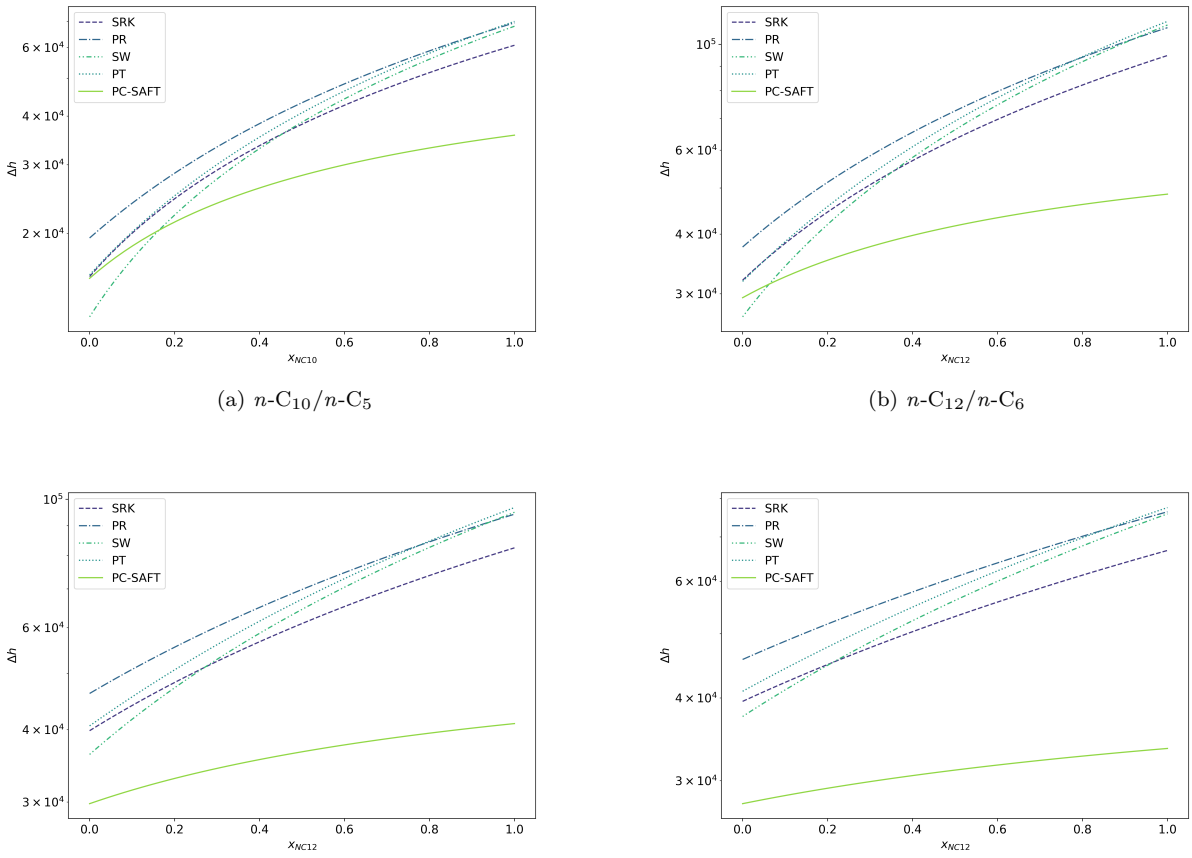

(a) n-C_{10}/n-C_5

(b) n-C_{12}/n-C_6

(c) n-C_{12}/n-C_7

(d) n-C_{12}/n-C_8

Figure 5.19: Difference in partial molar enthalpy of the components in several n-alkane mixtures. Difference is computed as $\Delta h = h_1 - h_2$, where h_1 is the first component in the mixture.

disagreement between the equations of state regarding the dew-line, the difference does not immediately seem to correlate with the disagreements regarding the Soret coefficient. For the n-C_{10}/n-C_5 mixture, there is very good agreement between the equations of state regarding the phase envelope, but this is the mixture with the largest mutual disagreement between the equations regarding the Soret coefficient. Most notably, PC-SAFT does not stand out from the cubic equations, despite predicting an opposite sign of the Soret coefficient in all mixtures.

The fact that the very small disagreement in VLE- predictions between the equations of state is so massively magnified when they are used to predict the Soret coefficient clearly indicates that the ability of an EoS to replicate the phase envelope of a mixture is at best an imprecise measure of its suitability when predicting the Soret coefficient. By this argument, the small deviations of SAFT-VR-MIE from reported data presented in Section 5.1, are not necessarily indicative of high precision in the computation of the differences in partial molar enthalpies used in the Kempers-model.

5.5.2 Ethanol-water

Predictions using PC-SAFT were tested against an extensive set of measurements carried out on the heavily associating Ethanol-Water system.[43] As seen in Figures 5.21 and 5.22, the model fails to reproduce the

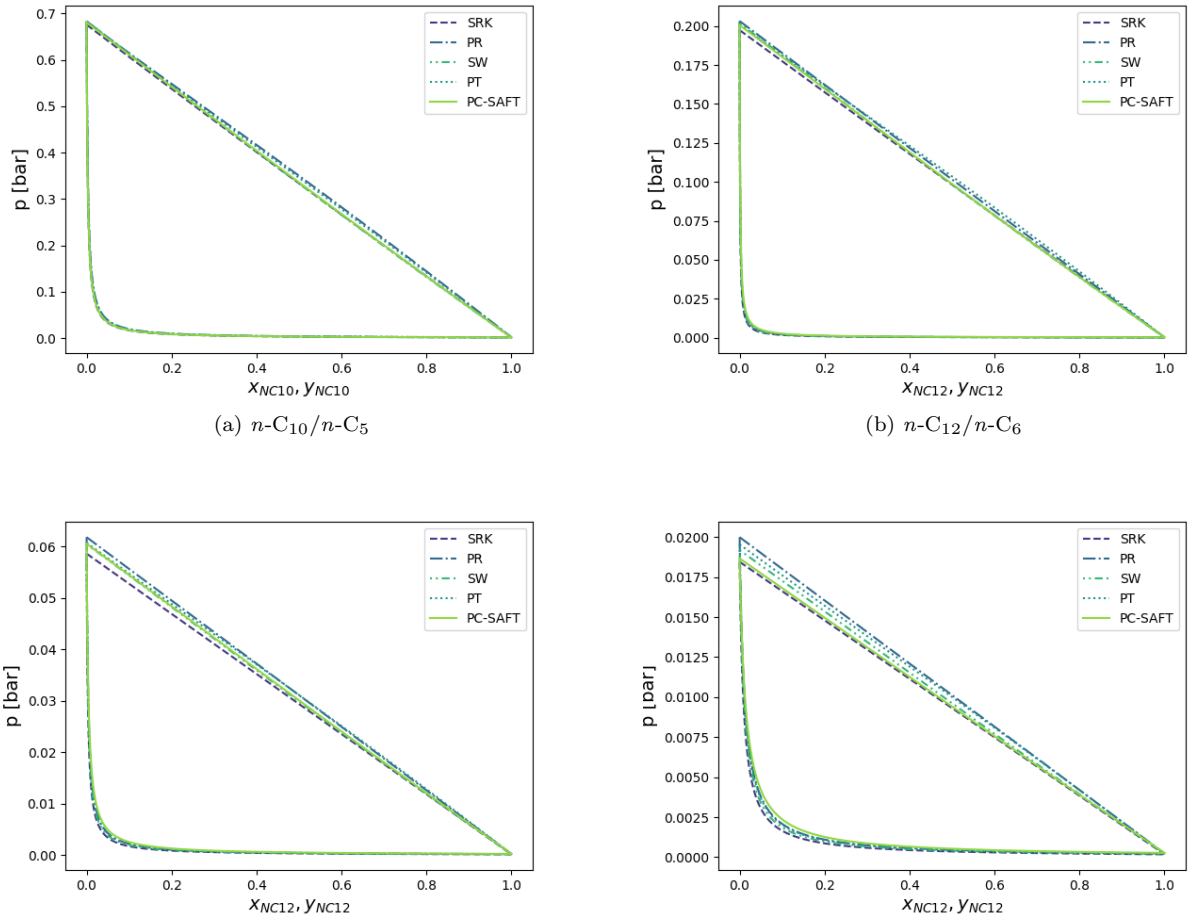

(a) n-C_{10}/n-C_5

(b) n-C_{12}/n-C_6

(c) n-C_{12}/n-C_7

(d) n-C_{12}/n-C_8

Figure 5.20: Two-phase envelope of several n-alkane mixtures computed with different equations of state. Note the different scales of the pressure axes.

change in sign that is observed. Still, the predicted trend is in good agreement with the data, and the discrepancy in absolute value is far smaller than when testing against the simulated LJ-fluids. From these measurements it is clear that the Kempers-model fares far better when measured against real systems using a well-fit EoS than against the theoretical mixtures presented in Section 5.3.

The small bump in the predictions at $w_{\mathrm{EtOH}} \approx 0.82$ was investigated more closely, and it was discovered that this was due to the thermal diffusion ratio computed from the Enskog solutions suddenly diverging in that point. This was among the observations that led to the investigation of the stability of the Enskog solutions discussed in section 5.6.

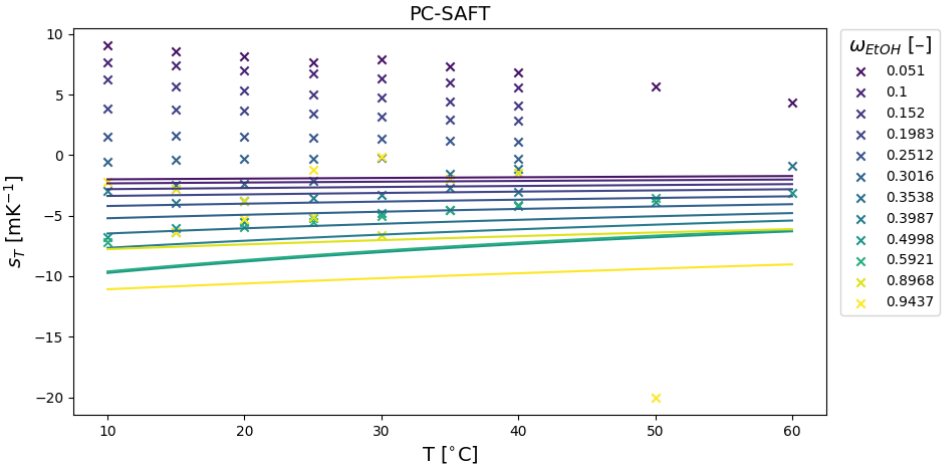

Figure 5.21: Prediction of the Soret coefficient of ethanol (EtOH) in water as a function of temperature at various ethanol weight fractions by the K-CoM model using the PC-SAFT equation of state. Marks connected by straight lines indicate measurements by Königer et al. [43]

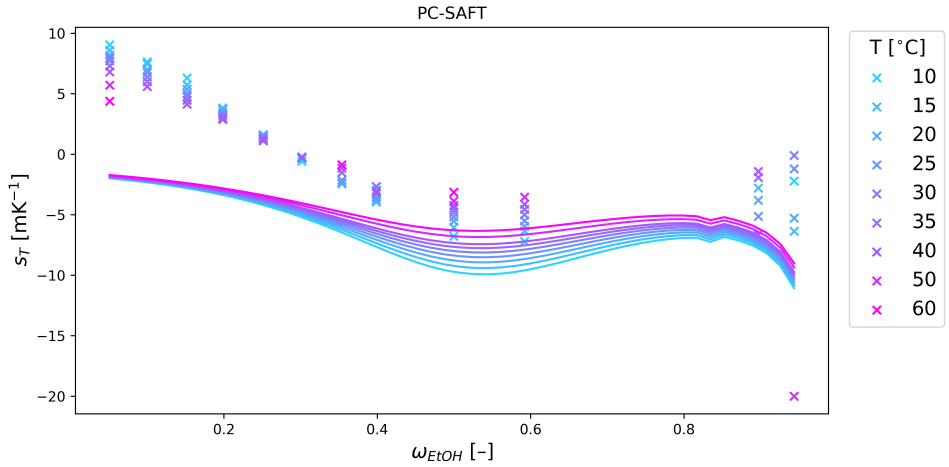

Figure 5.22: Prediction of the Soret coefficient of ethanol (EtOH) in water as a function of ethanol weight fraction at various temperatures by the K-CoM model using the PC-SAFT equation of state. Marks connected by straight lines indicate measurements by Königer et al. [43]

5.6 Model divergence

Both the Kempers-model and the Enskog solutions displayed divergent behaviour under certain conditions. This section investigates the behaviour with the intent of making clear why it is observed and if there may be a physical interpretation of the divergent solutions.

The Kempers-model was shown to diverge for a certain temperature, density and composition. From the model for a binary system, Equation (2.15), it is clear that the model will diverge when $\left(\frac{\partial \mu_i}{\partial x_j}\right)_{T,p,n_k} = 0$. This corresponds to an inflection point in the Gibbs energy as a function of composition, indicating that the mixture is thermodynamically unstable. The divergence of the thermodynamic contribution can thereby be understood as a physically sound solution rather than a failure of the model. Disregarding the kinetics, mixture at the composition of divergence will tend to separate, creating a phase boundary. At the interface between two stable phases of different composition, the Soret coefficient, as defined in Equation (3.16), is necessarily divergent, as the compositional gradient will remain nonzero even as the thermal gradient vanishes. The question of whether a meaningful definition of the Soret coefficient at the interface can be obtained is left untouched in this work.

It was observed that the implementation of the Enskog solutions produced a divergent thermal diffusion ratio for certain compositions at higher order approximations, hence the use of 5th order approximations for all figures unless otherwise is explicitly stated. In one case, shown in Figure 5.22 at approximately $w_{\mathrm{EtOH}} = 0.82$, the divergence was observed at order 5. Initially it was thought that this may be the manifestation of some higher order effect, as the composition at which the thermal diffusion ratio diverged varied from system to system. The Carnahan-Starling hard-sphere EoS is known to be capable of predicting phase transitions, [22] and the thought that higher order approximations to the Enskog solutions could do the same was entertained. However, no indication of this was found in the literature.

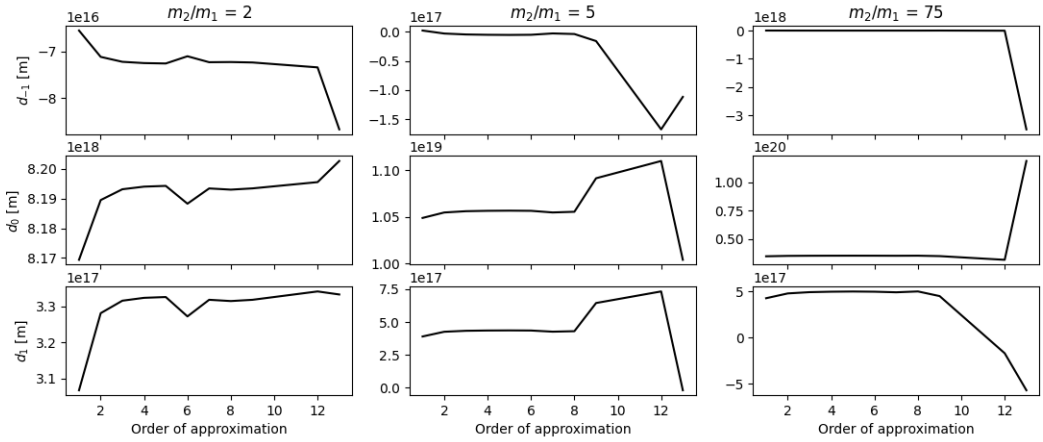

Figure 5.23: The expansion coefficients of the diffusion function **D** obtained from the Enskog solutions at different orders of approximation, with varying mass ratios. The value of parameters that were not varied are displayed in Table 5.8.

In order to investigate the divergence more closely, the expansion coefficients d_{-1}, d_0 and d_1 obtained from Equation (2.81) were computed at various orders of approximation while individually varying the hard sphere diameter ratio, the mass ratio and the composition. Note that the interdiffusion coefficient is proportional to d_0, while the thermal diffusion coefficient is proportional to d_{-1} and d_1. As shown in Figure 5.23, there is a small instability at $N = 6$ for a mass ratio of $m_2/m_1 = 2$, but the solution stabilises again until $N = 12$. Increasing the mass ratio led the solutions to become unstable at lower order approximations, with the instability kicking in at $N = 8$. Further increasing the mass ratio led the solutions to diverge more severely,

but not earlier than at $N = 7$. This was tested for mass ratios gradually increasing up to 75, with ratios of 2, 15 and 75 shown in Figure 5.23. In none of the cases did the solutions appear to stabilise at some new value when increasing the order of approximation, even up to $N = 20$.

Further, the HS-diameter ratios were systematically varied, but as shown in Figure 5.24, this does not appear to have any effect on the stability of the solutions. Finally, varying the composition at a constant mass ratio $m_2/m_1 = 2$ was tested. It appears that the solutions become stable at higher order approximations as the mole fraction of the lighter component is increased, as shown in Figure 5.25.

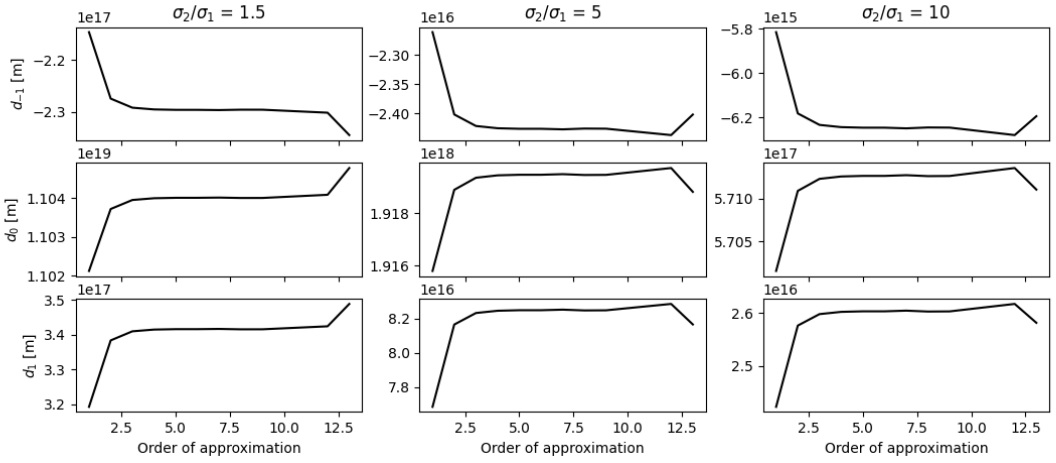

Figure 5.24: The expansion coefficients of the diffusion function **D** obtained from the Enskog solutions at different orders of approximation, at various HS-diameter ratios. The value of parameters that were not varied are displayed in Table 5.8.

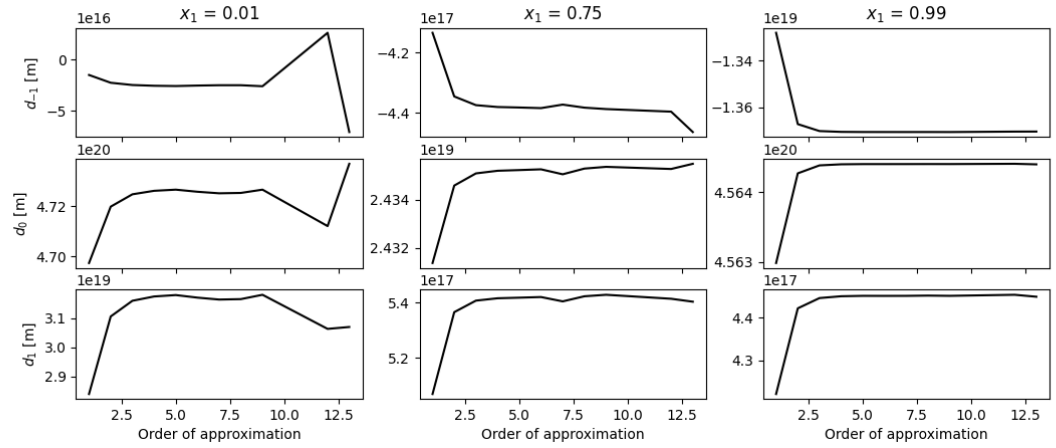

Figure 5.25: The expansion coefficients of the diffusion function **D** obtained from the Enskog solutions at different orders of approximation, at various compositions. The value of parameters that were not varied are displayed in Table 5.8.

Though these results shed some light on what conditions the Enskog solutions destabilise under, no immediate physical explanation for the instability reveals itself. Therefore, the error introduced in the numerical inversion of the matrix in Equation (2.81) was analysed by the methods described in Section 4.2.1. First

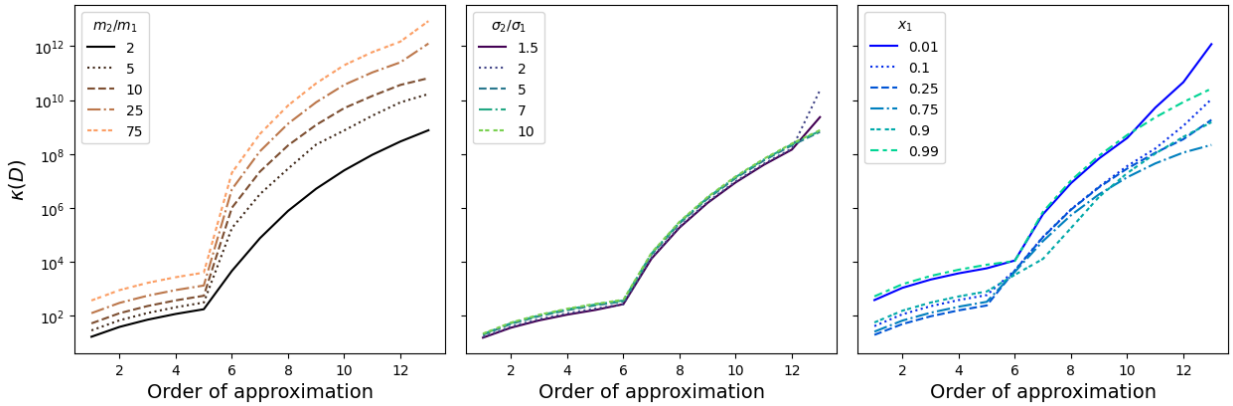

Figure 5.26: Condition number of the matrix $\underline{\boldsymbol{D}}_N$ of Equation (4.3) in various systems. Parameters for the computation are shown in Table 5.8.

the condition number $\kappa(\underline{\boldsymbol{D}}_N)$ was computed at varying mass ratios, HS-diameter ratios and compositions, as shown in Figure 5.26. Some of the trends in the instabilities can be understood from this analysis. Firstly, the condition number grows rapidly as the order of approximation goes past $N = 5$ for almost all cases shown. Secondly, increasing the mass ratio increases the condition number notably, but does not cause the "jump" at $N = 5$ to occur earlier. The HS-diameter ratio does not appear to have a significant effect on the condition number. Lastly, the trends seen in the condition number when varying the composition do not explain the stabilising effect of increasing the mole fraction of the lighter component, observed in Figure 5.25. Also noteworthy is the fact that at very high or low mole fractions, the "jump" in the condition number moves from $N = 5$ to $N = 6$.

In order to explain the trends observed when varying the composition, the alternative measure for error, ϵ_N^r presented in Section 4.2.1 was computed at various conditions, the results are presented in Figure 5.27. Firstly, note that the trends seen in the condition number are largely replicated when varying the mass ratios and the HS-diameter ratios. The condition number is a well established measure of potential error, so this agreement indicates that using ϵ_N^r as a measure for error is reasonable. The major difference in results between Figure 5.26, using the condition number and Figure 5.27, using ϵ_N^r is seen when the composition is varied. ϵ_N^r decreases with an increasing mole fraction of the lighter component. Recognise that while the condition number is a measure of potential error, ϵ_N^r is intended to be a measure of actual error. With this in mind, and observing that both $\kappa(\underline{\boldsymbol{D}}_N)$ and ϵ_N^r are small for small mass ratios, it appears that there is a stabilising effect of having a high mole fraction of low mass particles, that dominates the potential error introduced by very high or very low mole fractions of one component.

In summary, there are strong arguments to support that the observation of a divergent thermal diffusion ratio arising from the higher order Enskog approximations are the result of numerical error, rather than a physical phenomena. In this case the problem can likely be mitigated by appropriate scaling or preconditioning of the equations.

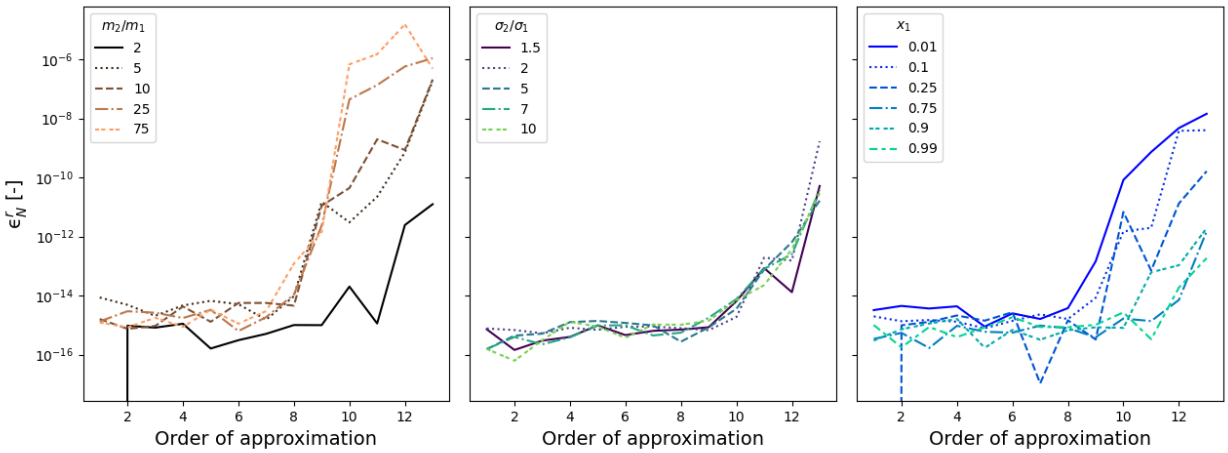

Figure 5.27: The relative error ϵ_N^r as a function of approximation order at various mass ratios, HS-diameter ratios and compositions. The value of parameters that were not varied are displayed in Table 5.8.

Table 5.8: Value of parameters that were held constant during systematic variation of the mass ratio, HS-diameter ratio and composition in Section 5.6. * Indicates the parameter that was varied. All computations were made at $T = 300\,\mathrm{K}$ and $\rho = 10\,\mathrm{mol\,m^{-3}}$.

Varied quantity	σ_1 [Å]	σ_2 [Å]	m_1 [$\mathrm{g\,mol^{-1}}$]	m_2 [$\mathrm{g\,mol^{-1}}$]	x_1 [-]
σ_2/σ_1	1	*	1	1	0.5
m_2/m_1	1	1	1	*	0.5
x_1	1	1	1	2	*

6 Revisiting the Kempers derivation

As shown in Sections 5.3 - 5.5, there are clear disagreements between the Kempers-model and both MD-simulations and experimental work. This section aims to critically assess the derivation presented in Section 2.1 with the goal of shedding light on where the discrepancies arise.

The derivation begins by regarding a two-bulb system connected by a tube of negligible volume. It is argued that if the two bulbs are held at constant and uniform temperature, such that they are at equilibrium, entropy production only occurs in the connecting tube. It is then argued that the separation of components is due to two effects that may be treated separately: Selective attraction and repulsion between the components, termed the "thermodynamic contribution" and selective collision interactions, termed the "kinetic contribution".

As it is understood, this separation of contributions is a manner of stating that one can separate the effect of the bulb temperatures from the effect of the temperature gradient. If one regards two separate, isolated subsystems at different temperatures, and distributes a set of particles between them, the maximum in the partition function is not found where the particles are evenly distributed. This is the thermodynamic contribution, the effect that even disregarding the existence of a temperature gradient, some particles will prefer the cold subsystem, while others will prefer the hot one. Naturally, for an ideal gas this contribution is zero, as an ideal gas mixture will evenly distribute itself in the available volume.

A point to note already here is that it is implied that kinetic gas theory is an exact description of the ideal gas state. This is not necessarily true, even though the ideal gas law is recovered in the limit of infinite dilution.[11] As is clear in the solution of the Boltzmann-equations in Section 2.3, kinetic gas theory describes

a dilute hard-sphere system. Using the Enskog solutions to represent an ideal gas at high densities, such as those investigated in Section 5.3, cannot be expected to be accurate. There are modifications to the Enskog solutions that account for high densities at which the volume occupied by particles becomes significant, but with these modifications the ideal gas law is naturally no longer recovered.[45] Furthermore, the species in a gas of hard spheres have a well defined chemical potential that is a function of both temperature and composition. Therefore, the thermodynamic contribution of the hard sphere state described by kinetic gas theory is non-zero, except in the limit of infinite dilution.

The kinetic contribution is stated to only reside in the connecting tube, where there is a temperature gradient. And it is assumed that the thermodynamic contribution can be modeled using equilibrium thermodynamics by regarding the canonical partition function relative to the partition function in the ideal gas state. That is, it is effectively assumed that all deviation from equilibrium, represented by the non-zero entropy production of the system, is completely described by kinetic gas theory. No further justification for these assumptions are made, but it is this argument that is used to justify that the steady state composition of the bulbs is given by a minimum in the canonical partition function relative to the partition function of the ideal gas state.

Aside from these issues, there is the issue that the Enskog solutions are explicit in density, while the Kempers-model is explicit in pressure. This raises the question of which density the Enskog solutions should be evaluated at. Because kinetic gas theory is used to represent the Soret effect in the ideal gas state, it may be reasonable to use the ideal gas density at the pressure supplied to the Kempers-model. However it may also be argued that because the Kempers-model makes use of the residual partial molar enthalpy as a function of pressure, the density in the ideal gas state should be the one obtained from the EoS used to represent the fluid. The latter of these arguments appeals to the idea that the Soret coefficient should be independent of representation, that is $S_T(T, p, \mathbf{n}) = S_T(T, V, \mathbf{n})$ for any real state. Because the residual properties change with representation, the ideal gas Soret coefficient should also change, in such a manner that the measurable Soret coefficient is invariant with respect to representation.

Finally, the partial molar enthalpies are introduced into the Kempers-model by a relation that holds only at equilibrium (Equation (2.11)). Eslamian and Saghir,[19] note this and replace the partial molar enthalpies with the activation energy of viscous flow, reportedly improving the model predictions. The relation is used in a manner that in fact is valid if Kempers' assumption that the thermodynamic contribution may be treated as an equilibrium phenomenon holds. Therefore, the improvement in predictions may actually be an indication that the underlying assumptions used to separate the thermodynamic contribution from the kinetic contribution are flawed.

In an attempt to better understand the derivation by Kempers, an alternative derivation is presented in Appendix A. The derivation disregards the issues discussed here, but follows an approach that is thought to be feasible to follow using a hard sphere reference state, rather than an ideal gas reference state. If this turns out to be feasible, the issues regarding the use of kinetic gas theory to represent the ideal gas state may be mitigated by following the derivation with a hard sphere reference state.

7 Conclusion

Although the Kempers-model fails to reliably reproduce the results of MD-simulations, the agreement with experimental data can be good when the model is supplied with an appropriate EoS. However, determining whether an EoS is suited for prediction of the Soret coefficient in a given system does not appear to be trivial.

The SAFT-VR-MIE EoS was extensively tested in its ability to reproduce the vapour-liquid equilibria and PVT-behaviour of the Lennard-Jones fluid as obtained from MD-simulations. The agreement was good or excellent at most of the phase points investigated. Still, the Kempers-model, supplied with the SAFT-VR-MIE EoS, was incapable of reliably reproducing the Soret coefficients obtained from MD-simulations of Lennard-Jones fluid mixtures. However, the relatively good agreement between the SAFT-VR-MIE EoS and MD simulations was not replicated in the MD-simulations from which data on the Soret coefficient was obtained. This, together with the fact that that the Kempers-model in some cases reproduced the Soret coefficient obtained from other simulations raises some questions regarding the reliability of the simulation data to which the Kempers-model was compared.

The possibility that disagreement between the Kempers-model and MD-simulations arose due to the large temperature gradients in the simulation cells was investigated by using Kempers-model to predict the concentration profile in the cells. This revealed that even with very large temperature differences, the concentration profile was close to linear. However, it also became clear that the Soret coefficient may vary significantly within a simulation cell. Therefore, if one is to compare the model predictions with data obtained from simulations, the manner in which the Soret coefficient has been obtained from the simulation should be made clear.

With this in mind, using SAFT-VR-MIE or similar equations of state that can be supplied with the same parameters as an MD-simulation represents an intriguing possibility for extensively testing the Kempers-model in other regions of the phase diagram than those tested here. This method of testing the model gives complete control over the parameters involved, and more investigation can provide further insight into how and why the model fails.

A comparison of of the Kempers-model predictions and experimental measurements of several n-alkane mixtures using various equations of state revealed the high sensitivity of the model to the EoS with which it is supplied. Further, it was uncovered that although different equations of state are in good agreement regarding the phase envelope of a mixture, they cannot be expected to yield the same Soret coefficient when used in combination with the Kempers-model. Comparing the partial molar enthalpies obtained from the different equations of state gives a better indication of how good their agreement will be on the Soret coefficient. This observation captures some of the essence of the predictive problem of the Kempers-model. It is highly sensitive to the EoS with which it is supplied, but comparing an EoS to largely available VLE- or PVT data for a mixture does not necessarily give a good indication of whether the EoS is suited for prediction of the Soret coefficient.

Critical assessment of the derivation presented by Kempers reveals some potential flaws. These are clearly not completely detrimental to the model, as it gives predictions in agreement with measurements in some cases. However, this may explain why the model in some cases fits very well with experiments and simulations, and in other cases misses completely. The general notion of using kinetic gas theory to describe a reference state and a thermodynamic approach to describe the deviation of a mixture from this reference state remains an appealing one. The choice of reference state and the exact manner in which one should proceed to describe the deviation from it, is therefore a matter deserving of further attention.

7.1 Further work

An immediate current limitation of the existing implementation of the Kempers-model is the restriction of the Kinetic gas module to a binary system. Chapman and Cowling present solutions for multicomponent systems closely analogous to those for binary systems, but it is not immediately clear how one should apply

the summational expressions presented by Tompson et al. to produce a working implementation. However, the Enskog solutions have been shown to converge quickly before destabilising due to numerical error, additionally the computational cost of computing the Enskog solutions increases rapidly with increasing order of approximation. Therefore, it may be more feasible to seek a simpler implementation of the multicomponent Enskog solutions that does not go to arbitrary order, than to attempt the application of the summational expressions by Tompson et al. to the multicomponent case.

Looking further into the derivation of the Kempers-model is justified. Following the general approach presented by Kempers, but using a hard sphere reference state is believed to possibly improve the model, especially in the high-density region. If this is done, the manner in which the kinetic contribution is separated from the thermodynamic contribution to the Soret effect deserves close attention.

Finally, all testing of the Kempers-model in this work has been conducted in the liquid region of the phase diagram. To further assess the effects of the selected EoS on the Kempers-model it may be fruitful to investigate larger portions of the phase diagram for a single mixture. In this sense, the SAFT-VR-MIE EoS is of special interest, as it can be supplied with the exact same parameters as a simulation, giving good grounds for comparison.

References

[1] M. Rahman and M. Saghir, International Journal of Heat and Mass Transfer **73**, 693 (2014).

[2] S. Kjelstrup, D. Bedeaux, E. Johannessen, and J. Gross, *Non-Equilibrium Thermodynamics for Engineers*, 2nd ed. (World Scientific Publishing, 2017).

[3] L. Onsager, Phys. Rev. **37**, 405 (1931).

[4] K. Dill and S. Bromberg, *Molecular Driving Forces*, 2nd ed. (Garland Science, 2011).

[5] K. B. Oldham, J. C. Myland, and A. M. Bond, *Electrochemical Science and Technology*, 1st ed. (Wiley, 2013).

[6] P. M. Doran, *Bioprocess engineering principles*, 2nd ed. (Elsevier, 2013).

[7] S. R. De Groot and P. Mazur, *Non-equilibrium thermodynamics* (Courier Corporation, 2013).

[8] D. Reith and F. Müller-Plathe, The Journal of Chemical Physics **112**, 2436 (2000).

[9] K. Shukla and A. Firoozabadi, Industrial & engineering chemistry research **37**, 3331 (1998).

[10] A. Firoozabadi, K. Ghorayeb, and K. Shukla, AIChE Journal **46**, 892 (2000).

[11] S. Chapman and T. G. Cowling, *The mathematical theory of non-uniform gases*, 2nd ed. (Cambridge university press, Bentley House, 200 Euston Road, London, N.W. 1, 1964).

[12] H. Van Beijeren and M. Ernst, Physics Letters A **43**, 367 (1973).

[13] H. Van Beijeren and M. H. Ernst, Physica **68**, 437 (1973).

[14] D. Longree, J. Legros, and G. Thomaes, The Journal of Physical Chemistry **84** (1980).

[15] J. Kincaid and B. Hafskjold, Molecular Physics **82**, 1099 (1994).

[16] R. Dawson, F. Khoury, and R. Kobayashi, AIChE Journal **16**, 725 (1970).

[17] H. Hanley, R. McCarty, and E. Cohen, Physica **60**, 322 (1972).

[18] L. J. T. M. Kempers, The Journal of Chemical Physics **115**, 6330 (2001).

[19] M. Eslamian and M. Z. Saghir, Journal of Non-Equilibrium Thermodynamics **35**, 51 (2010).

[20] R. C. Reid, J. M. Prausnitz, and B. E. Poling, *The properties of gases & liquids*, 4th ed. (McGraw-Hill Book Company, 1987).

[21] T. W. Leland and P. S. Chappelear, Industrial & Engineering Chemistry **60**, 15 (1968).

[22] N. F. Carnahan and K. E. Starling, The Journal of chemical physics **51**, 635 (1969).

[23] H. Hansen-Goos and R. Roth, The Journal of chemical physics **124**, 154506 (2006).

[24] R. Dohrn and J. M. Prausnitz, Fluid phase equilibria **61**, 53 (1990).

[25] T. Lafitte, A. Apostolakou, C. Avendaño, A. Galindo, C. S. Adjiman, E. A. Müller, and G. Jackson, The Journal of chemical physics **139**, 154504 (2013).

[26] SINTEF, "ThermoPack," `https://github.com/SINTEF/thermopack/` (2020).

[27] S. Stephan, K. Langenbach, and H. Hasse, The Journal of Chemical Physics **150**, 174704 (2019).

[28] E. Tipton, R. Tompson, and S. Loyalka, European Journal of Mechanics - B/Fluids **28**, 353 (2009).

[29] R. Tompson, E. Tipton, and S. Loyalka, European Journal of Mechanics - B/Fluids **28**, 695 (2009).

[30] E. Tipton, R. Tompson, and S. Loyalka, European Journal of Mechanics-B/Fluids **28**, 335 (2009).

[31] S. Loyalka, E. Tipton, and R. Tompson, Physica A: Statistical Mechanics and its Applications **379**, 417 (2007).

[32] R. Taylor and R. Krishna, *Multicomponent Mass Transfer*, 1st ed. (Wiley, 1993).

[33] J. M. O. de Zárate, The European Physical Journal E **42**, 1 (2019).

[34] V. G. Jervell, "KineticGas," `https://github.com/vegardjervell/Kineticgas` (2021).

[35] V. G. Jervell, "Kempers01," `https://github.com/vegardjervell/Kempers01` (2021).

[36] D. MacGowan and D. J. Evans, Phys. Rev. A **34**, 2133 (1986).

[37] G. V. Paolini and G. Ciccotti, Phys. Rev. A **35**, 5156 (1987).

[38] S. Stephan, M. Thol, J. Vrabec, and H. Hasse, Journal of Chemical Information and Modeling **59**, 4248 (2019).

[39] J. J. Potoff and A. Z. Panagiotopoulos, The Journal of Chemical Physics **109**, 10914 (1998).

[40] J. K. Johnson, J. A. Zollweg, and K. E. Gubbins, Molecular Physics **78**, 591 (1993).

[41] E. N. Fuller, P. D. Schettler, and J. C. Giddings, Industrial & Engineering Chemistry **58**, 18 (1966).

[42] D. Alonso de Mezquia, M. Mounir Bou-Ali, J. A. Madariaga, and C. Santamaría, The Journal of Chemical Physics **140**, 084503 (2014).

[43] A. Königer, B. Meier, and W. Köhler, Philosophical Magazine **89**, 907 (2009).

[44] I. Ashour, N. Al-Rawahi, A. Fatemi, and G. Vakili-Nezhaad, "Applications of equations of state in the oil and gas industry," (IntechOpen, 2011) pp. 165–178.

[45] J. O. Hirschfelder, C. F. Curtiss, and R. B. Bird, *Molecular Theory of Gases and Liquids* (John Wiley & Sons, 1954).

A Revisiting the derivation by Kempers

This derivation is presented as an alternative to the derivation by Kempers,[18] taking Equation (2.8) as a starting point,

$$\frac{1}{\sum_{AB} v_i}\Delta\left(\frac{\mu_i(T,V,\mathbf{n})-\mu_i^{ig}(T,V,\mathbf{n}^{ig})}{T}\right)=\frac{1}{\sum_{AB} v_N}\Delta\left(\frac{\mu_N(T,V,\mathbf{n})-\mu_N^{ig}(T,V,\mathbf{n}^{ig})}{T}\right) \qquad i=\{1,2,...,N-1\}. \tag{A.1}$$

Recall that while the temperature, volume and total composition is equal in the real state and the ideal gas state, the mole numbers and pressure in each bulb is different, even though the pressure of the two bulbs in the ideal gas state are equal, and the pressure of the two bulbs in the real state are equal. That is, $p_A^{ig}=p_B^{ig}\neq p_A=p_B$. Kempers treats Equation (A.1) by applying Taylor expansions about the average of bulb A and B, and states that the resulting set of equations is only valid for small temperature and concentration gradients, while Equation A.1 is stated to be generally valid.

Instead of employing a Taylor expansion, an attempt is here made to treat Equation (A.1) by considering the limiting case in which the connecting tube is infinitely short, and the temperature differences infinitely small but still non-zero. Note that in this limit the truncated Taylor expansions employed by Kempers should be exactly equal to the functions that are expanded. In this limit, we can make the replacements $v_i^A+v_i^B=2v_i$ and $\Delta\mapsto\nabla$. Equation (A.1) then reads

$$\frac{1}{v_i}\nabla\left(\frac{\mu_i(T,V,\mathbf{n})-\mu_i^{ig}(T,V,\mathbf{n}^{ig})}{T}\right)=\frac{1}{v_N}\nabla\left(\frac{\mu_N(T,V,\mathbf{n})-\mu_N^{ig}(T,V,\mathbf{n}^{ig})}{T}\right) \qquad i=\{1,2,...,N-1\}. \tag{A.2}$$

Only the left hand side of the equation will be explicitly treated here, the equivalent treatment is given to the right hand side. Begin by rewriting the term in the parentheses in terms of the fugacity coefficient and the compressibility factor,

$$\begin{aligned}
\mu_i(T,V,\mathbf{n})-\mu_i^{ig}(T,V,\mathbf{n}^{ig}) &= \mu_i(T,V,\mathbf{n})-\mu_i^{ig}(T,V,\mathbf{n})-\left(\mu_i^{ig}(T,V,\mathbf{n}^{ig})-\mu_i^{ig}(T,V,\mathbf{n})\right)\\
&= \mu_i^r(T,V,\mathbf{n})-\left[\mu_i^{ig}(T,V,\mathbf{n}^{ig})-\mu_i^{ig,\circ}(T,p_{ref})-\left(\mu_i^{ig}(T,V,\mathbf{n})-\mu_i^{ig,\circ}(T,p_{ref})\right)\right]\\
&= \mu_i^r(T,V,\mathbf{n})-RT\left[\ln\left(\frac{n_i^{ig}RT}{p_{ref}V}\right)-\ln\left(\frac{n_iRT}{p_{ref}V}\right)\right]\\
&= \mu_i^r(T,p,\mathbf{n})+RT\ln(Z)-RT\ln\left(\frac{n_i^{ig}}{n_i}\right)\\
&= RT\left(\ln(\phi_i(T,p,\mathbf{x}))+\ln(Z)-\ln\left(\frac{n_i^{ig}}{n_i}\right)\right)
\end{aligned} \tag{A.3}$$

Where μ° denotes the chemical potential of the pure component. After exposing the right hand side of Equation (A.2) to the same treatment, the prefactor RT cancels from each side. Now the gradient of each

term can be expanded, starting with the fugacity and the compressibility,

$$\begin{aligned}
\nabla \ln \phi_i &= \left(\frac{\partial \ln \phi_i}{\partial T}\right)_{p,\mathbf{x}} \nabla T + \left(\frac{\partial \ln \phi_i}{\partial p}\right)_{T,\mathbf{x}} \underbrace{\nabla p}_{=0} + \sum_j \left(\frac{\partial \ln \phi_i}{\partial x_j}\right)_{T,p,x_{k\neq j}} \nabla x_j, \\
\frac{1}{\nabla T}\nabla \ln \phi_i &= \left(\frac{\partial \ln \phi_i}{\partial T}\right)_{p,\mathbf{x}} - \sum_j \left(\frac{\partial \ln \phi_i}{\partial x_j}\right)_{T,p,x_{k\neq j}} x_j(1-x_j)S_{T,j}, \\
\nabla \ln(Z) &= \left(\frac{\partial \ln(Z)}{\partial T}\right)_{p,\mathbf{x}} \nabla T + \left(\frac{\partial \ln(Z)}{\partial p}\right)_{T,\mathbf{x}} \underbrace{\nabla p}_{=0} + \sum_j \left(\frac{\partial \ln(Z)}{\partial x_j}\right)_{T,p,x_{k\neq j}} \nabla x_j, \\
\frac{1}{\nabla T}\nabla \ln(Z) &= \left(\frac{\partial \ln(Z)}{\partial T}\right)_{p,\mathbf{x}} - \sum_j \left(\frac{\partial \ln(Z)}{\partial x_j}\right)_{T,p,x_{k\neq j}} x_j(1-x_j)S_{T,j}.
\end{aligned} \tag{A.4}$$

For the molar gradients, denoting the total number of moles as n,

$$\begin{aligned}
\nabla n_i &= n\nabla x_i + x_i \nabla n, \\
&= n\nabla x_i + x_i \left(\frac{\partial n}{\partial T}\right)_{p,V} \nabla T, \\
&= n\nabla x_i + x_i \frac{pV}{R}\left(-\frac{\left(\frac{\partial Z}{\partial T}\right)_{p,\mathbf{x}} T + Z}{(ZT)^2}\right)\nabla T.
\end{aligned} \tag{A.5}$$

which for the ideal gas state simplifies to

$$\nabla n_i^{ig} = n\nabla x_i^{ig} - x_i \frac{p^{ig}V}{RT^2}\nabla T \tag{A.6}$$

where $p^{ig} = \frac{nRT}{V}$ is the pressure in the ideal gas state, not to be confused with the reference pressure p_{ref}. Note that while $\nabla n^{ig} \neq \nabla n$, $\nabla n_i^{ig} \neq \nabla n_i$ and $\nabla x_i^{ig} \neq \nabla x_i$, the total mole fractions and mole numbers are obviously the same in the ideal gas state as in the real state. That is $n_i^{ig} = n_i$, $n^{ig} = n$ and $x_i^{ig} = x_i$. Inserting these relations into equation (A.1) and using the relation $\nabla \ln \varphi = \frac{\nabla \varphi}{\varphi}$ yields

$$\begin{aligned}
\nabla \ln\left(\frac{n_i^{ig}}{n_i}\right) &= \frac{\nabla n_i^{ig}}{n_i^{ig}} - \frac{\nabla n_i}{n_i} \\
&= \frac{1}{n_i}\left[n\nabla x_i^{ig} - x_i\frac{p^{ig}V}{RT^2}\nabla T - \left(n\nabla x_i - x_i\frac{pV}{R}\left(-\frac{\left(\frac{\partial Z}{\partial T}\right)_{p,\mathbf{x}} T + Z}{(ZT)^2}\right)\nabla T\right)\right] \\
&= \frac{1}{x_i}\left(\nabla x_i^{ig} - \nabla x_i\right) - \frac{1}{x_i T}\left(1 - \frac{\left(\frac{\partial Z}{\partial T}\right)_{p,\mathbf{x}} T + Z}{Z}\right)\nabla T \\
&= \frac{1}{x_i}\left(\nabla x_i^{ig} - \nabla x_i\right) - \frac{1}{x_i T}\left(\frac{\partial Z}{\partial T}\right)_{p,\mathbf{x}} \frac{T}{Z}\nabla T \\
\frac{1}{\nabla T}\nabla \ln\left(\frac{n_i^{ig}}{n_i}\right) &= (1-x_i)\left(S_{T,i} - S_{T,i}^{ig}\right) - \frac{1}{x_i}\left(\frac{\partial \ln(Z)}{\partial T}\right)_{p,\mathbf{x}}
\end{aligned} \tag{A.7}$$

Dividing Equation (A.2) by ∇T and inserting Equations (A.3), (A.4) and (A.7) results in a set of equations

that can be solved numerically for the Soret coefficients

$$\begin{aligned}
\frac{1}{v_i}\Bigg(\left(\frac{\partial \ln \phi_i}{\partial T}\right)_{p,\mathbf{x}} + \left(\frac{\partial \ln(Z)}{\partial T}\right)_{p,\mathbf{x}} - \sum_j \left[\left(\frac{\partial \ln \phi_i}{\partial x_j}\right)_{T,p,x_{k\neq j}} + \left(\frac{\partial \ln(Z)}{\partial x_j}\right)_{T,p,x_{k\neq j}}\right] x_j(1-x_j)S_{T,j}\Bigg) \\
- \frac{1-x_i}{v_i}\left(S_{T,i} - S_{T,i}^{ig}\right) + \frac{1}{v_i x_i Z}\left(\frac{\partial Z}{\partial T}\right)_{p,\mathbf{x}} \\
= \frac{1}{v_N}\Bigg(\left(\frac{\partial \ln \phi_N}{\partial T}\right)_{p,\mathbf{x}} + \left(\frac{\partial \ln(Z)}{\partial T}\right)_{p,\mathbf{x}} - \sum_j \left[\left(\frac{\partial \ln \phi_N}{\partial x_j}\right)_{T,p,x_{k\neq j}} + \left(\frac{\partial \ln(Z)}{\partial x_j}\right)_{T,p,x_{k\neq j}}\right] x_j(1-x_j)S_{T,j}\Bigg) \\
- \frac{1-x_N}{v_N}\left(S_{T,N} - S_{T,N}^{ig}\right) + \frac{1}{v_N x_N Z}\left(\frac{\partial Z}{\partial T}\right)_{p,\mathbf{x}}
\end{aligned} \tag{A.8}$$

which may be reordered to give

$$\begin{aligned}
\frac{1}{v_i}\left(\frac{\partial \ln \phi_i}{\partial T}\right)_{p,\mathbf{x}} - \frac{1}{v_N}\left(\frac{\partial \ln \phi_N}{\partial T}\right)_{p,\mathbf{x}} - \sum_j \left[\frac{1}{v_i}\left(\frac{\partial \ln \phi_i}{\partial x_j}\right)_{T,p,x_{k\neq j}} - \frac{1}{v_N}\left(\frac{\partial \ln \phi_N}{\partial x_j}\right)_{T,p,x_{k\neq j}}\right] x_j(1-x_j)S_{T,j} \\
- \frac{1-x_i}{v_i}\left(S_{T,i} - S_{T,i}^{ig}\right) + \frac{1-x_N}{v_N}\left(S_{T,N} - S_{T,N}^{ig}\right) \\
= \left(\frac{\partial \ln(Z)}{\partial T}\right)_{p,\mathbf{x}}\left(\frac{1}{v_N} + \frac{1}{v_N x_N} - \frac{1}{v_i x_i} - \frac{1}{v_i}\right)
\end{aligned} \tag{A.9}$$

It can immediately be seen that the this set of equations depends only on intensive properties of the system, and that it is independent of any standard state properties. It does however not immediately appear to be equivalent to Kempers' equation. It may be feasible to follow this approach using a hard-sphere reference state in place of the ideal gas reference state, which could be of importance as per the discussion in Section 6.

B Symbols and notation

Vectors are denoted with a boldface roman font as $\mathbf{a}$. Matrices with a boldface, underlined italic font as $\underline{\boldsymbol{A}}$. In the case where an italicised, sans serif font a occurs, and the vector $\mathbf{a}$ has been introduced, it is implied that $a = |\mathbf{a}|$.

Summations on the form $\sum_{i=a}^{b}$ are implied to include both the values a and b. Throughout the text it is implied that a symbol lacking a sub- or superscript refers to the total system. Such that $\varphi^j = \sum_i \varphi_i^j$, $\varphi_i = \sum_j \varphi_i^j$ and $\varphi = \sum_i \sum_j \varphi_i^j$ in the case where φ is an additive property. In other cases, the appropriate manner in which to combine the properties is explicitly given or assumed known. For example, for a two bulb system such as the one in Section 2.1, where x_1^α and x_1^β are the mole fractions of species 1 in bulb α and β, x_1 indicates the total mole fraction of species 1 while x^α indicates the mole fraction of species found in α, $x^\alpha = \frac{\sum_i n_i^\alpha}{\sum_j \sum_i n_i^j} = \frac{n^\alpha}{n}$.

A number of the symbols used in the description of kinetic gas theory are confined to Section 2.3. These are summarised in Table B.3. In the case of conflicting definitions between Tables B.1 and B.2 and Table B.3, the latter has precedence in Section 2.3, while the two former have precedence in the rest of the text. Specifically, b refers to an arbitrary molar property of a system, except in Section 2.3 where it refers to the impact parameter.

Table B.1: Symbols in the text. For symbols specific to Section 2.3 see Table B.3.

Symbol	Description	Unit
A	Helmholtz energy	J
α_T	Thermal diffusion factor	–
B	Extensive property	**
b	Partial molar property	**
$\mathrm{Co}(\cdot)$	Cofactor	–
D	Diffusion coefficient	$\mathrm{m^2\,s^{-1}}$
D_T	Thermal diffusion coefficient	$\mathrm{m^2\,s^{-1}}$
Δ_{ij}	Generalised diffusion coefficient	$\mathrm{s\,m^{-2}}$
Δ	(No subscript) Finite difference operator	–
δ_{ij}	Kronecker delta	–
$\underline{\underline{\mathbf{\Delta}}}$	Generalised diffusion matrix	$\mathrm{s\,m^{-2}}$
$\underline{\underline{\mathbf{\Delta}}}'$	"Padded" generalised diffusion matrix, see Eq. (3.35)	$\mathrm{s\,m^{-2}}$
$\det(\cdot)$	Determinant	–
ε	Mie-potential well depth	J
ϵ_N^r	Relative numerical error estimate.	–
η	Packing fraction	–
H	Enthalpy	J
h	Partial molar enthalpy	$\mathrm{J\,mol^{-1}}$
$\mathbf{J}$	Flux	*
k_B	Boltzmann constant	$\mathrm{J\,K^{-1}}$
k_T	Thermal diffusion ratio	–
κ	Condition number	–
L	Phenomenological coefficient	**
m	Molar mass or particle mass[1]	kg/molorkg
μ	Chemical potential	$\mathrm{J\,mol^{-1}}$
N	Number of components or order of approximation.	–
N_A	Avogadros number	$\mathrm{mol^{-1}}$
n	Mole number	mol
$\mathbf{n}$	Vector of all mole numbers	mol
$\hat{\mathbf{n}}$	Unit normal vector	–
p	Pressure	Pa
φ	Arbitrary variable	–
R	Gas constant	$\mathrm{J\,mol^{-1}\,K^{-1}}$
ρ	Molar density or particle density[1]	$\mathrm{mol\,m^{-3}}$ or $\mathrm{m^{-3}}$
ρ_m	Mass density	$\mathrm{kg\,m^{-3}}$
S	Entropy	$\mathrm{J\,K^{-1}}$
S_T	Soret coefficient	$\mathrm{K^{-1}}$
σ^{HS}	Hard sphere diameter	m
σ	Mie-potential root	m
T	Temperature	K

* Units depend on sub- and/or superscripts.

** Various units.

[1] Kinetic gas theory uses quantities per particle, otherwise the molar quantity is used.

Table B.2: Symbols in the text. For symbols specific to Section 2.3 see Table B.3.

Symbol	Description	Unit
$\mathbf{u}$	Particle velocity	$\mathrm{m\,s^{-1}}$
$\bar{\mathbf{u}}_i$	Average particle velocity of species i	$\mathrm{m\,s^{-1}}$
$\mathbf{u}^B$	Bulk velocity in the B FoR	$\mathrm{m\,s^{-1}}$
υ	Atomic diffusion volume	$\mathrm{m^3\,mol^{-1}}$
V	Volume	$\mathrm{m^3}$
v	Partial molar volume	$\mathrm{m^3\,mol^{-1}}$
x	Mole fraction	–
$\mathbf{x}$	Vector of all mole fractions	–
Z	Canonical partition function, or Compressibility factor	–
λ, γ, ν	Lagrange multipliers	–

Table B.3: Symbols specific to Section 2.3.

Symbol	Description	Unit
b	Impact parameter, see Fig. 2.2	m
$\mathscr{D}$	Concatenated differential operator	–
ϵ	Angular collision coordinate, see Fig. 2.2	–
f	Exact velocity distribution function (v.d.f.)	$\mathrm{s^3\,m^{-6}}$
$f^{(r)}$	r-th approximation term to the v.d.f.	$\mathrm{s^3\,m^{-6}}$
$\mathbf{g}$	Relative collision velocity	$\mathrm{m\,s^{-1}}$
I	Several specific integrals, see Eq. (2.45).	$*$
J	Several specific integrals, see Eq. (2.29)	$\mathrm{m^{-1}}$
m	Particle mass	kg
m_0	Sum of particle masses, $m_1 + m_2$	kg
M_i	m_i/m_0	–
N	Order of approximation	–
u	Particle speed	$\mathrm{m\,s^{-1}}$
$\mathbf{U}$	Peculiar velocity, $\mathbf{u} - \mathbf{u}^n$	$\mathrm{m\,s^{-1}}$
U	Peculiar speed, $\lvert\mathbf{U}\rvert$	$\mathrm{m\,s^{-1}}$
$\boldsymbol{\mathscr{U}}$	Dimensionless peculiar velocity, $\left(\frac{m_i}{2k_BT}\right)^{\frac{1}{2}} \mathbf{U}_i$	–
$\mathscr{U}$	Dimensionless peculiar speed, $\lvert\boldsymbol{\mathscr{U}}\rvert$	–
χ	Deflection angle, see Fig. 2.1	–

$*$ Depends only on integrand.

Table B.4: Sub- and superscripts in the text.

Subscript	Description	Superscript	Description
i, j, k, l	Species index	A	Basis for flux, determines unit
m	Molar quantity	B	Arbitrary frame of reference
r	Reduced quantity	ig	Ideal gas
c	Critical	HS	Hard sphere
α, β	Bulb index	$\circ$	Pure component
		ref	Reference state
		α, β	Bulb index
		$*$	Dimensionless quantity

Table B.5: Abbreviations in the text.

Abbreviation	Description
BH	Barker-Henderson
CS	Carnahan-Starling
EoS	Equation of State
FoR	Frame of Reference
HS	Hard sphere
LJ	Lennard-Jones
MD	Molecular dynamics
MET	Modified Enskog Theory
PVT	Pressure-Volume-Temperature
PC-SAFT	Perturbed chain SAFT
PR	Peng-Robinson
PT	Patel-Teja
RET	Revised Enskog Theory
SAFT	Statistical associating fluid theory
SET	Standard Enskog Theory
RAD	Relative absolute deviation
SRK	Soave-Redlich-Kwong
SW	Schmidt-Wensel
VdW	Van der Waals
VLE	Vapour-Liquid Equilibrium